이학박사 학위논문

백금 기반 촉매에 의한 메탄올의 전기화학적 산화 반응에 관한 연구

Pt-based Catalysts for Electrochemical Oxidation of Methanol

2017년 8월

서울대학교 대학원

화학부 전기화학전공

우 승 희

A Ph. D. Dissertation

Pt-based Catalysts for Electrochemical Oxidation of Methanol

By

Seunghee Woo

Supervisor: Professor Taek Dong Chung

Major: Electrochemistry

School of Chemistry

Graduate School of

Seoul National University

August 2017

ABSTRACT

This research mainly focuses on low temperature fuel cells. In detail, this research can be divided into following parts: i) Research on synthesis of low Pt loading catalyst, ii) Design of a new support material, iii) Development of one-step synthesis of Pt/graphene catalyst.

Part 1. Synthesis of Low Pt Loading Catalyst

Pt-based electrodes for proton exchange membrane fuel cells have been prepared by various methods such as polyol, impregnation, microemulsion. However, inactive catalyst sites are always present in the catalyst layer prepared by the conventional method. These inactive sites are not available for fuel cell reaction because the electrochemical reaction is limited only at the interface between the polymer electrolyte and the catalyst that is exposed to the reactant, known as the triple-phase reaction zone. In order to overcome this limitation, the electrodeposition method was applied on a surface of a substrate. Low loading Pt-Co cathode catalyst on a Nafion(Na^+)-bonded carbon layer was fabricated by using galvanostatic pulse technique to show the advantage of electrodeposition for high utilization of catalyst in proton exchange membrane fuel cell. The chemical composition of the electrodes could be controlled by varying the concentration of Co precursor. The Pt-Co catalysts evenly exist on the surface on the surface of

carbon electrode and its thickness was about 5.8 μm, which is four times thinner than conventional Pt/C. From XPS studies, Pt 4f spectrum of catalyst indicated the presence of oxidation states Pt^{2+} in addition to metallic Pt. The Pt-Co catalyst with a ratio of 3.2:1 was found to provide the highest single cell performance among the compositions studies. Therefore, the electrodeposition technique offers not only enhanced catalyst utilization but also simplification of preparation.

Keywords: Platium-cobalt cathode catalyst, Galvanostatic pulse electrodeposition, Cost-effective electrocatalyst

Part 2. A New Support Material

Carbon is an ideal material for supporting nano-sized metallic particles in a catalyst for low temperature polymer fuel cells. No materials other than carbon have the essential properties of electronic conductivity, corrosion resistance, surface properties, and low cost requied for the commercialization of fuel cells. However, carbon supports are relatively easy to be corroded under harsh fuel cell operation conditions, which would cause a rapid decay of electrochemical performance. To circumvent this shortcoming, the rational construction of carbon-based electrode materials with more advanced architectural design has been identified as the major solution. In this part, we designed a well-arranged structure of graphene-Vulcan carbon composite to prepare highly dispersed 40 wt.% PtRu electrocatalyst. Vulcan carbon was added as a nano spacer to enhance the utilization and electrochemical

activites of graphene-based materials. The results show that a PtRu catalyst loaded onto the graphene-Vulcan carbon (3:1 w/w) composite exhibits high electrocatalytic activity and high stability toward methanol electrochemical oxidation owing to the special structure of the graphene-Vulcan carbon composite. Also, we investigated the feasibility of a chemically activated graphene-supported electrocatalyst. The modified graphene sheets were synthesized by chemical activation using KOH. The chemically activation of graphene resulted in the creation of pores of various sized and increased the number of edge sites. The chemically activated graphene-supported PtRu catalyst shows a high electrocatalytic activity and stability toward methanol oxidation because of its three-dimensional and porous structure that facilitates the efficient access of reactants. These results indicate that a graphene-Vulcan carbon composite and chemically activated graphene can be used as a catalyst support in fuel cells.

Keywords: Graphene, Vulcan carbon, Nano spacer, Platinum, Ruthenium, Methnaol oxidation

Part 3. One-Step Synthesis of Pt/graphene Catalyst

Graphene-metal nanoparticle catalysts have typically been prepared by chemical or thermal reduction of mixture of GO (or graphene) and metallic precursors. These methods involve hazardous chemical, or high temperatures and complicated procedures. In this part, we demonstrate the one step co-electrodeposition synthesis

of the Pt/graphene catalyst using a galvanostatic pulse technique. Pt/graphene catalyst was uniformly deposited on a glassy carbon substrate, which facilitated the simultaneous electrochemical reduction of graphene oxide and formation of Pt nanoparticles. Compared to the commercial Pt/C catalyst, the electrochemically reduced Pt/graphene catalyst exhibited improved electrocatalytic activity for methanol oxidation due to the synergistic effects of an increase in the number of catalytic reaction sites and an enhancement of the charge transfer rate.

Keywords: Platinum, Graphene, Co-electrodeposition, Methanol oxidation

Student number: 2007-30082

TABLE OF CONTENTS

PART 2. DESIGN OF A NEW SUPPORT MATERIAL

GENERAL INTRODUCTION

1. Electrocatalysis of methanol oxidation

The electro-oxidation of small organic molecules on Pt electrocatalysts based electrodes has received more attention in the last decades due their application for electrochemical energy conversion in direct liquid feed fuel cells [1-3]. Among these molecules; methanol is used as liquid fuel for direct methanol fuel cells (DMFCs). Methanol is an attractive fuel for fuel cells due to its low price and easy handling, storage, and transport. DMFCs have an advantage over polymer electrolyte fuel cells utilizing hydrogen gas generated through a methanol reformer, because the system can be made much simpler. However, in order to accomplish the DMFC reaction, the methanol fuel should undergo the six-electron oxidation process on the electrode catalyst given follow

$$CH_3OH + H_2O \rightarrow CO_2 + 6H^+ + 6e^- \qquad E^o = 0.02\ V$$

It is at the anode surface where methanol is oxidized to CO_2, preferably at a 100 % yield, releasing six electron per methanol molecule to be harvested in the DMFC. Consequently, the oxidation kinetics is inherently slower. The slower kinetics are a result of intermediates formed during methanol oxidation [4]. Oxidation of the intermdiates to carbon dioxide requires the adsorption of an oxygen containing species (e.g., OH, H_2O). Methanol oxidation is a slow reaction that requires active multiple sites for the adsorption of methanol and the sites that can donate OH

species for desorption of the adsorbed methanol residues [5, 6]. The electro-oxidation of methanol has been studied on many electrode fabricated from unsupported metals and metal supported onto different supporting materials. Pt catalysts are still the most active catalysts materials for electro-oxidation of methanol [3, 7-11]. The electro-oxidation of methanol on Pt electrode surface is combined with several steps of dehydrogenation to form CO which is oxidized into CO_2 [12, 13]. **Figure 1** shows a proposed reaction network for methanol oxidation [14]. The mechanism for methanol oxidation has been debated significantly over the years, [15, 16] with research continuing to define the most significant pathways for different reaction conditions both experimentally [17, 18] and numerically [19]. There are multiple paths by which methanol oxidation can proceed. The selectivity of the reaction to formaldehyde, formic acid, and CO_2 depends on the reaction conditions, the catalyst used and the electrolyte. The selectivity of methanol oxidation over Pt to CO_2 is very high and formation of other byproducts will be neglected.

It should be noted in **Figure 1** that all reaction pathways to form CO_2 involve formation of adsorbed CHO or CO. It is believed that these species poison the catalyst surface and that their oxidation is the rate-limiting step for methanol oxidation. The mechanism shows that oxidation of the surface intermediates involves the addition of a hydroxyl group before the final oxidation to CO_2. The mechanism for the oxidation of CO is very important in the reaction mechanism for methanol oxidation and this step. This means that with a platinum catalyst electro-

adsorption of water is fairly slow and therefore addition of an OH^- group to the CO adsorbed on the reaction site must come from an attack of a liquid phase water molecule.

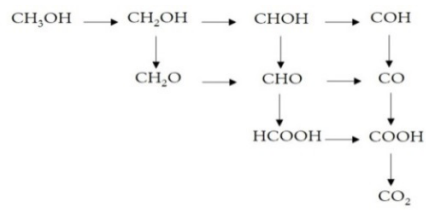

Figure 1. Reaction network for methanol oxidation.

The poisoning of the electrode surface (anode) by CO molecules formed during the methanol oxidation is one of the obstacles in the development of DMFCs for commercial applications. The modification of Pt catalysts with other metals or metal oxides which have higher tendency to form surface oxygenated species at lower potential is considered as one of the best ways to solve this problem [20, 21]. In order to improve the catalyst performance, many efforts have been done by many groups to synthesis new catalysts systems for methanol oxidation based on bimetallic catalysts such as PtRu [22-25], PtSn [26, 27], PtNi [28, 29], PtMo [30, 31], ternary alloy; PtRuNi [32-34], PtRuMo [33, 35, 36], and PtMOx (where M is, Ti, V, Mn, W) [37-40] which show higher catalytic activities than Pt alone have been investigated. Compared to pure Pt, the most active electrocatalysts known so far are alloys of Pt and Ru exhibiting lower overpotentials and extended life-time [41, 42]. The high catalytic activity of PtRu alloys for the electro-oxidation of methanol is described very well by the bifuctional action [41] of the alloy surface,

where the adsorption of methanol occurs on Pt ensembles and the further electro-oxidation of methanol dehydrogenation fragments is catalyzed by oxygen-like species adsorbed on adjacent Ru atoms.

The potential dependent discharge of water on Pt and Ru, respectively, to form oxygen-like surface species (symbolized by OH) will be approximated by the following two equations:

$$H_2O + Pt \rightarrow PtOH + H^+ + e^- \quad (1)$$

$$H_2O + Ru \rightarrow RuOH + H^+ + e^- \quad (2)$$

On the basis of cyclic voltammetry and ellipsometry, the adsorption of oxygen-like species in Pt (equation 1) will not occur to any appreciable extent below about 0.7 V, while it occurs on Ru at potentials as low as about 0.2 V (equation 2) [43]. Finally, given that the electrode potential is sufficiently positive to co-adsorb these oxygen-like species the electro-oxidation of the electrode poisoned by CO to CO_2 will be express as [44]

$$Pt + CH_3OH \rightarrow Pt\text{-}(CH_3OH)_{ads} \quad (3)$$

$$Pt\text{-}(CH_3OH)_{ads} \rightarrow Pt\text{-}(CH_3O)_{ads} + H^+ + e^- \quad (4a)$$

$$Pt\text{-}(CH_3O)_{ads} \rightarrow Pt\text{-}(CH_2O)_{ads} + H^+ + e^- \quad (4b)$$

$$Pt\text{-}(CH_2O)_{ads} \rightarrow Pt\text{-}(CHO)_{ads} + H^+ + e^- \quad (4c)$$

$$Pt\text{-}(CHO)_{ads} \rightarrow Pt\text{-}(CO)_{ads} + H^+ + e^- \quad (4d)$$

$$Ru + H_2O \rightarrow Ru\text{-}(H_2O)_{ads} \quad (5)$$

$$Ru\text{-}(H_2O)_{ads} \rightarrow Ru\text{-}(OH)_{ads} + H^+ + e^- \quad (6)$$

$$Pt\text{-}(CO)_{ads} + Ru\text{-}(OH)_{ads} \rightarrow Pt + Ru + CO_2 + H^+ + e^- \quad (7)$$

The rate determining step at 25°C is methanol adsorption/dehydrogenation (equation 3 or 4) [45, 46], while at elevated temperatures (*i.e.*, 60°C) the bimolecular surface reaction involving -OH_{ads} (equation 7) becomes rate limiting. The affinity of Ru for oxygen, as reflected in the Ru-O bond strength, will affect both the ability to oxidatively adsorb water [47] (equation 5 and 6) and the ease for Ru-O bonds to be broken in the formation of CO_2 (equation 7). The scheme of dehydrogenation on Pt surface is shown in **Figure 2**. The first step involves the adsorption of methanol from the bulk of the solution onto the electrode surface and its successive dehydrogenation to form linearly bonded CO.

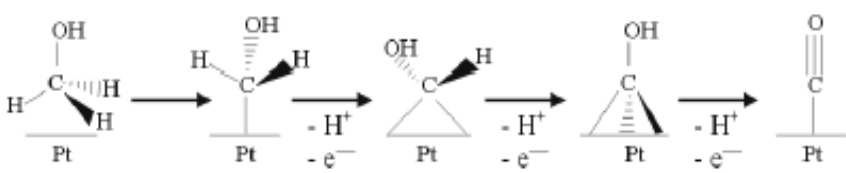

Figure 2. Scheme of methanol oxidation on Pt showing the consecutive stripping of hydrogen atoms.

Stripping voltammetry and potentiostatic stripping revealed that the adsorption of CO is equally facile on both Pt and Ru surface atoms and suggested that about 0.2 V negative shift of the onset of CO oxidation on the most active PtRu alloy electrode compared to pure Pt is related to the nucleation of oxygen-containing species on Ru atoms at low electrode potentials, thereby promoting the oxidation of CO to CO_2 [48].

2. Electrocatalyst

Electrochemical reactions for which no adsorbed intermediate exists are very rare and the electron transfer step or steps usually involve adsorbed species [49]. These kind of species that are necessary for a reaction to take place but do not seem to participate in the global equation, are called catalysts. Hydrogen oxidation reaction occurs easily on Pt. Since the metallic surface plays an active role in the formation of intermediates, the nature and particular state of the surface is crucial for the success of the reaction. The metallic surface is then an electrocatalyst, a catalyst for the electron transfer reaction. If the rate-determining step of the reaction involves adsorbed species, and this is probably the case, then the nature and structure of the metallic surface will determine the speed of the reaction (**Figure 3**).

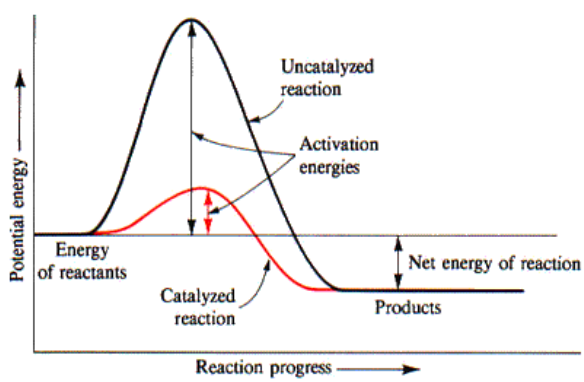

Figure 3. Traditional potential energy curve illustrating the lowering of the activation energy as the addition of a catalyst. The catalyzed activation energy is distinctively lower than that of an uncatalyzed reaction. As a result, the catalyzed reaction rate is increased; products are formed quicker and with greater yields over time [49].

The requirements of the catalyst for fuel cells are as follows: (**Figure 4, 5**)

1) High intrinsic activity for hydrogen/methanol oxidation reaction at the anode and for oxygen reduction reaction at the cathode.

2) Good durability to minimize the loss of electrocatalytic activity.

3) Good electrical conductivity to minimize resistive losses in the catalyst layer.

4) Thermal and acidic stability for maintaining the electrocatalytic activity.

Considering the requirements of suitable catalyst materials for the low temperature fuel cell, Pt and Pt-based catalysts are found to meet these requirements, in both activity and stability. Especially, Pt nanoparticles supported on carbon (Pt/C) have advantages such as larger relative surface area, higher efficiency, and good intrinsic activity.

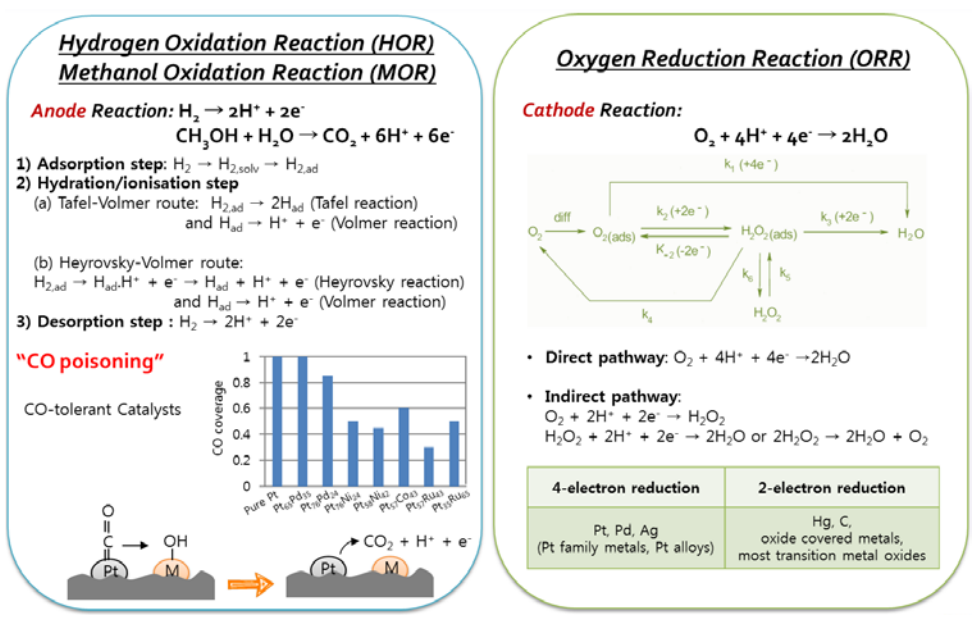

Figure 4. Anode and cathode reactions.

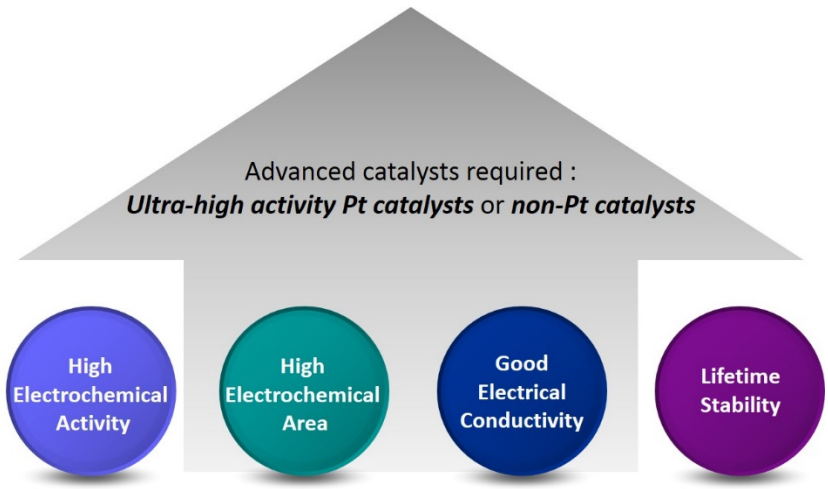

Figure 5. Essential criteria for electrocatalyst.

2. 1. Catalyst support

Many industrial catalyst consists of metals or metal compounds supported on an appropriate support, the basic role of which is to maintain the catalytically active phase in a highly dispersed state (**Figure 6**). Carbon materials have been used for a long time in heterogeneous catalysis, because they can act as direct catalyst or, more important, they can satisfy most of the desirable properties required for a suitable support [50]. The advantage of spreading the active phase on a support is to disperse it throughout the pore system, thus making it possible to obtain a large active surface per unit weight used. A supported catalyst facilitates the flow of gases through the reactor and the diffusion of reactants through the pores to the active phase. The performance and stability of fuel cells are known to strongly depend on the carbon support used as well as the catalytically active species [51].

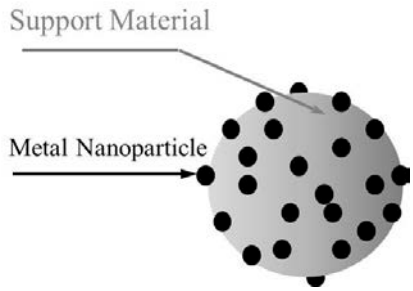

Figure 6. Carbon supported platinum catalyst.

The requirements of ideal support materials for Pt-based electrocatalysts should have the following characteristics: a high surface area for a high degree of dispersion of nanosized catalysts, a high electrical conductivity to facilitate electron transport during the redox reaction, a suitable pore structure and large pore volume to provide an open highway network around the active catalyst for a facile diffusion of fuels and products toward and away from the catalyst sites and low cost to make an inexpensive fuel cells. High surface area and a well-developed porosity are essential for achieving large metal dispersion, which usually results in a high catalytic activity.

2. 2. Triple phase boundary

The idea of the triple phase boundary is extensively employed in the fuel cell literature, especially with respect to solid oxide fuel cells and polymer electrolyte membrane fuel cells. The triple phase boundary concept holds that the hydrogen/methanol oxidation reaction and the oxygen reduction reaction can only

occur at confined spatial sites, called “triple phase boundaries” where ionomer, reactant, and electrically connected catalyst regions contact. A simplified schematic of the triple phase boundary is shown in **Figure 7**. The reaction kinetics often present a significant limitation to fuel cell performance. Therefore, understanding, characterizing, and optimizing the triple phase boundary content in fuel cells provides excellent opportunities for performance enhancement [52].

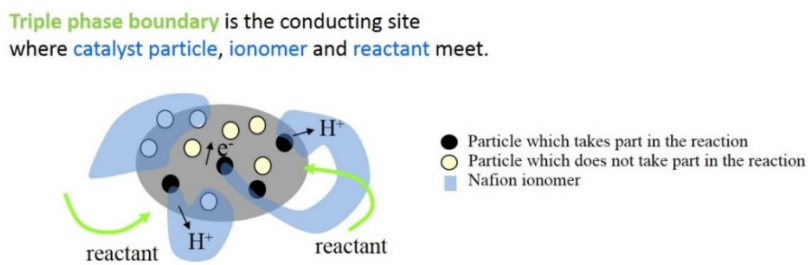

Figure 7. A simplified schematic diagram of the catalyst particle, ionomer and reactant.

3. Electrochemical characterization

3. 1. Cyclic voltammetry

Cyclic voltammetry (CV) technique is applied to a three electrode cell. Thus, the electrode potential is controlled by an applied driving potential difference E_d between the reference and working electrodes. The reference electrode connections must have a very high input impedance, so that the current flows only between the working and counter electrodes. The reference input of the potentiostat is

connected to the working electrode in the cell, and the potential of the working electrode is measured against the reference electrode. The potential scan is applied in one direction (positive or negative), starting at chosen values, and then the sweep rate is inverted at selected reversing points which are selected in such a way that one has oxygen evolution in the positive and hydrogen evolution in the negative part. In PtRu alloy working electrode, 800 mV *vs.* SHE (standard hydrogen electrode) is typically selected for the positive limit because Ru atoms are dissolved over the limit and 0 mV *vs.* SHE is selected for the negative limit because hydrogen evolution starts below the limit. CV at given electrodes without active species in the electrolyte such as sulfuric acid or perchloric acid results in current/potential relations that are very characteristic for the electrode material used. Primarily, there is a contribution due to the charging of the double layer. Due to a fast attainment of the equilibrium, the double layer capacity is not a function of scan rate, but it can depend on potential. A second contribution, and in general a much larger one, is given by charging a pseudo-capacitance of value, *e.g.*, capacity effects due to faradaic reactions like the formation and dissolution of hydride and oxide layers on the surface. This capacity does not also depend on the scan rate.

The voltammogram presented in **Figure 8** was taken using a polycrystalline Pt electrode in 1 M KOH [53]. In this voltammogram, the potential is referred to a reversible hydrogen electrode (RHE) in the same solution. Following the current starting at + 450 mV, we observe that between this potential and 550 mV the only current that flows is tat required to charge the electrolytic double layer. Above 550

mV, oxygen chemisorption start with

$$Pt + OH^- \rightarrow Pt\text{-}OH + e^-$$

and above ca. 800 mV

$$Pt\text{-}OH + OH^- \rightarrow Pt\text{-}O + H_2O + e^-$$

Above ca. 1600 mV oxygen evolution begins, and in addition, a phase oxide may form on the Pt surface (with a thickness larger than a monolayer). At lower potentials oxide may also be formed, if a constant potential is applied. After the reversion of potential, oxygen molecules near the surface are reduced together with the chemisorbed oxide layer. At lower potentials there is a small "double layer" region followed by the underpotential deposition of H-atoms

$$Pt + H_2O + e^- \rightarrow Pt\text{-}H + OH^-$$

Finally, close to the thermodynamic H_2/OH^- potential, a strong evolution of hydrogen starts. After scan reversion, H_2 molecules near the electrode and the layer of adsorbed hydrogen are oxidized again.

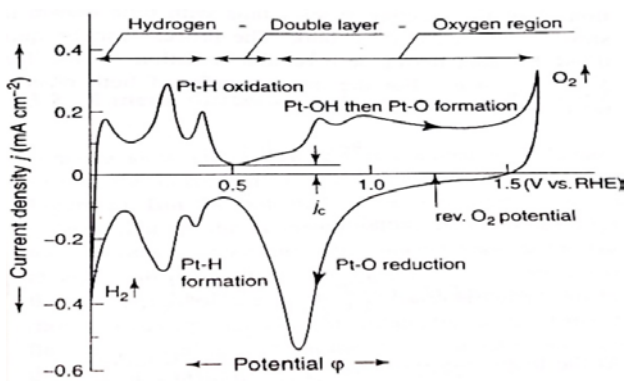

Figure 8. Cyclic voltammogram of polycrystalline platinum in 1 M KOH, 20°C, nitrogen purged, sweep rate = 100 mV s^{-1} [53].

Electrochemical active surface area (ECA) of electrodes is measured by CV either using the area under the hydrogen adsorption/desorption peaks or CO adsorption/stripping peaks. To determine the ECA, CV is carried out on the electrode of interest over a range between 0 and 1600 mV. The specific charge transfer due to hydrogen adsorption and desorption can be obtained from

$$Q_H = \frac{1}{2}(Q_T - Q_{DL}),$$

where Q_T is the total specific charge transfer in the hydrogen adsorption/desorption potential region and Q_{DL} is the specific capacitive charge in the double layers of both Pt and carbon support. Q_T can be obtained by integration of the CV curves in the relevant potential region [54]:

$$Q_T = \frac{1}{v}\int_{0.05}^{0.4}(I_d - I_a)dE\,,$$

where v is the scan rate, I_d and I_a are the specific current of desorption and adsorption, respectively, and E is the potential. Q_{DL} can be similarly obtained by integrating the double layer charging region. Assuming the charge per real cm^2 of Pt with monolayer adsorption of hydrogen [55] is Q_H°=210 μC cm^{-2}, then the active specific areas can be obtained from

$$S_{ECA} = \frac{Q_H}{Q_H^o}$$

Although the above method is commonly used for Pt/C catalysts, it cannot be applied to PtRu/C catalysts because Ru absorbs hydrogen. Real surface area can be characterized by CO_{ad} stripping analysis. As for PtRu/C, the surface area can be estimated assuming a monolayer of linearly adsorbed CO and the coulombic charge

necessary for oxidation as 420 μC cm^{-2}, because the hydrogen adsorption/desorption peak of the PtRu/C is not well defined comparing to that of the Pt/C.

3. 2. Single cell test

The MEA (membrane electrode assembly) of a low temperature fuel cell usually consists of five layers which include gas and liquid diffusion layers, and electrocatalyst layers with a polymeric proton conducting acidic membrane in between. The proton conducting membrane acts as an electronic insulator between the electrodes, but allows protons to migrate efficiently from the anode to the cathode. The membrane also functions as a physical barrier to prevent mixing of the reactants. In addition, a soluble form of the membrane material is used to impregnate the electrocatalyst layers to extend the membrane interface. This provides a proton conducting pathway. The overall schematic diagram of a low temperature is shown in **Figure 9**. The cell consists of two electrodes which are separated by the electrolyte and which are connected in an external circuit. The electrodes are exposed to gas or liquid flows to supply the electrodes with fuel or oxidant. The electrodes have to be gas or liquid permeable and therefore possess a porous structure. The structure and content of the gas diffusion electrodes is quite complex and requires considerable optimization for the practical application. Electrons flow in the external circuit during these reactions.

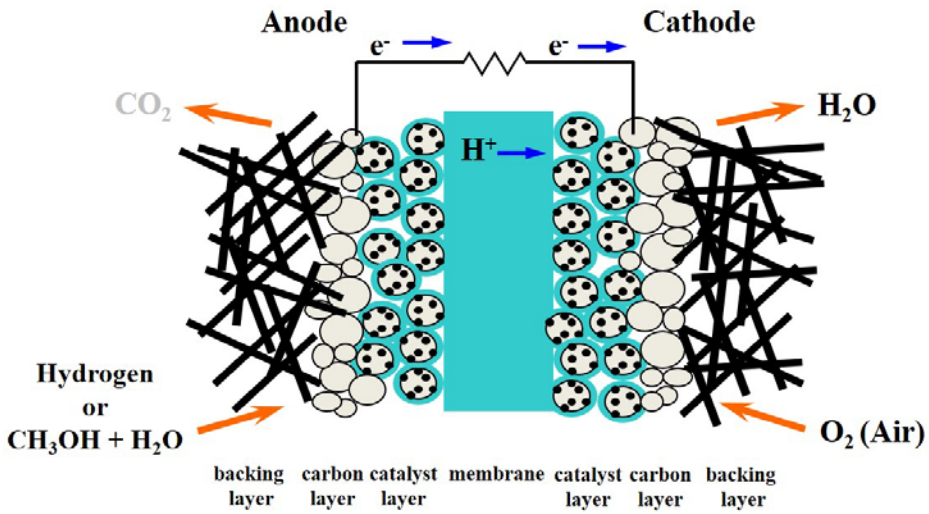

Figure 9. Schematic diagram of a low temperature fuel cell.

The factors which limit a low temperature fuel cell efficiency is show in **Figure 10**. Several sources contribute to irreversible losses in a practical fuel cell. The losses, which are often called polarization, overpotential or overvoltage (η), originate primarily from three sources: (i) activation polarization (η_{act}), (ii) ohmic polarization (η_{ohm}), and (iii) concentration polarization (η_{conc}). These losses result in a cell voltage (V) for a fuel cell that is less than its ideal potential, E (V=E-losses). The activation polarization loss is dominant at low current density. At this point, electronic barriers have to be overcome prior to current and ion flow. Activation losses show some increase as current increases. Ohmic polarization (loss) varies directly with current, increasing over the whole range of current because cell resistance remains essentially constant. Mass transport losses occur over the entire range of current density, but these losses become prevalent at high limiting currents

where it becomes difficult to provide enough reactants flow to the cell reaction sites. The improvement of cell performance is approached by modifications to fuel cell design (improvement in electrode structures, better electrocatalysts, more conductive electrolyte and, thinner cell components, etc.). In this study, the improvement in better electrocatalysts is focused to.

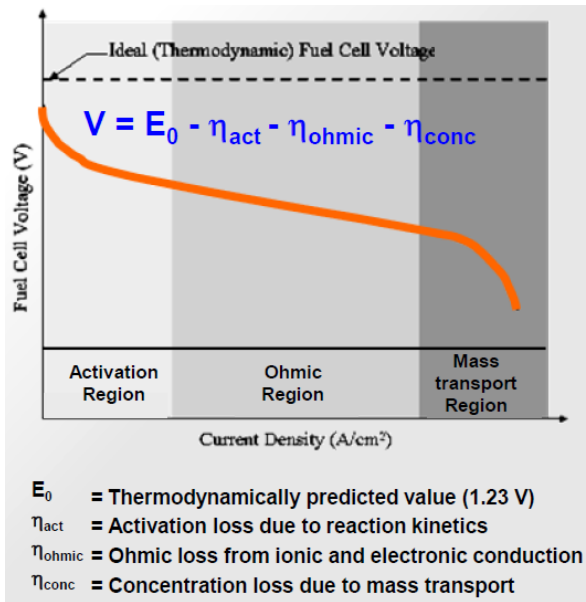

Figure 10. Ideal and actual fuel cell voltage/current characteristic.

4. REFERENCES

[1] E.L. Gyenge, *Chapter 4: Electrocatalytic oxidation of methanol, ethanol and formic acid', in PEM Fuel Cell Electrocatalysts and Catalyst Layers,* editor; Jiujun Zhang, Springer, New York, p. 165-270 (2008).

[2] A.O. Neto, R.W.R. Verjulio-Silva, M. Linardi, E.V. Spinacé, *Int. J. Electrochem. Sci*., 4 (2009) 954.

[3] A.B. Kashyout, A.A.A. Nasr, M.S. Mohy Eldin, *Alexandria Engineering Journal*, 48 (2009) 491.

[4] M. Leger, C. Lamy, B. Bunsenges, *J. Phys Chem.*, 94 (1990) 1021.

[5] V.S. Bagotzsky, B. Yu. Vassiliev, O.A. Khazova, *J. Electroanal. Chem.,* 81 (1997) 229.

[6] G.T. Burstein, C.J. Barnett, A.R. Kucernak, K.R. Williams; *Catal. Today*, 38 (1997) 425.

[7] T. Iwasita, *Electrochim. Acta*, 47 (2002) 3663.

[8] M. Brandalise, M.M. Tusi, R.M. Piasentin, M. Linardi, E.V. Spinacé, A.O. Neto, *Int. J. Electrochem. Sci*., 5 (2010) 39.

[9] H. Liu, C. Song, L. Zhang, J. Zhang, H. Wang, D.P. Wilkinson, *J. Power Sources*, 155 (2006) 95.

[10] W.M. Martínez, T.T. Thompson, M.A. Smit, *Int. J. Electrochem. Sci.*, 5 (2010) 931.

[11] A. Hamnett; *Catal. Today*, 38 (1997) 445.

[12] J.L. Go´mez de la Fuente, M.V. Martı´nez-Huerta, S. Rojas, P. Terreros, J.L.G. Fierro, M.A. Pena, *Catal. Today,* 116 (2006) 442.

[13] E.A. Bagotski, Y.B. Vassiliev, O.A. Khazova, *J. Electroanal. Chem.*, 81 (1977) 229.

[14] L. Carrette, K.A. Friedrich, U. Stimming, *ChemPhysChem,* 1 (2000) 162.

[15] R. Parsons, T. Vandemoot, *J. Electroanal. Chem.,* 257 (1988) 9.

[16] T. Iwasita, *Electrochim. Acta,* 47 (2002) 3663.

[17] E.A. Batista, G.R.P. Malpass, A.J. Motheo, T. Iwasita, *J. Electroanal. Chem.,* 571 (2004) 273.

[18] E.A. Batista, G.R.P. Malpass, A.J. Motheo, T. Iwasita, *Electrochem. Commun.,* 5 (2003) 843.

[19] S. Desai, M. Neurock, *Electrochim. Acta,* 48 (2003) 3759.

[20] G. Stalnionis, L. Tamasauskaite-Tamasiunaite, V. Pautieniene, A. Sudavicius, Z. Jusys, *J. Solid State Electrochem.,* 8 (2004) 892.

[21] B. Gurau, R.Viswanathan, R.Liu, T.J. Lafrenz, K.L. Ley, E.S. Smotkin, E.Reddington, A.Sapienza, B.C. Chan, T.E. Mallouk, S. Sarangapani, *J. Phys. Chem. B,* 102 (1998) 9997.

[22] Z. Liu, J.Y. Lee, W. Chen, M. Han, L.M. Gan, *Langmuir,* 20 (2004**)** 181.

[23] T. Maiyalagan *Int. J. Hyd. Energy.,* 34 (2009) 2874.

[24] T. Maiyalagan, *J. Solid State Electrochem.,* 13 (2009) 1561.

[25] S. Jingyu, H. Tianshu, C. Yanxia, Z. Xiaogang, *Int. J. Electrochem. Sci.,* 2

(2007) 64.

[26] A.O. Neto, R.R. Dias, M.M. Tusi, M. Linardi, E.V. Spinacé, *J. Power Sources*, 166 (2007) 87.

[27] H.B. Hassan, *J. Fuel Chem. Tech.*, 37 (2009) 346.

[28] T.C. Deivaraj, W. Chen, J.Y. Lee**.** *J. Mater. Chem.*, 13 (2003) 2555.

[29] Z.C. Wang, Z.M. Ma, H.L. Li, *Appl. Surf. Sci.*, 254 (2008) 6521.

[30] S.A. Lee, K.W. Park, J.H. Choi, B.K. Kwon, Y.E. Sung, *J. Electrochem. Soc.*, 149 (2002) A1299.

[31] T.Y. Morante-Catacora, Y. Ishikawa,C. R. Cabrera, *J. Electroanal. Chem.*, 621 (2008) 103.

[32] M.V. Martínez-Huerta, S. Rojas, J.L. Gómez de la Fuente, P. Terreros, M.A. Peña, J.L.G. Fierro *Appl. Catal. B: Environ*., 69 (2006) 75.

[33] S. Pasupathi, V. Tricoli, *J. Solid Sate Electrochem.*, 12 (2007)1093.

[34] T. Huang, J. Liu, R. Li, W. Cai, A. Yu, *Electrochem. Commun.*, 11 (2009) 643.

[35] A. Oliveira Neto, E.G. Franco, E. Aricó, M. Linardi, *Portug. Electrochim. Acta*, (2004) 93.

[36] Z. B.Wang1, P.J. Zuo, G.P. Yin, *Fuel Cells*, 9 (2009) 106.

[37] T. Maiyalagan, B. Viswanathan, U.V. Varadaraju, *J. Nanosci. Nanotechnol.* 6 (2006) 2067.

[38] T. Maiyalagan, B. Viswanathan *J. Power Sources*, 175 (2008) 789.

[39] T. Maiyalagan, F.N. Khan, *Catal. Commun.* 10, (2009) 433.

[40] C. Zhou, H. Wang, F. Peng, J. Liang, H. Yu, J. Yang, *Langmuir*, 25 (2009) 7711.

[41] O. Nishikawa, K. Doyama, K. Miyatake, H. Uchida, M. Watanabe, *Electrochim. Acta*, 50 (2005) 2719.

[42] J.B. Goodenough, A. Hamnett, B.J. Kennedy, R. Manoharan, S.A. Weeks, *J. Electroanal. Chem.*, 240 (1988) 133.

[43] E. Ticanelli, J.G. Beery, M.T. Paffett, S. Gottesfeld, *J. Electroanal. Chem.*, 258 (1989) 61.

[44] T. Frelink, W. Visscher, J.A.R. van Veen, *Surf. Sci.*, 335 (1995) 353.

[45] J. Sobkowski, K. Franaszczuk, A. Piasecki, *J. Electroanal. Chem.*, 196 (1985) 145.

[46] N.I. Il'chenko, G.I. Golodets, *J. Catal.*, 39 (1975) 73.

[47] J.O.m. Bockris, H. Wroblowa, *J. Electroanal. Chem.*, 7 (1964) 428.

[48] H.A. Gasteiger, J.E. Panels, S.G. Yan, *J. Power Sources*, 127 (2004) 162.

[49] W. Vielstich, A. Lamm, H.A. Gasteiger, *Handbook of fuel cells-fundamentals technology and applications*, John Wiley & Sons, (2003).

[50] L.R. Radovic, F. Rodriguez-Reinoso, *Chemistry and physics of carbon*, P.A. Thrower. Marcel Dekker, New York, (1997).

[51] P.J. Britto, K.S.V. Santhanam, A. Rubio, J.A.A. Alonso, P.M. Ajayan, *Adv. Mater.*, 11 (1999) 154.

[52] R. O'Hayre, D.M. Barnett, F.B. Prinz, *J. Electrochem. Soc.*, 152 (2005) A439.

[53] C.H. Hamann, A. Hamnett, W. Vielstich, *Electrochemistry*, Wiley-VCH,

Weinheim (1998).

[54] F.C. Nart, W. Vielstich, *in Handbook of Fuel Cells*, Wiley, New York, 2003.

[55] M. Freemantle, *Chem. Eng. News*, 74 (1996) 62.

PART 1

SYNTHESIS OF LOW Pt LOADING CATALYST BY PULSED GALVANOSTATIC ELECTRODEPOSITION

1. INTRODUCTION

Highly dispersed Pt on carbon black has been widely employed in polymer electrolyte membrane fuel cell (PEMFC). For commercial application, it is necessary to develop inexpensive catalysts that exhibit higher performance and stability than Pt/C catalysts. Low Pt loading and improved mass activity are required since Pt, which is used as the catalyst, is rare and expensive. For these reasons, many studies have been directed towards the development of electrodes with high performance with low Pt loadings [1-4]. Anode and cathode electrodes for PEMFC have been prepared by various methods such as the impregnation [14], polyol [15], microemulsion [16] and electrodeposition methods [17-21]. Catalyst powders synthesized by means of the impregnation, polyol, and microemulsion methods were well mixed with an ionic binder and then apply the paste on a porous support by a decal or a blade or a spray method. After this procedure, the membrane electrode assembly (MEA) was generally fabricated by using the prepared electrode and a Nafion membrane. Inactive catalyst sites are always present in the catalyst layer prepared by the conventional method (**Figure 1**). This method does produce a large number of inactive catalyst sites. These inactive sites are not available for fuel cell reaction because the electrochemical reaction is limited only at the interface between the polymer electrolyte and the catalyst that is exposed to the reactant, known as the triple-phase reaction zone [22]. Also, an ionic binder is added to the electrode in order to extend the triple-phase boundaries. As a

result, it increases the production cost of the electrode.

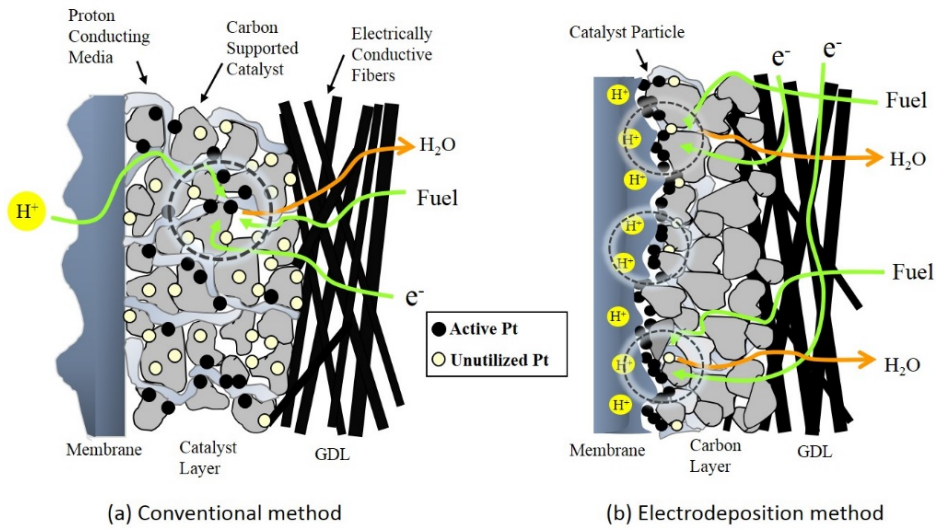

Figure 1. Structure of electrode prepared by (a) conventional method and (b) electrodeposition method and transport of fuel, protons, and electrons.

In order to overcome this limitation, the electrodeposition method was applied on a surface of a substrate. Therefore, it offers not only enhanced catalyst utilization but also simplification of preparation. Taylor et al. [23] developed an electrochemical catalyzation technique to improve the utilization of Pt catalyst. Antoine and Durand [24] impregnated carbon with H_2PtCl_4 and applied an electrochemical pulsed current to deposit Pt on the Nafion active layer. This process guarantees a smaller active layer thickness and high Pt mass fraction up to 40 wt.%. Kim et al. [20] used a pulse electrodeposition technique to prepare MEA. In this technique, Pt was deposited on the surface of the carbon electrode, followed by heat treatment and Nafion impregnation. In this case, the impregnated polymer electrolyte covered the

Pt particles, and thus, some Pt particles were not exposed to the reactant. In addition, some Pt particles were not always in good contact with the electrolyte phase because Nafion could not penetrate into the catalyst layer easily. In terms of the triple-phase boundary reaction zone, these electrodes may face problems of poor electrolyte contact or poor reactant diffusion. In order to overcome these problems, the electrodeposition technique was applied on a Nafion-bonded uncatalyzed carbon electrode. Thus use of Nafion as a proton conducting binder in the catalyst layer has been demonstrated to increase the Pt utilization significantly. In first-grneration PEMFCs, catalyst layers containing PTFE (polytetrafluoroethylene)-bonded Pt catalysts with a high loading of 4 mg_{pt} cm^{-2} were used as the PEMFC electrodes [25]. Srinivasan et al. reported high performance electrodes with a low catalyst loading of 0.35 mg_{pt} cm^{-2} [26, 27]. This achievement was made possible mainly by using Nafion instead of PTFE as the catalyst binder. For using a Nafion-bonded carbon electrode, it is necessary to modify the heat treatment process because Nafion is thermally unstable above 150 ^{o}C [28]. Another approach for the heat treatment is improving the mechanical properties of Nafion ionomer. It is reported that if the protons in Nafion ionomer are exchanged by other cations, the thermal stability of Nafion ionomer is improved [29, 30-33]. The molecular structure of Nafion (**Figure 2**) consists of a poly (tetrafluoroethylene) (PTFE) backbone with perfluorinated pendant chanins terminated by sulfonate groups in the acid form. Mauritz and Moore performed DMA (dynamic mechanical analysis) studies of various Nafion membranes

including the acid form and other cationic forms [28]. After the conversion of Nafion to the sodium sulfonated form (Nafion-Na^+), the ionomer exhibited a significant shift in the α relaxation to temperature near 250 ^oC. Due to this thermal stability, the Nafion (Na^+)-bonded electrodes are possible to treat to 250 ^oC.

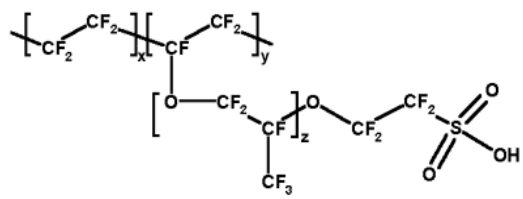

Figure 2. Chemical structure of Nafion (sulfonic acid form).

In general, electrodeposition can be carried out by using either a potentiostatic or a galvanostatic technique, which involves direct and pulse techniques. Electrodeposition via the galvanostatic pulse technique is considered convenient to improve the current distribution. Therefore, it is easy to control the particle size and composition of the alloy simply by varying experimental parameters such as on/off time and peak current density [34, 35]. Electrode fabrication by electrodeposition results in the increase of catalyst utilization and low cost requirement. An advantage point of electrodeposition is also the simplification of electrode preparation reducing the catalyst synthesis step. Therefore, electrode fabrication using the electrodeposition method can increase the efficiency of PEMFC [36].

In this part, we study on the electrode preparation method for low Pt-Co loading on Nafion (Na^+)-bonded carbon electrodes using a current pulsed electrodeposition

technique and the optimal ratio of Pt-Co cathode catalyst. The main feature of this method is the location of the Pt-Co deposition that is limited only to the triple-phase boundary reaction zone areas and thereby we can get improved performance with low Pt-Co loading.

2. LITERATURE SURVAY

2. 1. Electrodeposition process

In an electrodeposition process, metal ions are transferred from the solution to the cathode and adsorbed at the electrode surface and adatoms are formed by the change transfer reaction. An adatom deposited on the surface of a perfect crystal stays on the surface as an adion only temporarily because of its low binding energy to the crystal. And formation of clusters occurs to increase is stability and finally incorporated into the crystal lattice [37]. At this time, two competing steps occur at the surface of electrode. One is the growth of crystals and another is the creating nucleation. These two steps can be influenced by the surface diffusion rate of adatom and the rate of charge transfer reaction.

When the charge transfer step in an electrodeposition reaction is fast, the rate of growth of nuclei (crystallites) is determined by the lattice incorporation step of diffusion of electrodeposition ions into the nucleus (diffusion in the solution). In the initial stages of growth of the nuclei it can be assumed that nuclei grow

independency of each other. In this case the rate of growth of a single 3D hemispherical nucleus is given by

$$\nu = \left(\frac{nFk^3 2\pi M^2}{\rho^2}\right)t^2 \quad \cdots\cdots\cdots\cdots \quad \text{(i)}$$

Where k is the rate constant of 3D nucleus growth (mol cm^{-2} s^{-1}), M is molecular weight, and ρ is the density of deposit (mass/volume) [37].

However, in order to obtain uniform and small sized catalyst particles, formation of nuclei is preferred growth of existing crystal. The rate of nuclei formation, ν, is given by:

$$\nu = k_1 \exp(-k_2/h^2) \quad \cdots\cdots\cdots\cdots \quad \text{(ii)}$$

where k_1 and k_2 are constants and h is the overpotential [34]. Therefore, the rate of nuclei formation depends on the overpotential that is given by the Tafel expression,

$$h = a + b \log i \quad \cdots\cdots\cdots\cdots \quad \text{(iii)}$$

where a and b are constants, and i is the current density. From the above equations, it can be indicated that as the applied current density increases.

Pulsed electrodeposition can raise the limiting current density, because the metal ion can be supplied from the bulk solution during the off time of the pulse. Consequently, this effect of off time bring out increase of nucleation rate based on equation [34, 38, 39] but the galvanostatic direct technique has only one variable such as current density. As current density for deposition increases, the metal ions near cathode are quickly exhausted and these concentrations become zero. Finally, the galvanostatic direct technique has lower limit current density and overpotential

for nucleation compared to the galvanostatic pulse technique [34].

In general, electrodeposition can be largely divided into galvanostatic [40, 41] and potentiostatic method (**Table 1**). The galvanostatic method is more convenient to high geometric surface area electrodes because of two-electrode system and arbitrary waveform generator [42]. The galvanostatic method with two-electrode system assorts direct and pulse technique. Especially, the galvanostatic pulse technique show many advantages. For example, improvement of the current distribution and possibility of adjustment for the particle size of catalyst and composition of alloy by varying independent parameters, such as on-time (t_{on}), off-time (t_{off}) and peak current (i_p) density as shown in **Figure 5**. The duty cycles that is related to on-time and off-time is defined as follows.

$$\text{Duty cycle (\%)} = \frac{t_{on}}{t_{on}+t_{off}} \times 100 \quad \cdots\cdots\cdots\cdots\cdots\cdots\cdots\cdots\cdots\cdots\cdots\cdots\cdots\cdots \quad \text{(iv)}$$

During on time, growth of existing crystal and formation of nuclei occur at the surface of electrode as shown in **Figure 6**.

Table 1. Galvanostatic technique and potentiostatic technique.

Galvanostatic Technique		Potentiostatic Technique	
Two-electrode system		Three-electrode system	
Direct current	Pulse current	Constant potential	Pulse potential
Only one variable (current density: j)	Three independent variables (t_{on}, t_{off}, i_p)	Increase diffusion layer thickness	-Renewal of diffusion layer - Short deposition time

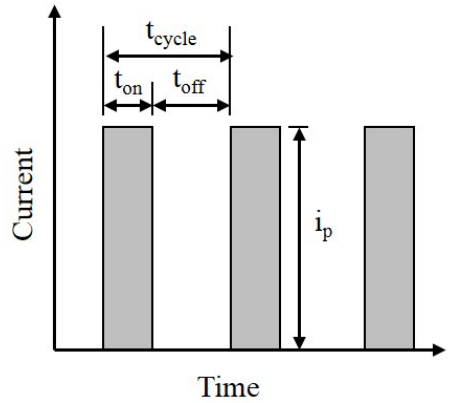

Figure 5. General concept of galvanostatic pulsed electrodeposition.

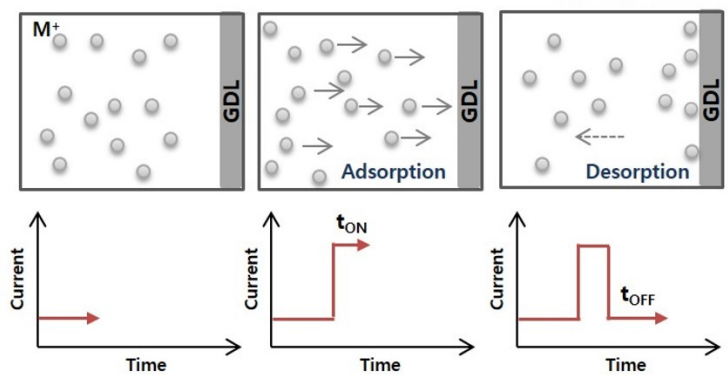

Time interval	Conditions	Phenomena
t_{on} (On-time)	- Double layer charging - Overpotential - Concentration profile near electrode - Adsorption (ion)	- Nucleation rate - Growth mechanism - Electrode reaction - Co-deposition (alloy) - Additive reaction
t_{off} (Off-time)	- Double layer discharging - Potential relaxation - Concentration profile relaxation - Desorption	- Surface diffusion - Corrosion, displacement reactions

Figure 6. Effect of duty cycle in galvanostatic pulsed electrodeposition.

(1) Effect of Peak Current Density

A decrease in particle size by application of the current density has often been reported in the literature [35]. There are several ways of examining the effect of pulsed current density on the particle size. One of the ways is an increase in pulsed current density at constant pulse charge and at constant average current density. This method has the advantage that ambiguity in interpretation of the results due to the influence of the off-time can be avoided. Increased pulsed current density amplitude leads to increased adatom concentrations, corresponding to equation (iii) to higher overpotentials and therefore, according to equation (ii), to higher nucleation rates.

(2) Effect of Duty Cycle

The duty cycle can be changed by increasing the off-time when the peak current density, on-time and total charge density are fixed. Duration of the off-time plays an important role in the deposition since the recovery of concentration of the electroactive species on the surface electrode occurs in this period. As the off-time decrease, a large increase of the particle size of the deposit is observed [34]. The results can be explained by taking into account that the limiting current density decreases with an increase of the duty cycle.

(3) Effect of Surface Concentration

Reaction rate and deposit structure depend on the surface concentration of the reacting species. Mass transport limits the maximum rate of deposition and influences the structure and the properties of obtained deposits. The maximum rate of mass transport in plating system corresponds to the limiting current density at which the surface concentration of the reacting species at the electrode is zero. And the limiting current density is proportional to the bulk concentration of the reacting species. That is to say, the surface concentration of the reacting species has influence on the rate of deposition and the current efficiency.

(4) Effect of Temperature

An effective control of the deposition process operating temperature is vital for the consistent performance of any deposition bath. Deviations of more than 5 ^{o}C from optimum temperature are sufficient to harm plate quality, deposition rates, and other properties. The higher temperature provides higher plating rates and the ability to operate more dilute baths without the loss of current efficiency. We have focused on the optimization of the deposition conditions using the uncatalyzed electrode, which decide the deposition parameters; current density, duty cycle, charge density and concentration of chemical species. As the deposition parameters are optimized, the fuel cell performance can be increased with higher utilization of the catalyst.

3. EXPERTIMENTAL

3. 1. Electrode preparation

The carbon slurry was made by mixing 0.1 g Vulcan XC-72 carbon powder, 0.43 mL Nafion solution (Aldrich, 5 wt.% in lower aliphatic alcohols and water, 1100 EW) with 6 mL isopropyl alcohol in an ultrasonic bath (**Figure 7**).

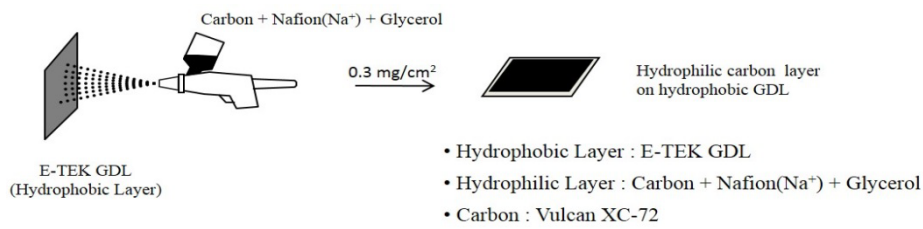

Figure 7. Preparation of uncatalyzed carbon layer.

Then, excess sodium hydroxide was added to the mixture in order to change the H^+-form of Nafion to the Na^+-form. **Figure 8** illustrates the schematic diagram of pulse electrodeposition method. To apply a uniform and flat electrode surface, the commercial gas-diffusion layer (GDL; E-TEK, LT 1200-W, Electrochem Inc.) was used as a backing layer. These steps were used to increase the current and thermal stability, respectively. The resulting carbon electrode had a hydrophilic surface due to the addition of the glycerol. The hydrophilic carbon layer was loaded with 0.3 mg cm^{-2} of carbon by spraying.

Galvanostatic pulsed electrodeposition of Pt-Co electrodes was carried out in a two-electrode cell by using an electrochemical instrument (VoltaLab80,

Radiometer). The uncatalyzed carbon electrode served as a working electrode and Pt mesh as a counter electrode. Electrodeposition was performed in a plating bath which contains the solution of 40 mM K_2PtCl_4 and various concentrations of $CoCl_2$ (20, 40, 60, 120 mM) dissolved in 0.5 M NaCl. The parameters for galvanostatic pulse electrodeposition were a peak current density of 300 mA cm^{-2}, an on/off time of 10/100 ms and a total charge density of 1 C cm^{-2}. After the electrodeposition process, the electrodes were heated at 250 ^oC in H_2 atmosphere for 30 min to remove organic solvent and reduce the oxidized catalysts. Subsequently, the electrode catalysts were performed for protonation in 0.1 M H_2SO_4 solution at 80^oC for 30 min in order to exchange again the Na^+-form of Nafion to the H^+-form.

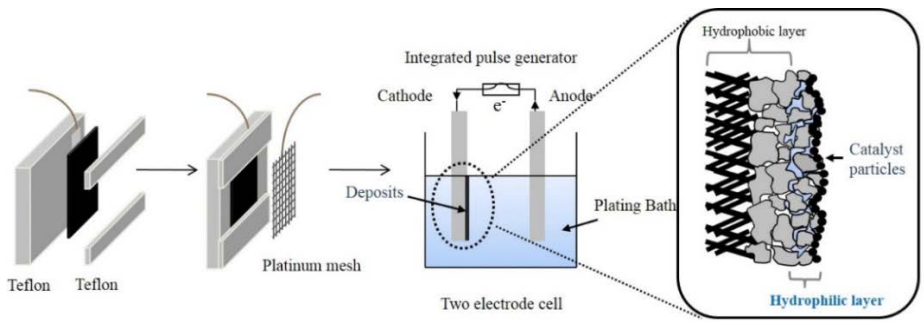

Figure 8. Schematic diagram of pulsed electrodeposition method.

3. 2. Characterization

The amount of deposited Pt-Co on the electrode was determined by using an electron probe micro-analyzer (EPMA, JEOL Co., JXA-8900R) and inductively coupled plasma-atomic emission spectroscopy (ICP-AES). The morphology and particle size of the electrodeposited Pt-Co catalysts were obtained with a high-

resolution transmission electron microscope (HR-TEM, JEOL Co., JEM-200CX). Before and after the heat treatment, the oxidation states of Pt were analyzed by X-ray photoelectron spectroscopy (XPS, Pohang Accelerator Laboratory, Beam line 4B1). Data from X-ray diffraction measurements (XRD, Philips, X'pert APD) were analyzed for the degree of alloying and lattice parameters.

3. 3. Single cell test

The catalyst slurry for the conventional electrode was prepared by thoroughly mixing the supported catalyst (40 wt.% HP Pt/C, E-TEK), Nafion solution (5 wt.%), and an appropriate amount of isopropyl alcohol. The well-mixed slurry was sprayed on a GDL (E-TEK, LT 1200-W) with 0.4 mg_{pt} cm^{-2}. The electrodeposited electrode and the sprayed electrode were placed on either side of the Nafion 112 membrane (DuPont) as the cathode and anode, respectively. The membrane electrode assembly (MEA) was hot-pressed at 100 kg_f cm^{-2} for 3 min at 130^{o}C. For comparison, conventional MEA was also prepared by spraying both electrodes using the same GDL on both sides with a Pt loading of 0.4 mg cm^{-2}. The cell performance and operating conditions were measured and controlled by a fuel cell test station (Globe Tech, Inc. 890 series, GT-500). The cell temperature was maintained at 70^{o}C with the H_2 and air gases humidified at 80^{o}C for anode and 75^{o}C for cathode, respectively. The pressure on both electrodes was maintained at 2 bar.

4. RESULTS AND DISCUSSION

Under optimized conditions, Pt-Co alloy catalysts were prepared on Nafion(Na^+)-bonded carbon layers by means of a galvanostatic method. The amount of loaded Pt and Co was controlled by changing $CoCl_2$ concentration and it was determined by ICP-AES, as shown in **Table 2**. Concentrations of Co precursor were varied from 20 to 120 mM while the concentration of Pt precursor is fixed at 40 mM. The data in Table 1 show that amounts of Pt and Co increase as the concentration of Co precursor is increased and these values are used to calculate the chemical composition. Also, the chemical composition of Pt-Co electrode was measured from energy dispersive x-ray spectroscopy (EDS) results where average results were calculated from several different data points. The compositions of electrode were observed from ICP-AES and EDS, as reported in **Table 3**. From these results, reliable chemical compositions of electrode from two analytical methods were obtained.

Table 2. Amount of Pt and Co deposits from 40 mM Pt and various concentration of $CoCl_2$.

(Measured by ICP-AES)

Sample	Pt (mg/cm^2)	Co (mg/cm^2)
20 mM $CoCl_2$	0.06899	0.06899
40 mM $CoCl_2$	0.07208	0.00676
60 mM $CoCl_2$	0.07539	0.01053
120 mM $CoCl_2$	0.08612	0.02481

Table 3. ICP-AES and EDS results of chemical composition for prepared catalysts.

Sample	Pt : Co atomic ratio	
	ICP-AES Measurement	EDS Measurement
20 mM $CoCl_2$	85 : 15	83 (±4) : 17 (±4)
40 mM $CoCl_2$	76: 24	78 (±3) : 22 (±3)
60 mM $CoCl_2$	68 : 32	64 (±3) : 36 (±3)
120 mM $CoCl_2$	51 : 49	52(±4) : 48 (±4)

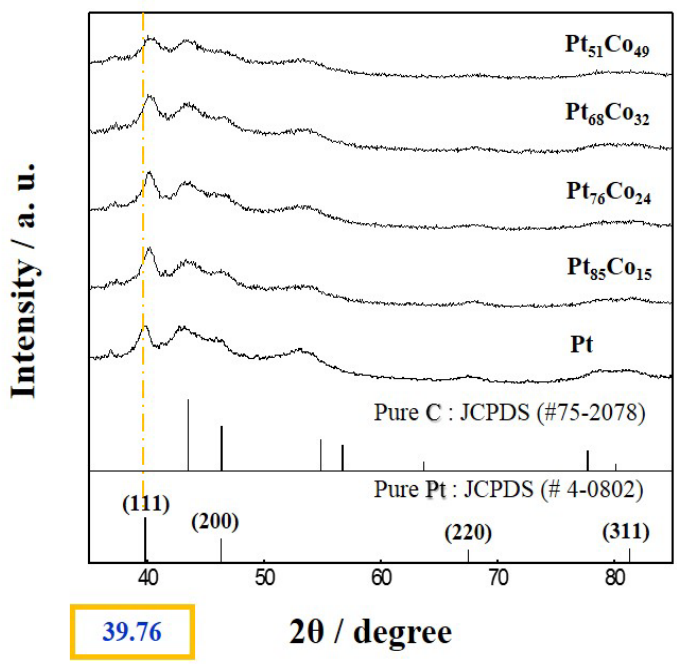

Figure 9. XRD patterns of the electrodeposited Pt-Co alloy catalysts after heat treatment (250 ^{o}C, 30 min, H_2 10% / N_2 90%).

XRD patterns were analyzed to investigate the structural change of Pt-Co alloy catalyst. As indicated in Figure 9, XRD patterns show the Pt (111), (200), (220), and (311). The lattice parameter values of Pt are 3.887 Å (Pt), 3.861 Å ($Pt_{85}Co_{15}$),

3.863 Å ($Pt_{76}Co_{24}$), 3.860 Å ($Pt_{68}Co_{32}$), and 3.859 Å ($Pt_{51}Co_{49}$) for **Figure 9**, respectively. The lattice parameter of the Pt-Co alloy catalysts smaller than that of pure Pt. The decreasing of lattice parameter results from the interpenetration of transition metals which are smaller than Pt. Also, the Pt (111) peak of Pt-Co electrodes shifts to a higher angle compared to a pure Pt peak due to the incorporation of Co atoms into Pt atoms [13, 43].

An XPS study was carried out to investigate the oxidation state of deposits before and after the heat treatment. **Figure 10** shows the x-ray photoelectron spectra of Pt 4f of the prepared electrodes after the heat treatment.

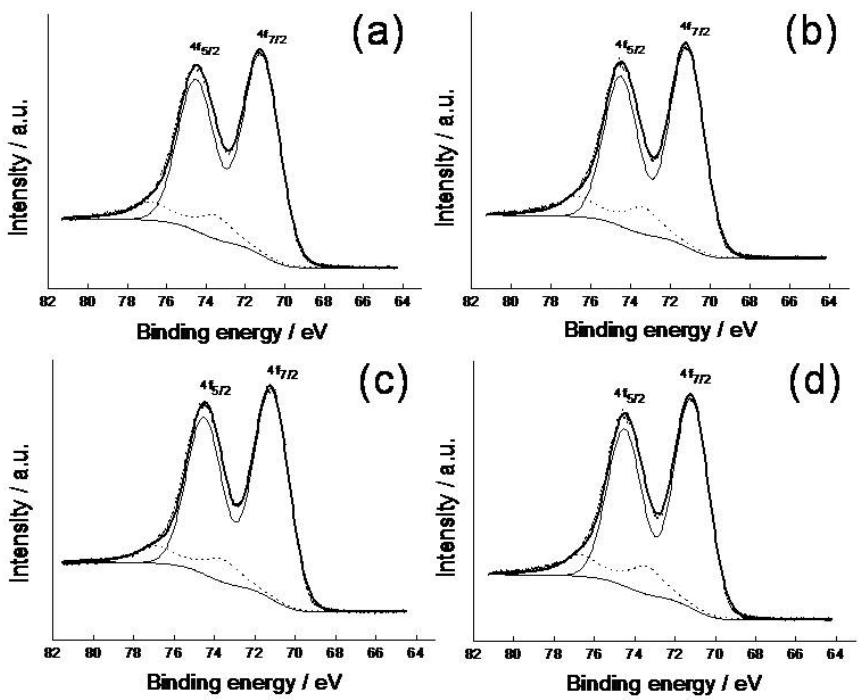

Figure 10. X-ray photoelectron spectra of Pt 4f of electrodeposited Pt-Co alloy catalysts after heat treatment: (a) $Pt_{85}Co_{15}$, (b) $Pt_{76}Co_{24}$, (c) $Pt_{68}Co_{32}$, and (d) $Pt_{51}Co_{49}$. The spectra were deconvoluted into two components labeled as Pt and Pt^{2+}.

The spectra can be deconvoluted into two components, labeled as Pt and Pt^{2+} (as PtO or $Pt(OH)_2$). The relative intensities (%) of metallic Pt deposited from different Co concentrations are almost the same and these values increases in general after heat treatment, as shown in **Table 4**. It is reasonable to assume that the reduction of oxidized Pt occurs during the heat treatment. Based on XPS measurements, the electrodeposited Pt-Co alloy catalyst was found to have originated from the higher degree of relative intensity for metallic Pt on the catalyst surface compared to that of commercial 40 wt.% Pt-Co/C catalyst (E-TEK) in the XPS measurements of previous study [43]. The XPS results on electrodeposited Pt-Co alloy catalyst showed the presence of a relatively lower Pt-oxide content on the alloys.

Table 4. Binding energies and relative intensities of deposits as observed from the Pt 4f X-ray photoelectron spectra in **Figure 10**.

Sample	**Species**	**Binding Energies of 4f $_{7/2}$ (eV)**	**Relative Intensities (%)**	
			Before Heat Treatment	After Heat Treatment
$Pt_{85}Co_{15}$	Pt	71.0	83.6	85.3
	Pt^{2+}	73.2	16.4	14.7
$Pt_{76}Co_{24}$	Pt	71.0	83.2	85.2
	Pt^{2+}	73.1	16.8	14.8
$Pt_{68}Co_{32}$	Pt	71.0	83.6	85.5
	Pt^{2+}	73.2	16.4	14.5
$Pt_{51}Co_{49}$	Pt	71.0	83.3	85.4
	Pt^{2+}	73.0	16.7	14.6

Unfortunately, we can't find any reliable peak of cobalt 2p due to low loading catalysts. A trace metal loading causes weak signal on XPS experiment.

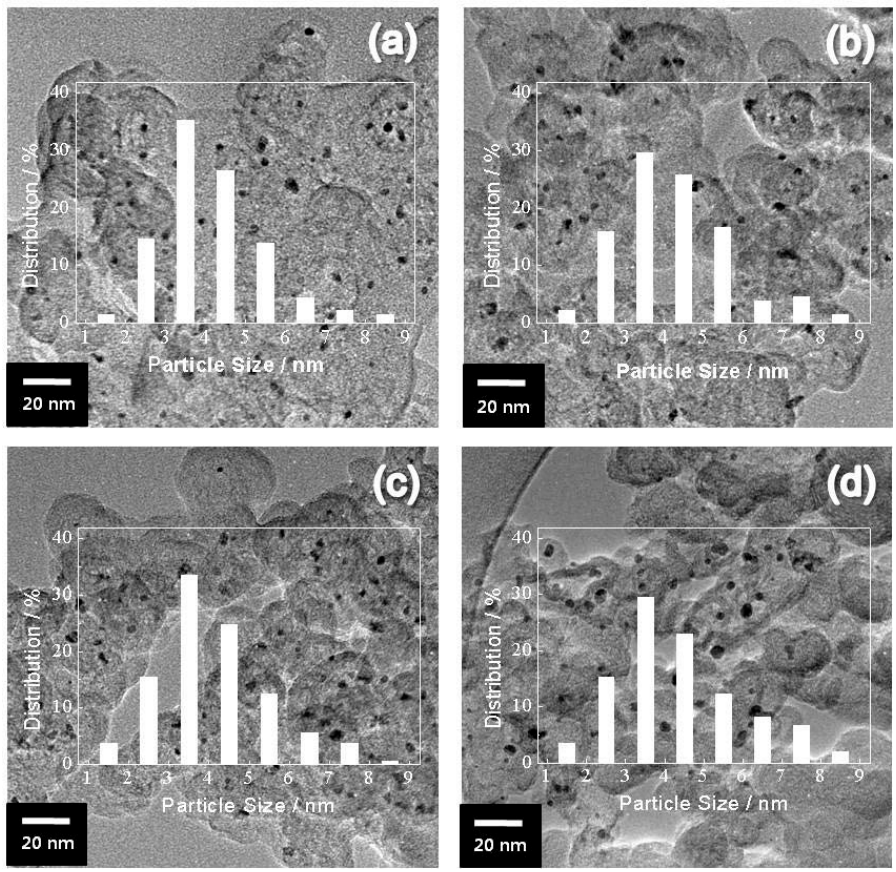

Figure 10. HR-TEM images of electrodeposited Pt-Co alloy catalysts after heat treatment: (a) $Pt_{85}Co_{15}$, (b) $Pt_{76}Co_{24}$, (c) $Pt_{68}Co_{32}$, and (d) $Pt_{51}Co_{49}$. Insets indicate the particle size distribution.

The morphology of Pt-Co particles was observed by HR-TEM, and the images are presented in **Figure 11**. These images were obtained from a series of deposits with a total charge density of 1 C cm^{-2} and various compositions. The average particle

sizes were calculated by particle distributions. Before heat treatment, size of those catalysts were 3-4 nm regardless of Co concentration (not shown here) while the average particle size of Pt-Co electrode after heat treatment at 250^{o}C in H_2 atmosphere for 30 min grew a little (3-5 nm). In order to estimate the thickness of catalyst layer, SEM images and line scan were obtained by using EPMA coupled with SEM. **Figure 11** (a) shows the cross-sectional image of MEA consisting of a conventional anode (left), pulse electrodeposited cathode (right) and Nafion membrane (middle). **Figure 11** (b) displays the cross section image of the electrodeposited electrode from $Pt_{76}Co_{24}$ catalyst. The cross section image clearly shows the three layers consisting of catalyst layer, carbon layer and carbon cloth. The thickness of catalyst layer is measured to be 5-6 μm. The thickness of the Pt catalyst layer of anode and cathode is confirmed to be 26.2 μm and 5.8 μm, as shown in **Figure 11** (c). The thickness of deposited cathode is about four times thinner than that of the E-TEK anode prepared by conventional method. Namely, the pulse electrodeposited cathode shows a high intensity of Pt peak in the thin area from the membrane. **Figure 11** (d) shows the Pt-Co concentration profile of electrodeposited cathode electrode. The electrodeposited electrode increases the number of triple-phase boundaries where reactant is in contact with catalyst and ionomer. Therefore, there is the possibility of a higher Pt-Co utilization because of the existence of abundant triple phase boundaries.

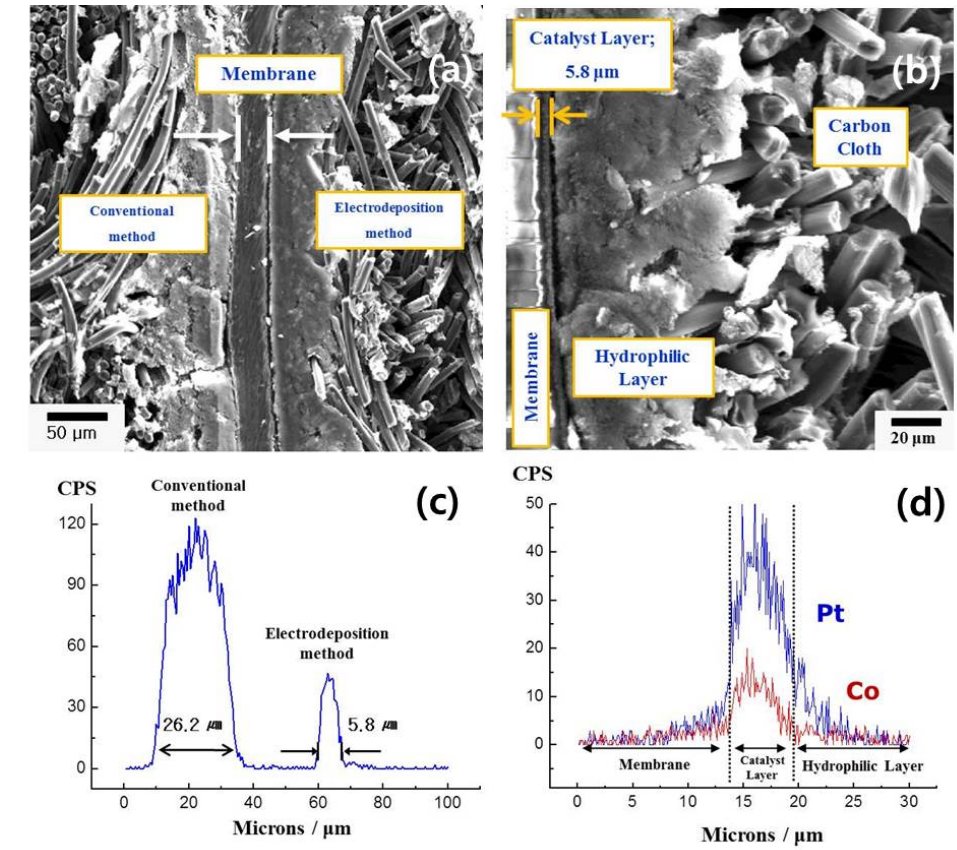

Figure 11. Cross-sectional SEM images and EPMA concentration profiles of the electrodeposited electrode from $Pt_{76}Co_{24}$ catalyst: (a) Cross-sectional image of MEA consisting of a conventional anode (left), pulse electrodeposited cathode (right) and Nafion 112 membrane (middle), (b) Cross-sectional image of pulse electrodeposited cathode, (c) Pt concentration profile of MEA, and (d) Pt-Co concentration profile of electrodeposited electrode for cathode.

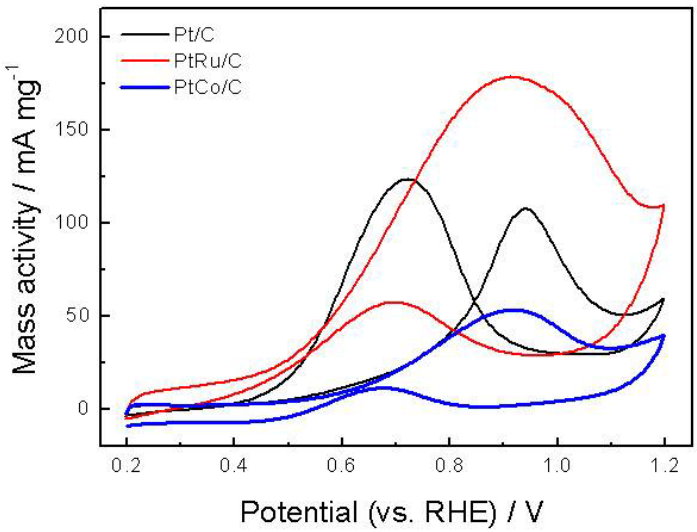

Figure 12. Voltammograms of deposited Pt/C, Pt-Ru/C, Pt-Co/C catalysts in 0.5 M CH_3OH and 0.5 M H_2SO_4 solution.

Methanol crossover results in a significant loss in coulombic efficiency and voltage efficiency of a DMFC because the Pt/C is commonly used as the cathodic catalyst, and methanol would be oxidized at the cathode [44, 45]. To avoid this problem, one is the use of oxygen reduction catalysts, which are inactive towards methanol oxidation or have a high methanol tolerance strategy is the use of oxygen reduction catalysts, which are inactive towards methanol oxidation or have a high methanol tolerance. Previous studies have proved that the use of some Pt alloy catalysts could be an efficient route to meet this requirement because the carbon-supported Pt-Cr alloy catalyst [46, 47] and bulk $Pt_{70}Ni_{30}$ alloy catalyst [48] have been found to exhibit a high methanol tolerance during oxygen reduction in comparison to pure Pt. **Figure 12** presents potential sweep voltammograms in a 0.5 M CH_3OH and 0.5

M H_2SO_4 solution at Pt/C, Pt-Ru/C, and Pt-Co/C catalysts. It is seen that the Pt-Ru/C and Pt/C catalysts exhibit enhanced catalytic activity toward methanol oxidation. However, the Pt-Co/C catalyst showed a high methanol tolerance.

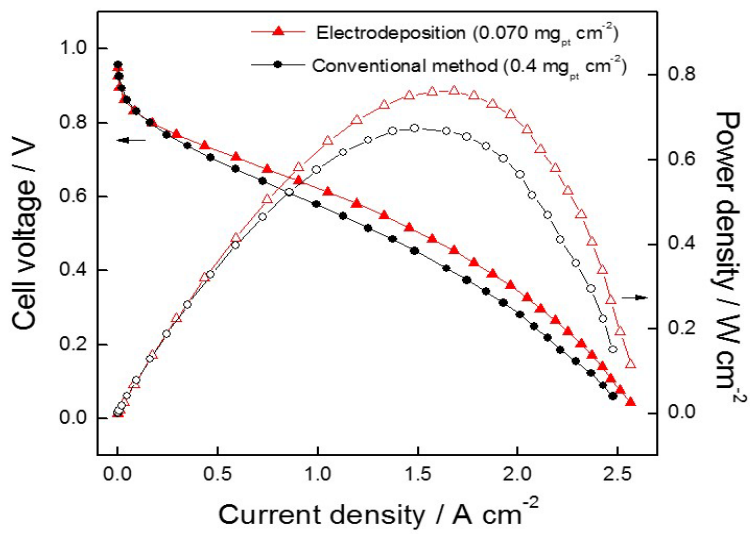

Figure 13. Current-voltage polarization curves of electrodeposited cathode catalysts and conventional method using the 40 wt.% HP Pt/C E-TEK catalyst. The anode catalyst loading was maintained at 0.4 mg_{pt} cm^{-2}. The cell temperature was maintained at 70°C with the anode H_2 and cathode air gases. The pressure on both electrodes was maintained at 2 bar: (●) pulse electrodeposited cathode with catalyst loading of 0.070 mg_{Pt} cm^{-2}, (▲) conventional electrode with Pt loading of 0.4 mg_{pt} cm^{-2}.

Figure 13 shows the polarization curves from the PEM fuel cell prepared by using two different types of cathodes. One was prepared by using the electrodeposited Pt on uncatalyzed carbon electrode and the other was prepared by conventional method using the 40 wt.% Pt/C E-TEK catalyst. The total amount of metals in the cathode was determined as 0.070 mg_{Pt} cm^{-2} by ICP-AES. While conventional MEA

were fabricated by spraying the catalyst slurry with 0.4 mg_{Pt} cm^{-2} on GDL on the cathode side. The current densities are 1.051 A cm^{-2} and 0.858 A cm^{-2} at 0.6 V for pulse electrodeposited electrode and conventional electrode, respectively. In comparison with the conventional electrode made with catalysts from the E-TEK, the electrode prepared by electrodeposition contains only 17.5 % of catalyst of the E-TEK shows a better performance in almost the entire current density regions. It is certain that a less amount of Pt is required with the electrodeposition method to exhibit the same performance as the electrodes prepared by the conventional method.

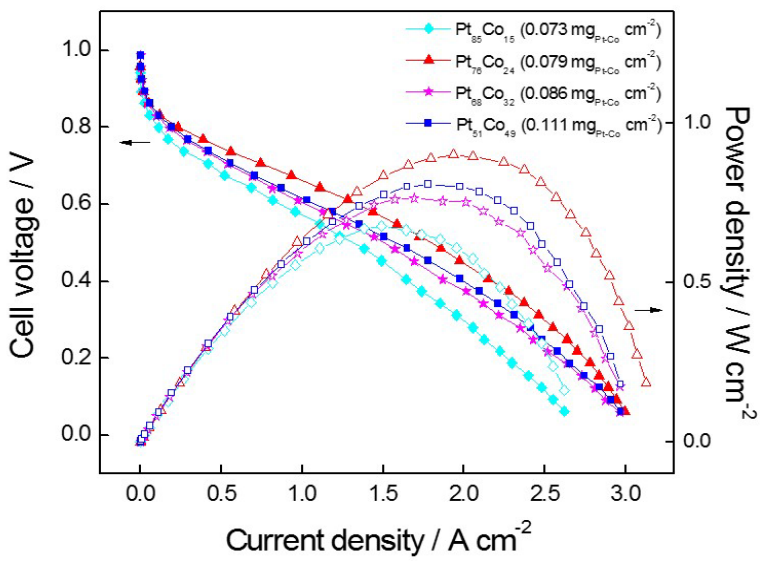

Figure 14. Current-voltage polarization curves of the electrodes prepared with different Pt-Co compositions. The electrodeposited electrodes were used as the cathode. The anode catalyst loadings were maintained at 0.4 mg_{pt} cm^{-2}. The cell temperature was maintained at 70 ^{o}C with the anode H_2 and cathode air gases. The pressure on both electrodes was maintained at 2 bar: (◆) $Pt_{85}Co_{15}$, (▲) $Pt_{76}Co_{24}$, (★) $Pt_{68}Co_{32}$, and (■) $Pt_{51}Co_{49}$.

Figure 14 presents the mass activities of the electrodes prepared with different Pt-Co compositions. The electrodeposited electrodes were used as the cathode. The electrodeposition method was prepared from 40 mM K_2PtCl_4 and various concentrations of $CoCl_2$ dissolved in 0.5 M NaCl. A anode was made from the slurry mixed commercial 40 wt.% HP Pt/C E-TEK, Nafion solution and isopropyl alcohol. The mixture was sprayed on GDL with 0.4 mg cm^{-2} of Pt. The electrodeposited Pt-Co electrodes exhibit better performance than electrodeposition Pt electrode. The Pt-Co catalysts with 76 : 24 (obtained from a solution containing 40 mM K_2PtCl_4 and 40 mM $CoCl_2$) were found to provide the highest single cell performance among the compositions studied. These results are in agreement with previous result, the optimum atomic ratio of 3 : 1 Pt-Co [8, 13, 52-54].

5. CONCLUSION AND PERSPECTIVE

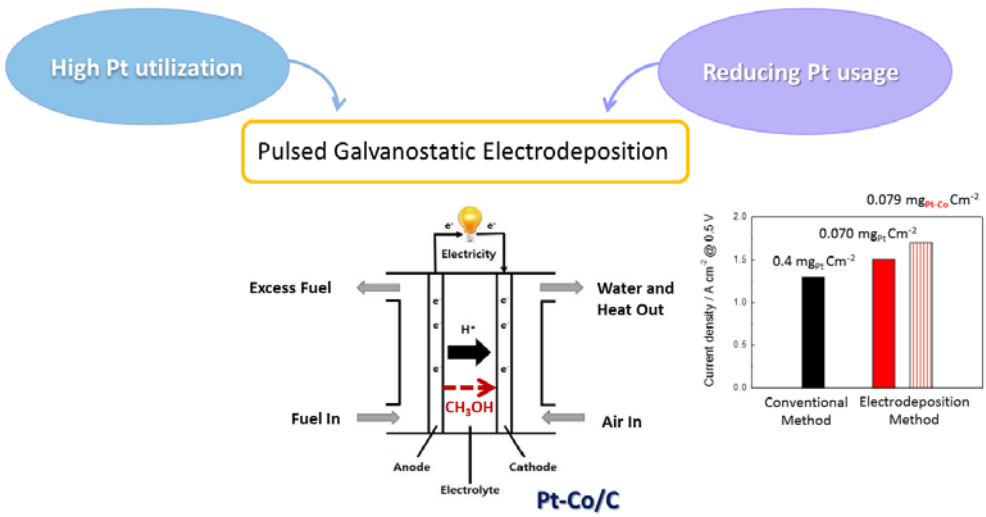

The characteristics and single cell performance of cost-effective Pt-Co catalysts, prepared on uncatalyzed carbon electrode by galvanostatic pulse electrodeposition have been evaluated. The chemical composition of the electrodes could be controlled by varying the concentration of Co precursor. We observed that Pt-Co catalysts evenly exist on the surface of carbon electrode and the thickness of Pt-Co catalysts layer was about 5.8 μm. From XPS studies, Pt 4f spectrum of catalyst indicated the presence of oxidation states Pt^{2+} in addition to metallic Pt. The Pt-Co catalysts with 76 : 24 were found to provide the highest single cell performance among the compositions studied. Improved mass activity of Pt-Co alloy catalysts indicated a definite increase of utilization efficiency.

6. REFERENCES

[1] H.A. Gasteiger, J.E. Panels, S.G. Yan, *J. Power Sources*, 127 (2004) 162.

[2] M.S. Wilson, S. Gottesfeld, *J. Electrochem. Soc.*, 139 (1992) L28.

[3] S.Y. Cham W.M. Lee, *J. Electrochem. Soc.*, 146 (1999) 4055.

[4] M.S. Wilson, J.A. Valerio, S. Gottesfeld, *Electrochim. Acta*, 40 (1995) 355.

[5] P. Stonehart, Ber. Bunsenges, *Phys. Chem.*, 94 (1990) 913.

[6] M. Watanabe, K. Tsurumi, T. Mizukami, T. Nakamura, P. Stonehart, *J. Electrochem. Soc.*, 141 (1994) 2659.

[7] A. Seo, J. Lee, K. Han, H. Kim, *Electrochim. Acta*, 52 (2006) 1603.

[8] T. Toda, H. Igarashi, H. Uchida, M. Watanabe, *J. Electrochem. Soc.*, 146 (1999) 3750.

[9] B.C Beard, P.N. Ross, *J. Electrochem. Soc.*, 137 (1990) 3368.

[10] S. Mukerjee, S. Srinivasan, M.P. Soriaga, J. McBreen, *J. Phys. Chem.*, 99 (1995) 4577.

[11] L. Xiong, A. Manthiram, *J. Electrochem. Soc.*, 152 (2005) A697.

[12] S. Koh, J. Leisch, M.F. Toney, P. Strasser, *J. Phys. Chem. C*, 111 (2007) 3744.

[13] M-K. Min, J. Cho, K. Cho, H. Kim, *Electrochim. Acta*, 45 (2000) 4211.

[14] S.C. Zignani, E. Antolini, E.R. Gonzalez, *J. Power Sources*, 182 (2008) 83.

[15] E.I. Santiago, L.C. Varanda, H.M. Villullas, *J. Phys. Chem. C*, 111 (2007) 3146.

[16] L. Xiong, A. Manthiram, *Electrochim. Acta*, 50 (2005) 2323.

[17] Y. Ra, J. Lee, In Kim, S. Bong, H. Kim, *J. Power Sources,* 187 (2009) 363.

[18] J. Lee, J. Seo, K. Han, H. Kim, *J. Power Sources,* 163 (2006) 349.

[19] F. Alcaide, O. Miguel, H.J. Grande, *Catal. Today,* 116 (2006) 408.

[20] H. Kim, N.P. Subramanian, B.N. Popov, *J. Power Sources,* 138 (2004) 14.

[21] S.D. Thompson, L.R. Jordan, M. Forsyth, *Electrochim. Acta,* 46 (2001) 1657.

[22] A. Ioselevich, A.A. Kornyshev, W. Lehnert, *Solid State Ionics,* 124 (1999) 221.

[23] E.J. Talyor, E.B. Anderson, N.R.K. Vilambi, *J. Electrochem. Soc.,* 139 (1992) L45.

[24] O. Antoine, R. Durand, Electrochem. *Solid-State Lett.,* 4 (2001) A55.

[25] A.J. Appleby, E.B. Yeager, Assessment of Research Needs for Advanced Fuel Cells, Pergamon, New York, 1986.

[26] S. Srinivasan, E.A. Ticianelli, C.R. Derouin, A. Redondo, *J. Power Sources,* 22 (1988) 359.

[27] E.A. Ticianelli, C.R. Derouin, A. Redondo, S. Srinivasan, *J. Electrochem. Soc.,* 135 (1998) 2209.

[28] K.A. Mauritz, R.B. Moore, *Chem, Rev.,* 104 (2004) 4535.

[29] R.B. Moore, C.R. Martin, *Anal. Chem.,* 58 (1986) 2569.

[30] K.A. Page, K.M. Cable, R.B. Moore, *Macromolecules,* 38 (2005) 6472.

[31] S.R. Samms, S. Wasmus, R.F. Savinell, *J. Electrochem. Soc.,* 143 (1996) 1498.

[32] Y.Q. Wang, Y. Kawano, S.R. Aubuchon, R.A. Palmer, *Macromolecules,* 36 (2003) 1138.

[33] S.C. Yeo, A. Eisenberg, *J. Appl. Poly. Sci.,* 21 (1977) 875.

[34] K.H. Choi, H.S. Kim, T.H. Lee, *J. Power Sources*, 75 (1998) 230.

[35] J-C.L. Puippe, F. Leaman (Eds.), Theory and Practice of Pulse Plating, AESF Soc., Orlando, FL, 1986, p.73.

[36] M.P. Hogarth, J. Munk, A.K. Shukla, A. Hamnett, *J. Appl. Electrochem.*, 24 (1994) 85.

[37] M. Paunovic, M. Schlesinger, Fundamentals of Electrochemical Deposition, 1998, J. Wiley and Sons, Inc.

[38] D. Lendolt, A. Marlot, *Surf. Technol.*, 169-170 (2003) 8.

[39] O. Dossenbach, in: J-C. Puippe, F. Leaman (Eds.), Theory and Practice of Pulse Plating, AESF Soc. Orlando, FL, 1986, 73

[40] M. Mastragostino, A. Missirolo, F. Soavi, *J. Electrochem. Soc.*, 8 (2005) A110.

[41] G. Wu, L. Li, B.Q. Xu, *Electrochem. Acta*, 50 (2004) 1.

[42] Z. He, J.J. Chen, D. Lui, H. Tang, W. Deng, Y. Kuang, *Materials Chemistry and Physics*, 85 (2004) 396.

[43] A.S. Arico, A.K. Shukla, H. Kim, S. Park, M. Min, V. Antonucci, *Appl. Surf. Sci.*, 172 (2001) 33.

[44] B. Gurau, E.S. Smotkin, *J. Power Sources*, 112 (2002) 339.

[45] A. Arico, P. Creti, P.L. Antonucci, V. Antonucci, Electrochem. *Solid-State Lett.*, 1 (1998) 66.

[46] H. Yang, N. Alonso-Vante, J.-M. Le´ger, C. Lamy, *J. Phys. Chem. B*, 108 (2004) 1938.

[47] R.C. Koffi, C. Coutanceau, E. Garnier, J.-M. Leger, C. Lamy, *Electrochem.*

Acta, 50 (2005) 4117.

[48] J.-F. Drillet, A. Ee, J. Friedemann, R. Kötz, B. Schnyder, V.M. Schmidt, *Electrochim. Acta,* 47 (2002) 1983.

PART 2

DESING OF A NEW SUPPORT MATERIAL

1. INTRODUCTION

Many research groups have recently made efforts to understand the influence of carbon support properties on the activity of fuel cell electrocatalysts. Carbon is an ideal material for supporting nano-sized metallic particles in an electrode for low temperature polymer fuel cells [1-3]. No materials other than carbon have the essential properties of electronic conductivity, corrosion resistance, surface properties, and low cost required for the commercialization of fuel cells. Carbon materials affect many vital properties of supported metal catalysts, in particular: (i) metal particle size, morphology and size distribution [4, 5]; (ii) extent of alloying in bimetallic catalysts [6]; (iii) stability of supported metal nanoparticles towards particle growth and agglomeration; (iv) electrocatalytic activity, e.g. due to metal-support interactions; (v) degree of catalyst utilization; (vi) mass transport in the catalytic layer; (vii) electronic conductivity of the catalyst layer and thus its ohmic resistance, etc. [7, 8].

Carbon black is currently the most widely used carbon material for the preparation of supported catalysts because this carbon material contains a small portion of micropores and a large surface area sufficient to accommodate a high loading of the metal phase. Carbon black is formed in the gas phase by the thermal decomposition of hydrocarbons [9]. Common carbon blacks include acetylene black, Vulcan XC-72, Ketjen Black, Black Pearl, etc., which possess different physicochemical characteristics, such as specific surface area, electronic

conductivity, stability and surface functionality.

Recently, graphene has been studied as a catalyst support due to its excellent conductivity, remarkable mechanical strength and high specific surface area [10-19]. Various techniques including mechanical exfoliation, epitaxial growth and chemical vapor deposition have been developed for producing graphene. Among them, chemically synthesized graphene using either graphite or a graphite derivative as the starting material has been found to be a useful component in various composites, potentially improving and controlling their properties [20, 21]. Graphene may serve as a support material to anchor nanoparticle catalysts in order to improve electron transport, which provides possibilities in the design of next-generation catalysts with enhanced interactions between the substrate and the catalysts. In a previous study, we reported that a PtRu/graphene was used as an electrocatalyts for improving methanol oxidation [16]. However, the surface area of graphene decreases considerably when separated sheets aggregate together due to van der Waals force and π–π interaction [22-24], this will influence the utility and activity of the catalysts supported on them. Although the use of metal nanoparticles has been proposed for separating the graphene sheets, there has been some difficulty in creating a triple-phase boundary in a catalyst layer.

In this part, we tried to provide a better approach of reactants into PtRu catalysts *via* the addition of a nano-sized spacer between graphene sheets. Also, we investigated the feasibility of a novel chemically activated graphene-supported electrocatalyst.

2. LITERATURE SURVEY

2. 1. Various carbon supports for fuel cells

Carbon plays an important role in fuel cell catalyst because of its good electrical and thermal conductivities, low density, adequate corrosion resistance, low thermal expansion, low elasticity, and high purity (**Figure 1**). In general, fuel cell catalysts consist of nano-sized metal particles deposited on carbon supports, therefore, the metal particles expose the active sites whereas the support acts as an anchor for these particles, thus preventing sintering. Extensive effort has been devoted to determining the optimum carbon as supports which supply enough surfaces in the dispersion of nanoparticles.

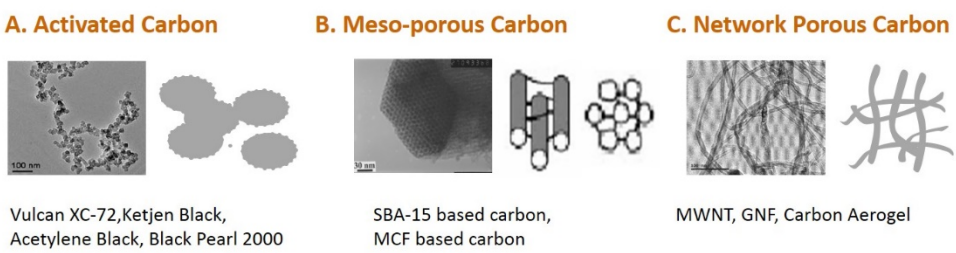

Figure 1. Various carbon supports.

(1) Activated carbon

Activated carbons are commonly used as supports for DMFC anode catalysts. There are many types of carbon blacks, such as Acetylene Black, Vulcan XC-72, Ketjen Black, etc., and these are usually manufactured by pyrolyzing hydrocarbons

such as natural gas or oil fractions taken from petroleum processing. These carbon blacks show different physical and chemical properties, such as specific surface area, porosity, electrical conductivity and surface functionality. Among these factors, specific surface area has a significant effect on the preparation and performance of supported catalysts. Generally, highly dispersed, supported catalysts cannot be prepared from low-surface-area carbon blacks (e.g., Acetylene Black). High surface-area carbon blacks (e.g., Ketjen Black) could support highly dispersed catalyst nanoparticles. However, Ketjen Black supported catalysts showed high Ohmic resistance and mass transport limitation during fuel cell operation. Vulcan XC-72 with a surface area of $\sim 250\ m^2\ g^{-1}$ has been widely used as a catalyst support, especially in DMFC anode catalyst preparation. An accessible and sufficiently large surface for maximum catalyst dispersion has been argued to be a necessary but insufficient condition for obtaining optimized carbon supported catalysts. Other factors, such as pore size and distribution, and surface functional groups of carbon blacks, also affect the preparation and performance of carbon black supported catalysts.

(2) Carbon nanotube

Carbon nanotubes were discovered in 1991 by Sumio Iijima of NEC and are practically long, thin cylinders of graphite sheet [25] and large-scale synthesis have been investigated, due to their high mechanical and unique electrical properties [26, 27]. In CNT the graphitic planes run parallel to the central axis, implying that in

this compound only basal planes are exposed. These materials are also referred to as multi-walled carbon nanotubes (MWNT) or parallel carbon nanofibers. If the fiber consists of only one graphite sheet that is oriented in a parallel way to the fiber axis it is called a single-walled carbon nanotube (SWNT). This carbon of which surface is graphene sheet is so inert that the introduction of oxygen-containing groups by treatment of this material with an oxidizing agent, *e.g.*, nitric acid [28-30]. These functional groups ensure wettability with water and other polar solvents and enable the anchoring of an active phase or its precursor. A number of studies relating to the synthesis of CNT supported catalysts and their application in heterogeneous catalysis have been reported [28, 30-38]. However, the reasons why CNT supported catalysts show high performances in fuel cell application have not been discussed clearly.

(3) Carbon nanofiber

Carbon nanofiber (CNF) can be produced at relatively low costs with a high yield and are therefore suitable as catalyst support material [38-42]. It can be prepared in a reproducible manner, with tunable properties, making these fibers a support with great potential. One of the most outstanding features of these structures is the presence of a large number of edges, which in turn constitute sites that are readily available for chemical and physical interactions. In CNF the graphitic planes are oriented at an angle to the central axis, thus exposing graphite edge planes. The CNFs are classified as possessing a ‘platelet’ structure where the graphite platelets

in the carbon materials are oriented perpendicular to the fiber axis, a ‘spiral’ form where the platelets in the helical CNFs are oriented parallel to the fiber axis, a ‘ribbon’ structure where the graphite platelets are aligned parallel to the fiber axis, and a ‘herring-bone’ structure where graphene sheets are stacked in a ‘fishbone’ way. Among these types of CNFs ‘platelet’ and ‘spiral’ graphite CNFs possess a structure in which the graphite sheets are oriented in a direction perpendicular to the growth axis and since the layers maintained a minimum interlayer spacing of 0.355 nm, this well-ordered arrangement can act as a template for subsequent deposition of metals (**Figure 2**).

The production of reactive carbon intermediates from a carbon source is a crucial step in the synthesis of CNF. This can be achieved by activation of graphite by laser vaporization, by electric arc-discharge, or by the dissociation of a carbon-containing gas (*e.g.*, CH_4, CO, and C_2H_4) on the surface of a suitable metal catalyst like Ni, Fe, or Co. Only the latter route, the catalytic synthesis route, very pure carbon nanofibers can be produced in large quantities, while tuning of physico-chemical properties like surface structure, mean diameter, density, and morphology is possible.

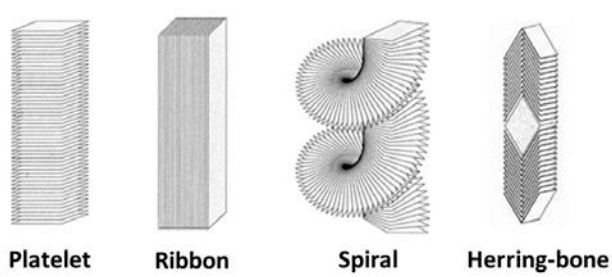

Figure 2. Schematic representations of four main types of carbon nanofiber (CNF).

(4) Graphene

Graphene is the name given to a two-dimensional sheet of sp^2-hybridized carbon. Its extended honeycomb network is the basic building block of other important allotropes; it can be stacked to form 3D graphite, rolled to form 1D nanotubes, and wrapped to form 0D fullerenes. Long-range π-conjugation in graphene yields extraordinary thermal, mechanical, and electrical properties, which have long been the interest of many theoretical studies and more recently became an exciting area for experimentalists. Graphene has potential applications in various fields such as energy electrodes, transparent electrodes (**Figure 3**).

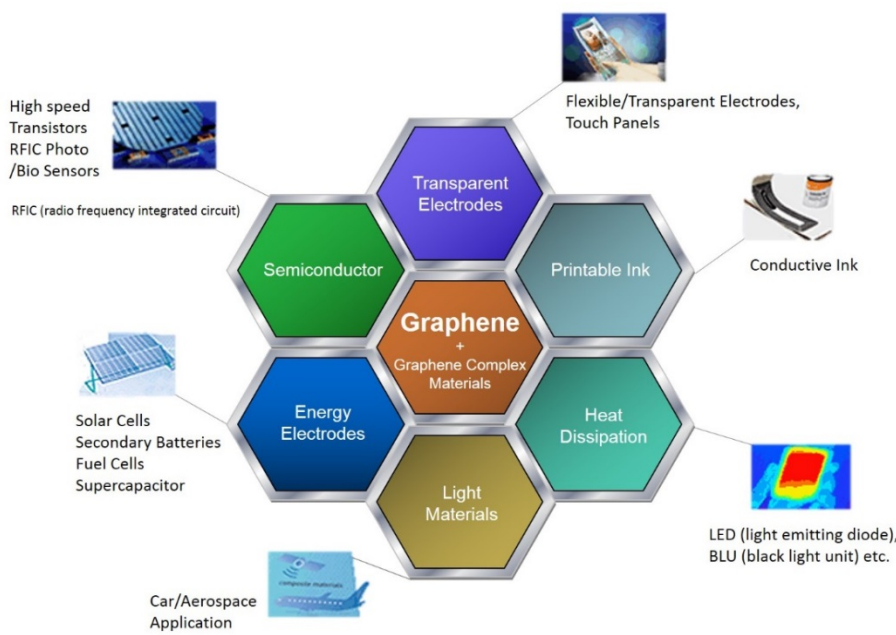

Figure 3. Applications of graphene.

While studies of graphite have included those utilizing fewer and fewer layers for some time, the field was delivered a jolt in 2004, when Geim and co-workers at Manchester University first isolated single-layer samples from graphite [43]. These mechanical exfoliation technique used by the Manchester group isolated the two-dimensional crystals from three-dimensional graphite [44]. Many methods including mechanical exfoliation, chemical exfoliation, epitaxial growth, and chemical vapor deposition have been developed for producing graphene (**Table 1**).

As recently demonstrated, graphene can be obtained in bulk quantity by chemical reduction of graphene oxide in solution. Because chemical reduction of graphene oxide easily obtains many grams as compared to mechanical method, many groups have been widely investigated on this topic [45-47].

Table 1. Synthesis method of graphene

	Exfoliation	**Epitaxial Growth**	**Chemical Vapor Deposition**
Structure	One- of few- layered graphene oxide nanoshees	Graphene films	Patterned graphene films
Property	To be blended with other components to synthesize functional composites	To be used in electronic devices such as field effect transistors	To be used as transparent conductive films for device fabrication

(5) Porous graphene

Porous graphene is a collection of graphene-related materials with pores in-plane and out-of-plane (**Figure 4**). Depending on the production techniques used, the pore size ranges from atomic precision to macro scale. As a result of the pores of graphene, porous graphene exhibits properties distinct from those of pristine graphene, leading to its potential applications in numerous fields such as energy storage [48-51], gas purification [52, 53].

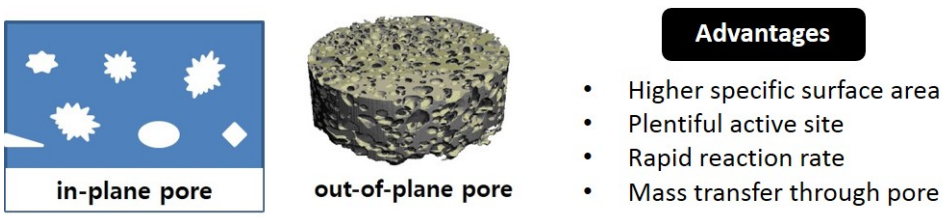

Figure 4. In-plane/out-of-plane pore by pore structure dimension.

2. 2. Preventing graphene sheets from restacking

Graphene has attracted increasing attention in the past several years due to its high surface area, remarkable thermal conductivity, excellent electronic conductivity and mechanical properties [10, 11]. Unfortunately, graphene from chemical reduction of graphite oxide (GO) often results in the aggregation or restacking due to the intersheet van der Waals attractions [54], and consequently significant degradation of the unique properties of individual sheets, such as high specific surface area and fast ion transport behaviors.

To fully utilize and further explore the new functions of graphene, many researchers try to design out-of- plane space by introducing spacer in-between graphene layers, such as metal oxides [55, 56], metal hydroxide [57, 58], conducting polymer [59-61], and carbon nanotubes [62-66] which makes the electroactive area more accessible, resulting in enhanced electrochemical performances for fuel cell, supercapacitors and Li-ion batteries. Recently, porous graphene materials including graphene nanomesh (in-plane pores in graphene sheets), crumpled graphene and graphene foam have been extensively studied. Due to their unique porous structure combined with the inherent properties of graphene, porous graphene materials have a higher surface area and much more space for the transportation or storage for the electron/ion, gas and liquid.

3. EXPERIMENTAL

3.1. Preparation of graphene oxide

Graphene oxide was synthesized using the modified Hummers method reported by Kovtyukhova et al [67]. Synthesized graphene oxide was suspended in water (0.05 wt.%) to give a brown dispersion. Exfoliation of the graphene oxide was achieved through ultrasonication for 3 h and then subsequently dialyzed (12–14 kDa cut-off) for 6 h to remove any residual salts and acids. The obtained solution was then subjected to 20 min of centrifugation at 3000 rpm to remove any unexfoliated graphene oxide [68, 69]. Finally, the precipitate was dried at 70°C overnight.

3.2. Preparation of chemically activated graphene

500 mg of GO was dispersed in 20 ml of deionized water with ultrasonication for 20 min. 3 g of KOH was added to the solution 50 followed by ultrasonication for another 20 min. The solution was impregnated with stirring at room temperature for 6 h and dried at 120^{o}C. The powdered mixture was heated at 280^{o}C for 1 h to evaporate residual water and then to it was heated at 800^{o}C for 1 h under N_2 gas atmosphere for activation in a quartz furnace. After washing the product with deionized water several times, it was dried at 80^{o}C overnight, and then the activated graphene was obtained [70, 71].

3.3. Synthesis of PtRu/graphene-Vulcan carbon and PtRu/activated graphene

A PtRu alloy catalyst supported on graphene–Vulcan carbon was prepared using an improved impregnation method [72], applying HCHO as a reducing agent and HCl as an acidic sedimentation promoter. H_2PtCl_6 (Aldrich) and $RuCl_3$ (Aldrich) were used as metal precursors. The atomic ratio of platinum to ruthenium was adjusted to 1:1. Graphene oxide and Vulcan carbon (VULCAN XC-72, Cabot Corp.) were used as supports to make 40 wt.% PtRu/graphene–Vulcan carbon catalysts (**Figure 5**). The graphene oxide and Vulcan carbon ratio varied between 0 and 100 wt.%. Also, the activated graphene was used as a support to obtain 40 wt.% PtRu/activated graphene. The prepared catalysts were heat-treated at 300°C in 10% H_2 in N_2 atmosphere to reduce the oxidized catalysts. For a comparison, 40 wt.% PtRu/graphene and PtRu/Vulcan carbon catalysts were also prepared in the same manner.

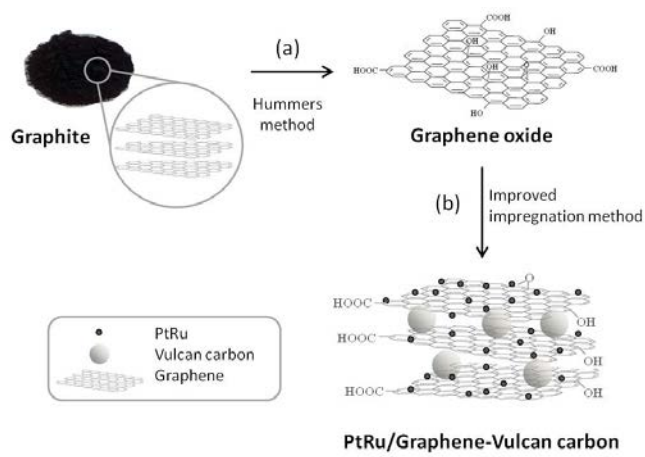

Figure 5. Schematic illustration of facile synthesis of graphene-Vulcan carbon composite. (a) Chemical oxidation using modified Hummers method and (b) preparation of PtRu/graphene-Vulcan carbon catalyst using an improved impregnation method.

3.4. Characterization

The chemical states of the component elements were analyzed through XPS (AXIS-His spectrometer, KRATOS) using a monochromatic Al Ka X-ray source (1486.6 eV) with a 12 kV voltage and 10 mA current. The binding energies were shifted for charging using C 1s to 284.6 eV. The C 1s signals were collected and analyzed based on the deconvolution of the spectra using XPS peak software. Atomic force microscopy (AFM) images of the layers deposited on SiO_2/Si substrates were obtained using a Digital Instruments XE150 (PSIA) in tapping mode. Typical images were obtained at line scan rates of 1 Hz and 256 × 256 pixel samples were collected. A high-resolution transmission electron microscope (HR-TEM, JEM-3010, JEOL) and field-emission scanning electron microscope (FE-SEM, JSM-6700F, JEOL) were used to check the morphology of the catalysts. The crystallinity of the samples was determined through X-ray diffraction (XRD) performed using a M18XHF-SRA (MAC science Co.) diffractometer equipped with nickel-filtered Cu Ka radiation at a scan rate of 5° min^{-1} (2-theta). The X-ray gun was operated at 50 kV and 200 mA.

3.5. Electrochemical measurements

All electrochemical experiments were performed using an Autolab potentiostat (Metrohm, USA) with a conventional 3-electrode system. The electrochemical cell consists of a glassy carbon electrode (3 mm diameter, Bioanalytical Systems, Inc.) as the working electrode, Ag/AgCl (Bioanalytical Systems, Inc.) as the reference

electrode, and platinum wire as the counter electrode. All potentials determined through the electrochemical measurements were converted to the reversible hydrogen electrode (RHE) scale. The scan rate used during the CV measurement was 20 mV s^{-1}. The working electrodes were prepared as follows: a glassy carbon electrode, polished to a mirror finish with a 0.05 mm alumina suspension (Buehler, Lake Bluff, MN, USA) before each experiment, was used as a substrate for the catalysts during the electrochemical measurements. A mixture of the catalyst, 5 wt.% Nafion solution, 2-propanol, and distilled water were ultrasonically homogenized. For the measurements, a thin compact layer of the mixture was cast onto the glassy carbon electrode. A measured volume of this mixture was dropped onto the glassy carbon surface, which enabled the calculation of the catalyst loading. The electrochemical activity of the methanol oxidation reaction was measured using linear sweep voltammetry at a scan rate of 20 mV s^{-1} at 25°C in a 1 M CH_3OH and 1 M H_2SO_4 solution. The electrochemically active surface area (ECA) of the prepared catalysts was determined using CO-stripping voltammetry in 1 M H_2SO_4 solution. CO adsorption was achieved at 0.1 V versus RHE in a CO saturated solution for 10 minutes and the electrolyte was purged with nitrogen for 10 min to remove CO on the surface. The amount of CO_{ads} was evaluated by integrating the stripping peak of CO_{ads}, which was corrected for the electric double-layer capacitance. The electrochemical surface area of the PtRu metal was obtained using two assumptions: (1) the monolayer of the linearly adsorbed CO was established, and (2) the coulombic charge required for oxidation was 420 mC cm^{-2}

[72, 73]. Chronoamperometry curves were measured at 0.7 V for 3600 s in 1 M CH_3OH and 1 M H_2SO_4.

3.6. Single cell test

The polymer electrolyte membrane fuel cell tests of the prepared catalysts were performed with respective anode electrocatalysts under the same operating conditions. To fabricate the membrane electrode assembly (MEA), the catalyst slurry for the electrode was prepared by thoroughly mixing catalysts, Nafion solution (5 wt.%), and an appropriate amount of isopropyl alcohol. The well-mixed slurry was sprayed on a GDL (E-TEK, LT 1200-W) with 0.4 mg_{PtRu} cm^{-2} for the anode. The Pt/C (E-TEK, 40 wt.%) catalyst slurry with 0.4 mg_{pt} cm^{-2} was applied for the cathode. The anode and cathode electrodes were placed on both sides of a Nafion 112 membrane (DuPont). The MEA was hot-pressed at 9800 kPa for 3 min at 130°C. The cell performance and operating conditions were measured and controlled by a fuel cell test station (Globe Tech, Inc. 890 series, GT-500). The cell temperature was maintained at 70°C with the anode H_2 and cathode air gases.

4. RESULTS AND DISCUSSION

4.1. Addition of a nano-sized spacer between graphene sheets (PtRu/graphene-Vulcan carbon)

Surface chemical information was obtained using X-ray photoelectron spectroscopy (XPS). The main signals present on the survey spectra of the graphene oxide and graphene are due to C and O. The high-resolution C 1s XPS spectra are shown in **Figure 6** (a). The C 1s peak of the graphene oxide consists of C-C (sp^2 carbon in the basal plan, 284.6 eV), C-O (286.6 eV), C=O (288.1 eV) and O-C=O (289 eV). The contribution of C-O is particularly high. After a reduction using formaldehyde, the O/C ratio decreases notably in graphene, indicating that a large majority of the oxygenated species is removed [74, 75]. In addition, a broad and weak peak centered above 290.0 eV is identified as a shake-up satellite due to π–π* transitions [76]. To assess the reduction of graphene oxide, Fourier transform infrared (FT-IR) spectra of the nanostructures were recorded (**Figure 6** (b)). The FT-IR spectrum of graphene oxide shows the presence of various oxygen-containing groups, including O-C=O ($\nu_{O\text{-}C=O}$ at 840 cm^{-1}), C-OH ($\nu_{C–OH}$ at 1220 cm^{-1}), O-H ($\nu_{O–H}$ at 1400 cm^{-1}) and carboxyl functional moieties at 1730 cm^{-1}, which are formed owing to the strong oxidation process [77]. On the other hand, in the case of graphene, most of the contributions from the oxygen-containing groups decrease after reduction using formaldehyde.

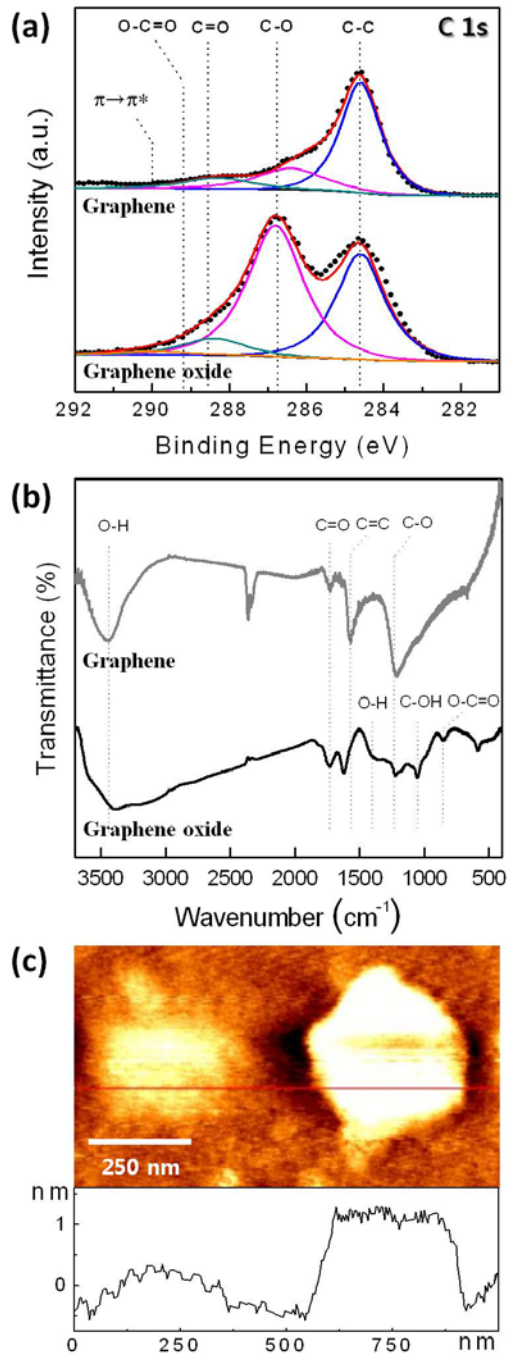

Figure 6. (a) XPS spectra of graphene oxide and graphene, (b) FT-IR spectra of graphene oxide and graphene, and (c) tapping-mode AFM image of graphene on SiO_2/Si substrate.

Tapping-mode atomic force microscopy (AFM) shows that the graphene sheet was flat, with a thickness of ~ 1.48 nm (**Figure 6** (c)). The measured thickness is larger than the theoretical value of a perfectly flat sp^2-carbon atom network (~0.32 nm). It is assumed that this difference results from oxygen-containing functionalities such as epoxy and hydroxyl groups, intrinsic out-of-plane deformation of graphene, and an instrumental offset arising from different interactions between the AFM cantilever, graphene sheet, and substrate [69, 74].The crystal structures of the graphene oxide, graphene sheet and prepared catalysts were characterized using XRD, the results of which are shown in **Figure 7** (a). The XRD pattern of graphene oxide showed a well-defined (002) peak at 10.5°. After a chemical reduction using formaldehyde, the graphene oxide was reduced to graphene with a peak at 24.7° [75]. Additionally, XRD data of PtRu catalysts loaded onto supporting materials are shown in **Figure 7** (a). The Pt (111) peak observed from all alloy catalysts shifts slightly toward a higher value compared with pure Pt. This shift indicates that the alloy is formed between the Pt and Ru [72, 78].

The surface morphology of the PtRu/graphene–Vulcan carbon was observed using a high-resolution transmission electron microscopy (HR-TEM) and field-emission scanning electron microscopy (FE-SEM). As shown in **Figure 7** (b), PtRu nanoparticles were uniformly dispersed on a graphene–Vulcan carbon composite and their ranges were primarily between 1 and 5 nm with an average particle size of 3.3 nm, which is slightly smaller than PtRu/Vulcan carbon with an average particle size of about 3.5 nm (**Figure 8**).

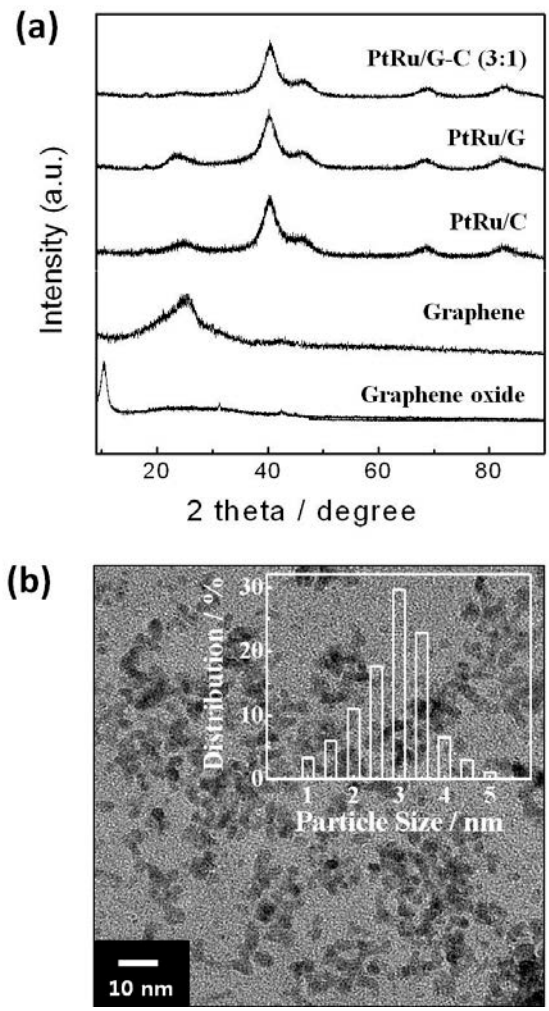

Figure 7. (a) X-ray diffraction profiles of graphene oxide, graphene, PtRu/Vulcan carbon (PtRu/C), PtRu/graphene (PtRu/G), and PtRu/graphene-Vulcan carbon (PtRu/G-C (3:1)) and (b) HR-TEM image of PtRu metal particles anchored onto graphene-Vulcan carbon. The inset is a graph of particle size distribution.

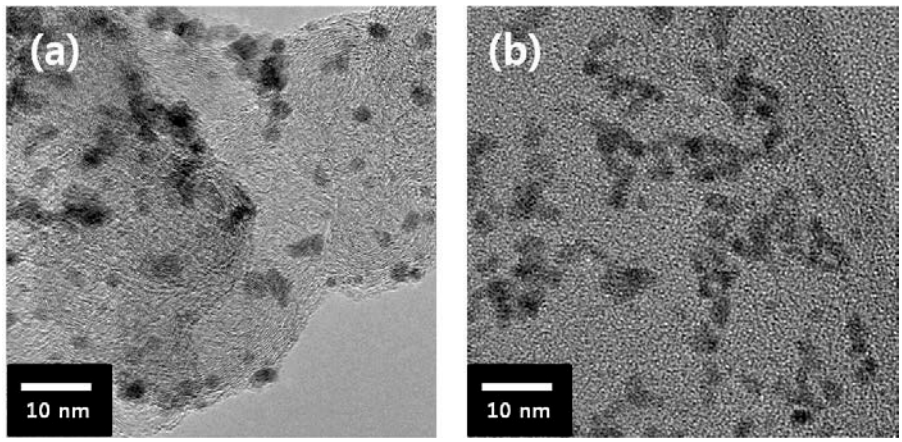

Figure 8. HR-TEM images of (a) PtRu/Vulcan carbon and (b) PtRu/graphene

The graphene consists of randomly aggregated, closely associated crumpled sheets forming a disordered solid. The PtRu/graphene catalyst (**Figure 9** (a)) shows a slightly wrinkled morphology, while the PtRu/graphene–Vulcan carbon composite shows a highly wrinkled morphology (**Figure 9** (b)). Aksay *et al.* reported that these wrinkles may be important for preventing the aggregation of graphene occurring from van der Waals forces during drying process and to maintain high active surface area [13, 24]. This means that the Vulcan carbon prevents the aggregation of graphene sheets and increases distance between them, thereby altering their arrays. An effective electrocatalyst is one that correctly balances the transport processes required for an operational fuel cell. A catalyst, ionomer and reactant are referred to as a triple-phase found in a catalyst layer. The triple-phases meet at the triple-phase boundary and create a reaction carried out by the catalyst particles [79]. In the PtRu/graphene, a relatively low triple-phase boundary resulted

from the aggregation of the graphene sheets. In contrast, more triple-phase boundaries could be created in a PtRu/graphene–Vulcan carbon than in a PtRu/graphene owing to the well-arranged spacing structure of a graphene–Vulcan carbon composite. Therefore, the catalyst layer with a graphene–Vulcan carbon composite provides more reactive PtRu nanoparticles adjacent with an ionomer and reactant, resulting in a higher methanol oxidation and ECA (**Figure 10** (b)). The electrocatalytic activity for methanol oxidation was estimated by linear sweep voltammetry. **Figure 10** (a) shows the linear sweep voltammograms of the PtRu/graphene–Vulcan carbon composite (PtRu/G–C), PtRu/graphene (PtRu/G), and PtRu/Vulcan carbon (PtRu/C) in 1 M CH_3OH and 1 M H_2SO_4. The current density of the PtRu/G–C catalyst was increased to twice that of the PtRu/G catalyst at 0.8 V. The electrocatalysts with different graphene–Vulcan carbon ratio were prepared and their electrochemical activities evaluated (**Figure 11**). PtRu/graphene–Vulcan carbon at 3:1 w/w shows the highest methanol oxidation compared to the other composition ratios. This ratio suggests the best electrocatalyst activity during methanol oxidation.

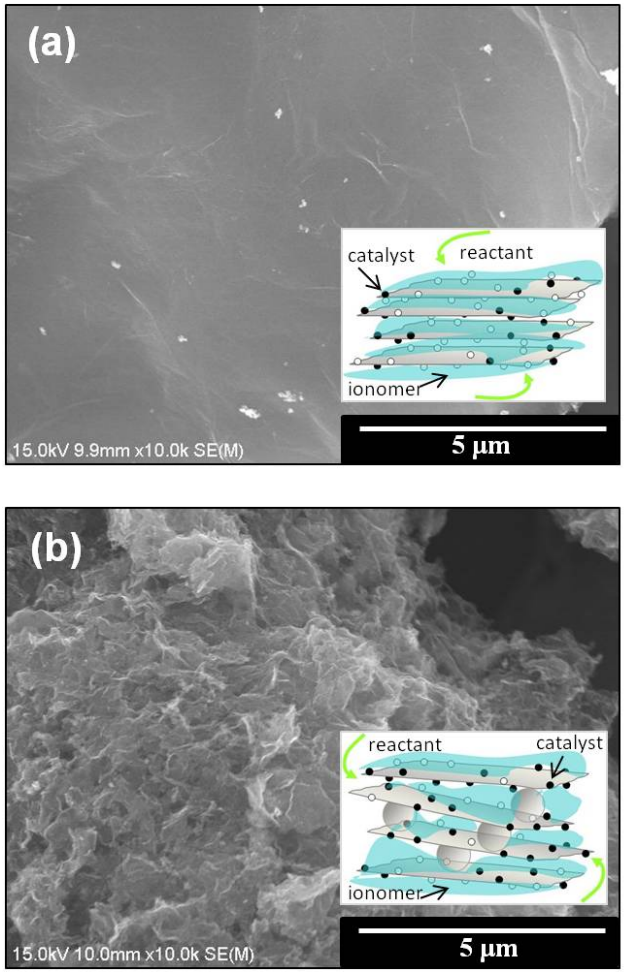

Figure 9. FE-SEM images of (a) PtRu/graphene and (b) PtRu/graphene-Vulcan carbon composite. The inserts show the effects of a spacing material between two-dimensional graphene (●: activated catalyst, ○: dead catalyst).

The electrochemically active surface area (ESA) provides important information regarding the number of available active sites. **Figure 10** (b) shows the CO-stripping voltammograms of the PtRu/graphene–Vulcan carbon (PtRu/G-C), PtRu/graphene (PtRu/G), and PtRu/Vulcan carbon (PtRu/C) recorded in 1 M H_2SO_4. Note that the PtRu/G-C catalyst of 79.8 $m^2 g^{-1}$ exhibits a larger electrochemical surface area than the PtRu/G catalyst value of 44.6 $m^2 g^{-1}$, which is attributed to the different active sites. Long-term methanol oxidation was conducted at 0.7 V and the variation of current with time was recorded (**Figure 10** (c)). The performances of the prepared catalysts show that the current density initially decreased and reached a steady state value. From these results, the PtRu/G-C catalyst exhibits a higher current density and long-term performance for the methanol oxidation compared with PtRu/G and PtRu/C. **Figure 12** shows the polarization curves of the polymer electrolyte membrane fuel cell using the as-prepared catalysts and the commercial catalysts. The current densities at 0.6 V are 0.967 A cm^{-2} and 0.368 A cm^{-2} for the 40 wt.% PtRu/G-C (3:1 w/w) and 40 wt.% PtRu/graphene, respectively. The power densities of the PtRu/G-C (3:1 w/w) and PtRu/graphene were found to be 0.742 W cm^{-2} and 0.310 W cm^{-2}, respectively. It is evident from **Figure 12** that the PtRu/G-C (3:1 w/w) catalyst exhibited better performance than that of the PtRu/graphene catalyst in a polymer electrolyte membrane fuel cell test. The results indicated that Vulcan carbon effectively modifies to array of graphene sheets, resulting in more triple-phase boundaries available for electrochemical reaction and better mass transport in the catalyst layer.

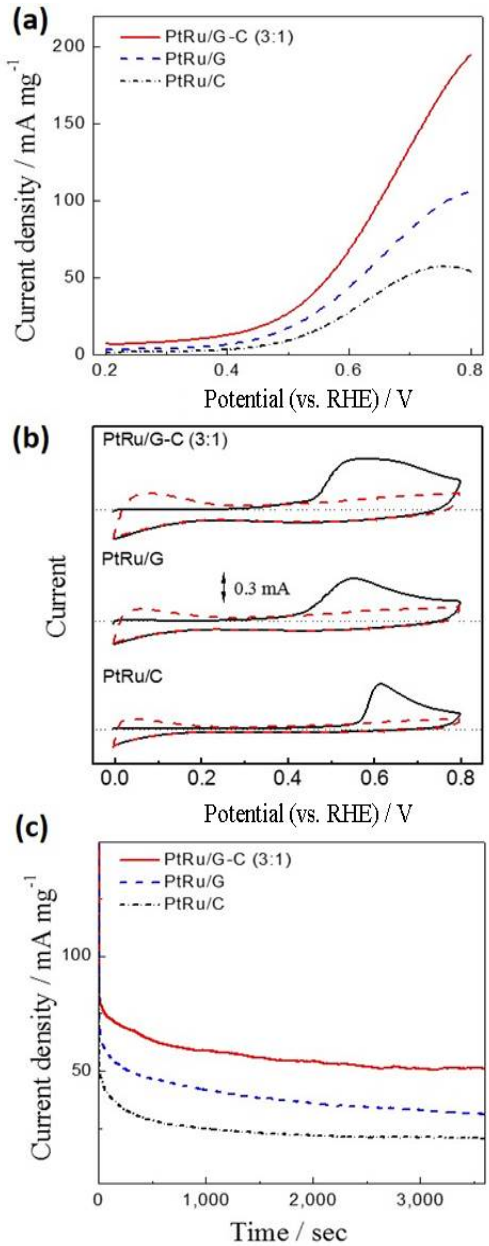

Figure 10. (a) Linear sweep voltammograms of the prepared catalysts in 1 M H_2SO_4 and 1 M CH_3OH at 25 °C at a scan rate of 20 mV s^{-1}. (b) CO-stripping voltammograms in 1 M H_2SO_4. The black line shows the first cycle, i.e., the CO stripping voltammograms, while the red dash line shows the second cycles, which are equivalent to the background CV of the particular catalysts. (c) Chronoamperometric curves at 0.7 V in 1 M CH_3OH and 1 M H_2SO_4.

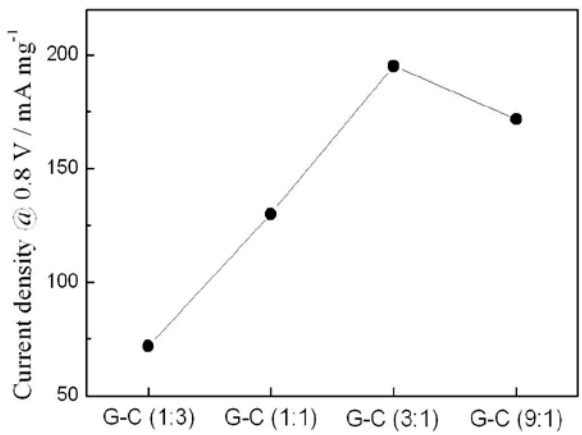

Figure 11. Methanol oxidation current at 0. 8 V for graphene-Vulcan carbon with different ratio (graphene to Vulcan carbon = 1:3, 1:1, 3:1, 9:1 w/w).

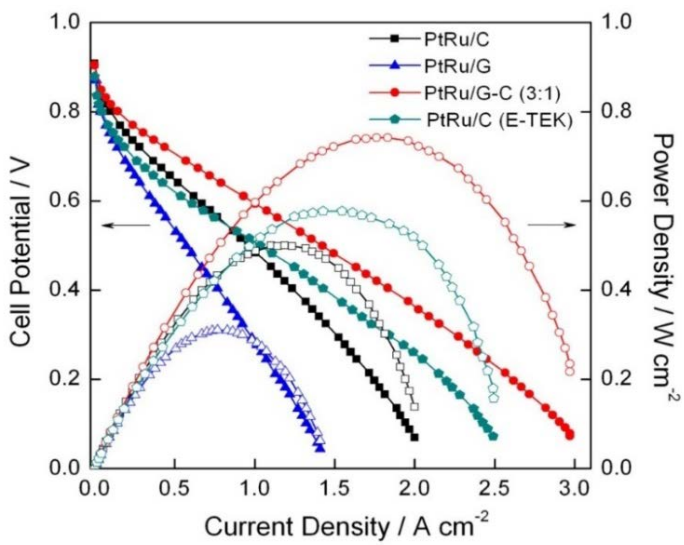

Figure 12. (a) Current–voltage polarization curves of the polymer electrolyte membrane fuel cell using PtRu/Vulcan carbon, PtRu/graphene, PtRu/Vulcan carbon-graphene (3:1), and commercial catalysts (E-TEK, 40 wt.% PtRu/C) as respective anode electrocatalyst. The cell temperature was maintained at 70^{o}C with the anode H_2 and cathode air gases.

4.2. Chemically activated graphene supported PtRu electrocatalyst

The PtRu/chemically activated graphene (PtRu/CAG) catalyst was prepared through a 2-step reaction: activation of graphene oxide, followed by an improved impregnation method of as-prepared chemically activated graphene and metal precursors. **Figure 13** (a) illustrates the preparation of graphene *via* the KOH activation process. During the activation reaction at elevated temperature, the surface of graphene acquires a high porosity and large specific surface area. In the reaction, KOH is reduced into metallic K and carbon atoms of graphene are oxidized to carbon oxide and carbonate. The as-formed metallic K intercalate into the graphene layers and accelerates the efficient activation process all over the graphene surface, leading to higher structural porosity [80].

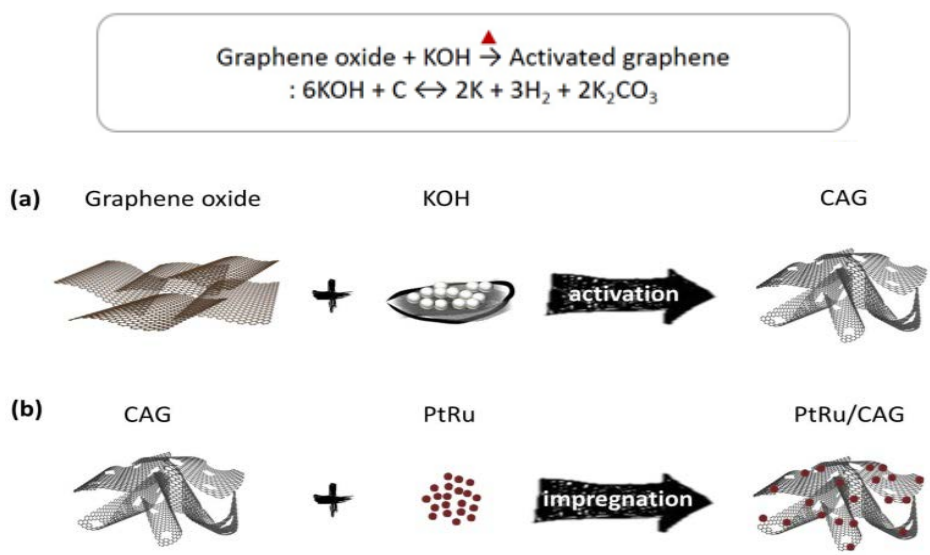

Figure 13. Schematic diagrams of (a) chemically activated graphene (CAG) by KOH activation and (b) PtRu/ chemically activated graphene (PtRu/CAG) using an improved impregnation method.

The KOH activation process generates a porous structrure of various pore sizes. FE-SEM and HR-TEM images show the surface morphology of chemically activated graphene.

The FE-SEM images (**Figure 14**) reveal the three-dimensional structure of chemically activated graphene (CAG), consisting of pores and rough edges. In contrast, the graphene consists of a thinm wrinkled paper-like structures. Similarly, the PtRu/graphene (PtRu/G) shows a slightly wrinkled structure, while the structure of PtRu/chemically activated graphene (PtRu/CAG) displays abundant wrinkles. The wrinkles in graphene have practical significance in that they prevent the aggregation of the graphene sheets and thus maintain a large active surface area.

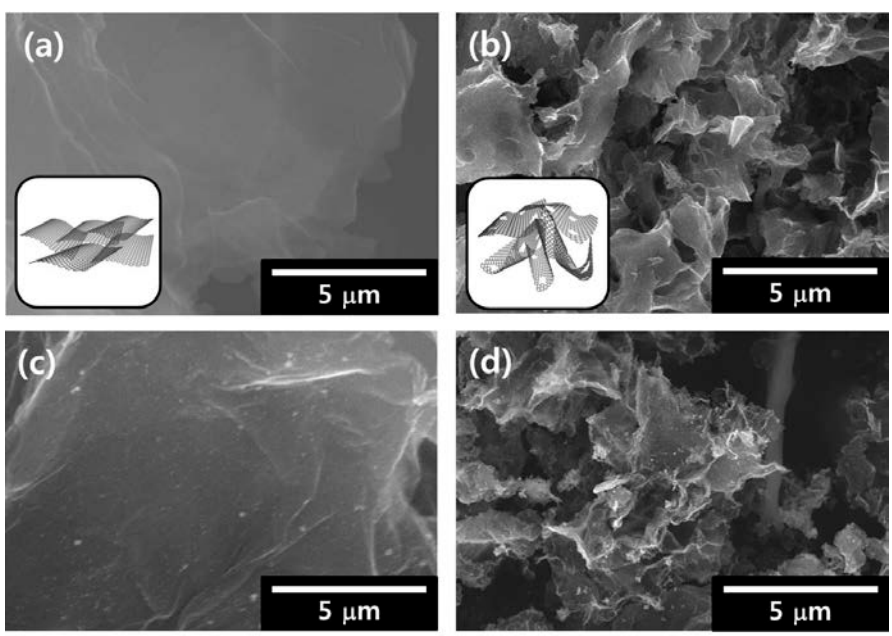

Figure 14. FE-SEM images of (a) graphene sheets, (b) chemically activated graphene (CAG), (c) PtRu/graphene(PtRu/G), and (d) PtRu/chemically activated graphene (PtRu/CAG).

In particular, the HR-TEM image reveals a nanoporous structure, similar to that of porous graphene activated by KOH reported previously [70], indicating that this activation process is able to etch the graphene sheets to form a porous structure. Chemically activated graphene had a rough and mesh-like structure (**Figure 15** (b)), whereas graphene typically shows a flat and smooth surface (**Figure 15** (a)). The images indicate that KOH etched the structure during the activation process.

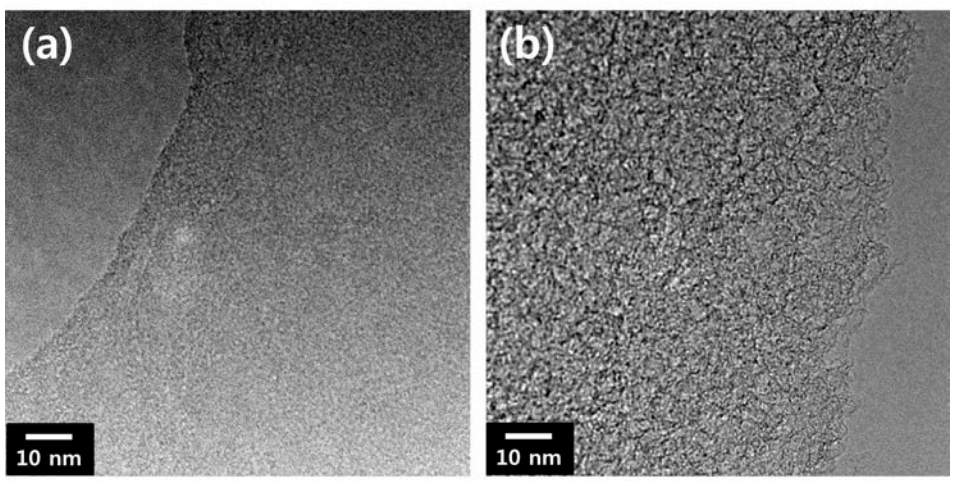

Figure 15. HR-TEM images of (a) graphene and (b) chemically activated graphene.

The HR-TEM image of PtRu/chemically activated graphene (**Figure 16**) shows the PtRu nanoparticles tobe uniformly dispersed on the chemically activated graphene with an average particle size of about 3.1 nm, which is slightly smaller than PtRu/graphene with an average particle size of about 3.3 nm. The presence of PtRu (1:1 atomic ratio) in PtRu/chemically activated graphene was confirmed by the EDX spectrum.

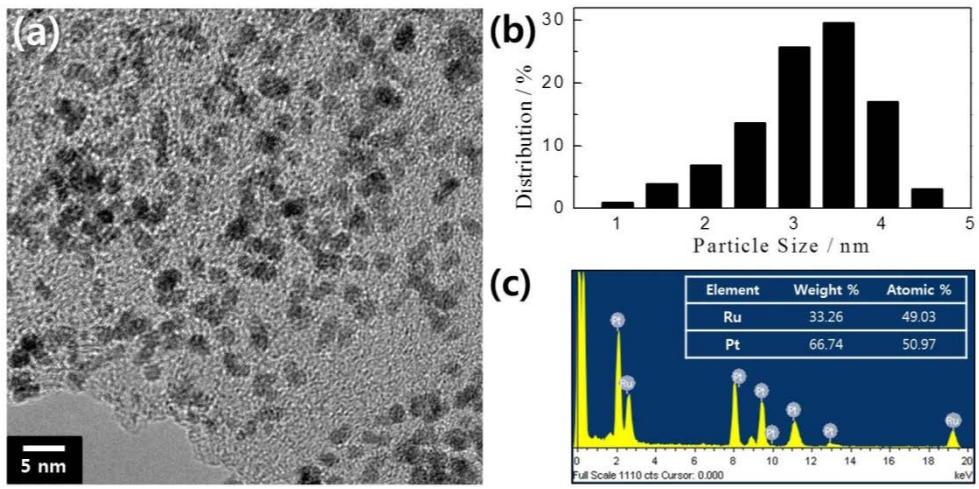

Figure 16. (a) HR-TEM image of PtRu metal particles anchored on chemically activated graphene. (b) Particle size distribution and (c) EDX spectrum of PtRu/chemically activated graphene.

Table 2 shows the specific surface area, total pore volume, and average pore sizes of the samples. The specific surface areas of graphene and chemically activated graphene were 370 and 2,376 m^2 g^{-1} respectively. The very large surface area of chemically activated graphene was close to the theoretical value of graphene (2,630 m^2 g^{-1}). This is because the in-plane pores created during the chemical activation process, increase the surface area of chemically activated graphene.

In the nitrogen adsorption/desorption analysis, the isotherm slope of chemically activated graphene continuously increased until around P/P_0 = 0.5. According to the classification of isotherms, the chemically activated graphene isotherm could be classified as a mesopore type (**Figure 17**), chemically activated graphene exhibited a narrow pore diameter distribution mainly centered at ~ 3.8 nm.

Graphene has a surface are of 360 m^2 g^{-1} with average pore diameter of ~ 4.3 nm. The nitrogen adsorption/desorption isotherm of graphene shows a platelet-like structure [81, 82]. Active sites are often located in mesopore of 2 ~ 10 nm, whereas the mesopores of 20 ~ 50 nm and macropore favor mass transfer and reduce transport limitations [83]. Therefore, the existence of pores of various sizes in the chemically activated graphene expected to be beneficial for the mass transfer of the reactant.

Table 2. Specific surface area, total pore volume, and average pore diameter of Vulcan carbon (C), graphene (G), and chemically activated graphene (CAG). The specific surface area and total pore volume were calculated using the BET method and the average pore diameter was yielded by the BJH method.

	C	**G**	**CAG**
Specific surface area (m^2/g)	240	366	2,376
Total pore volume (m^3/g) [a]	0.62	0.99	1.86
Average pore diameter (nm) [b]	10.43	10.67	2.89

[a] Total pore volumes measured at P/Po = 0.995.
[b] BJH desorption average pore diameters.

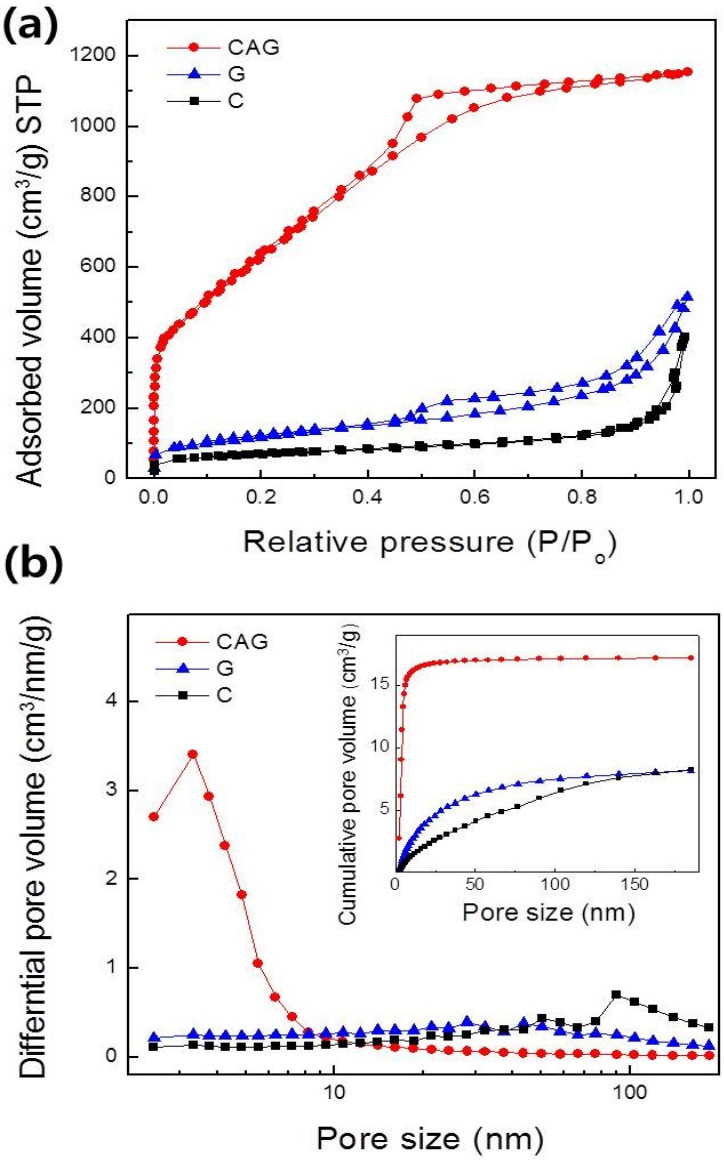

Figure 17. Nitrogen adsorption/desorption analysis of chemically activated graphene (CAG), graphene (G) and Vulcan XC-72 (C). (a) N_2 isotherm curves at 77.4 K. (b) Cumulative pore volume and pore diameter distribution obtained from the adsorption isotherm in (a).

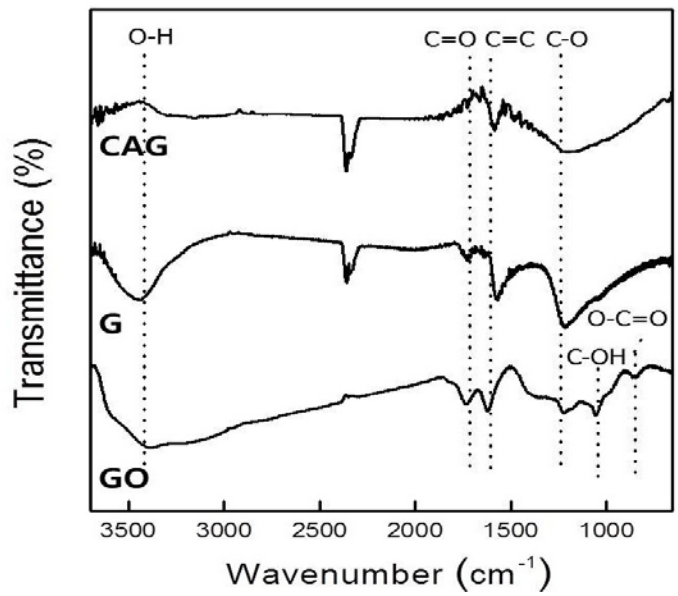

Figure 18. FT-IR spectra of graphene oxide (GO), graphene (G), and chemically activated graphene (CAG).

The reduction of graphene oxide, was assessed by recording the Fourier transform infrared (FT-IR) and X-ray photoelectron spectroscopy (XPS) spectra of graphene oxide, graphene, and chemically activated graphene (**Figure 18, 19)**

The FT-IR spectrum of graphene oxide shows the presence of various oxygen-containing groups, including O-C=O, C-OH, C-O, and C=O, which are formed owing to the strong oxidation process [77]. On the other hand, in the case of graphene and chemically activated graphene, most of the contributions from the oxygen-containing groups decrease after heat treatment.

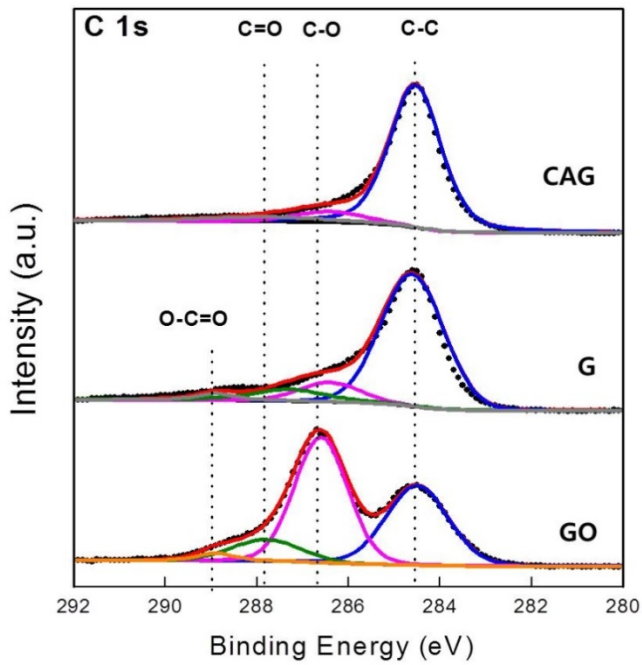

Figure 19. XPS spectra of graphene oxide (GO), graphene (G), and chemically activated graphene (CAG).

The C 1s XPS spectra can be deconvoluted into four peaks at binding energies of ~ 284.6, ~ 286.6, ~ 287.9, and ~ 289 eV, which can be attributed to the sp^2 C-C, C-O, C=O, and O-C=O groups, respectively [74, 75]. The peak resulting from the C-O bond of chemically activated graphene and graphene is much smaller than that of graphene oxide. On the other hand, the peak of the C-C bond of chemically activated graphene and graphene at a binding energy of 284.6 eV is larger than that of graphene oxide. The area percentages of the different peaks are summarized in **Table 3**, which shows that the ratio of bonds between carbon and oxygen in chemically activated graphene is much smaller than that in graphene oxide and

graphene. This evidence indicates that graphene oxide was reduced during the activation process.

Table 3. Relative intensities of C 1s bond of graphene oxide (GO), graphene (G), and chemically activated graphene (CAG) by XPS measurement.

Bond	GO (%)	G (%)	CAG (%)
C-C	37.2	72.7	85.3
C-O	49.7	14.1	9.5
C=O	10.6	11.1	5.2
O-C=O	2.5	2.1	-

Figure 20 shows the XRD patterns of the catalyst supports and the catalysts. The XRD pattern of graphene oxide showed a well-defined (002) peak at 11.8° corresponding to a d-spacing (interlayer distance between sheets) value of 0.837 nm. This value is higher than the interlayer spacing of graphite flackes (d-spacing: 0.335 nm), because of the presence of oxygenated functional groups and intercalated water molecules [84]. After thermal reduction, the graphene exhibited a weak and broad diffraction peak at 23.9°, whereas the peak displayed by graphene oxide at 11.8° was absent from the XRD pattern of graphene. After thermal reduction of the graphene oxide to graphene [75, 76]. The d-spacing value decreased to 0.344 nm. The distance between the graphene layers of chemically activated graphene was found to be 0.349 nm, which is somewhat larger than that

of graphene. Additionally, the XRD data of PtRu catalysts loaded onto supporting materials are shown in **Figure 20**. The Pt peak representing the (111) plane observed for all alloy catalysts is shifted toward a slightly higher value compared with pure Pt. This shift indicates the formation of an alloy between Pt and Ru [72].

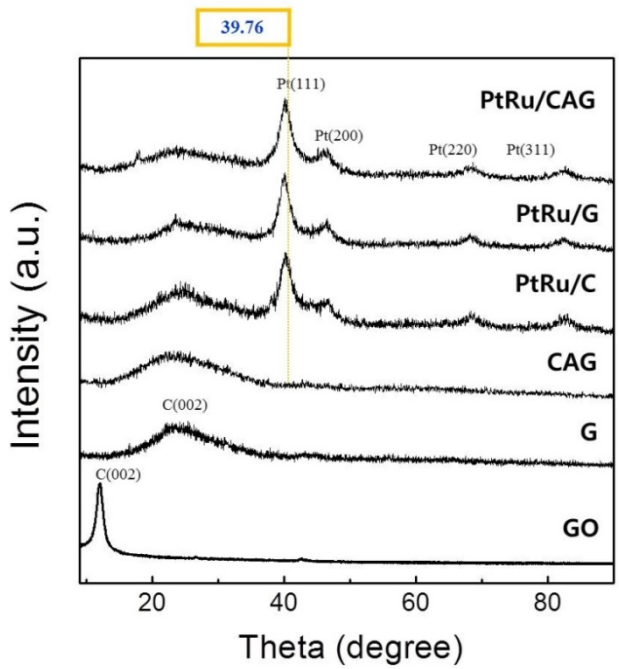

Figure 20. X-ray diffraction patterns of graphene oxide (GO), graphene (G), chemically activated graphene (CAG), PtRu/Vulcan carbon (PtRu/C), PtRu/graphene (PtRu/G), and PtRu/chemically activated graphene (PtRu/CAG).

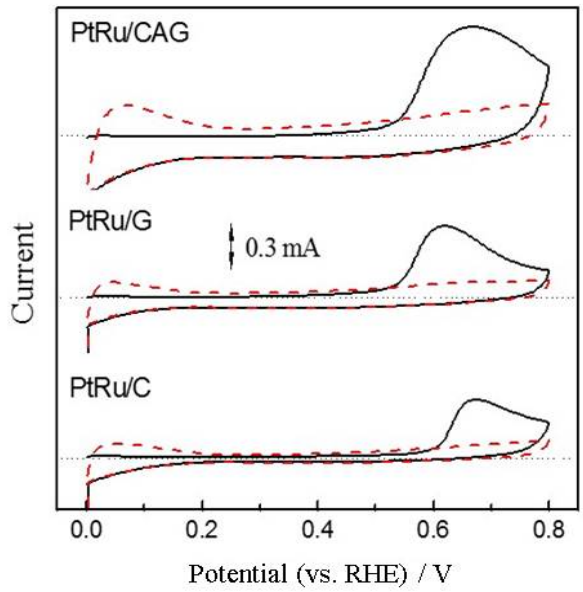

Figure 21. CO-stripping voltammograms of PtRu/chemically activated graphene (PtRu/CAG), PtRu/graphene (PtRu/G), and PtRu/Vulcan carbon (PtRu/C) in 1 M H_2SO_4. The black line shows the first cycle, *i.e.*, the CO stripping voltammograms, while the red dash line shows the second cycles, which are equivalent to the background CV of the particular catalysts.

The electrochemically active surface area (ECA) provides important information regarding the number of available active sites. **Figure 21** shows the CO-stripping voltammograms of the PtRu/activated graphene (PtRu/AG), PtRu/graphene (PtRu/G) and PtRu/Vulcan carbon (PtRu/C) recorded in 1 M H_2SO_4 at a scan rate of 20 mV s^{-1}. The utilization of the PtRu/CAG catalyst showed a significantly higher electrochemically active surface area of 80.2 m^2 g^{-1} in methanol electro-oxidation compared to that shown by the PtRu/G (44.8 m^2 g^{-1}) and PtRu/C (26.5 m^2 g^{-1}) catalysts. This meas that the abundant pores and three-dimensional

structure in the support material played an important role in the electrochemical reaction.

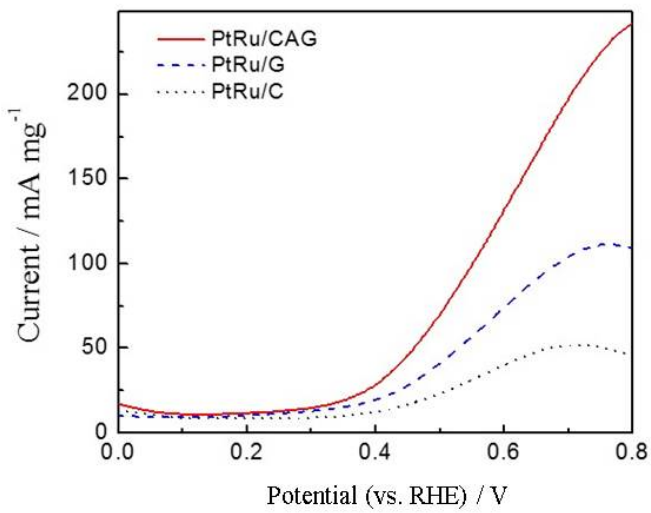

Figure 22. Linear sweep voltammograms ofPtRu/chemically activated graphene (PtRu/CAG), PtRu/graphene (PtRu/G), and PtRu/Vulcan carbon (PtRu/C) in 1 M H_2SO_4 and 1 M CH_3OH at 25°C at a scan rate of 20 mV s^{-1}.

Figure 22 shows the linear sweep voltammograms of the PtRu/CAG, PtRu/G, and PtRu/C in 1 M CH_3OH and 1 M H_2SO_4. The current density of the PtRu/CAG catalyst is more than twice as high as that of the PtRu/G catalyst at 0.7 V. The results indicated that the chemical activation of graphene to produce CAG effectively modifies the graphene sheets, resulting in the availability of additional triple-phase boundaries for electrochemical reation. The enhanced current of the methanol oxidation indicated that a higher energy density could be achieved in fuel cells for practical applications.

The long-term stabilities of the catalysts prepared for methanol oxidation were

investigated by recording their chronoamperometric curves in 1 M H_2SO_4 and 1 M CH_3OH at a constant potential of 0.6 V (**Figure 23**). For all the catalysts, the current was initially observed to decrease, which could be ascribed to the formation of CO_{ads} and other intermediate species during the methanol oxidation reaction [85, 86] However, the urrent of the PtRu/CAG catalyst is still considerably higher than those obtained for the PtRu/G and PtRu/C catalysts after 2000 s. These results indicate that the chemically activated graphene would be capable of providing effective support for a metal catalyst in fuel cells.

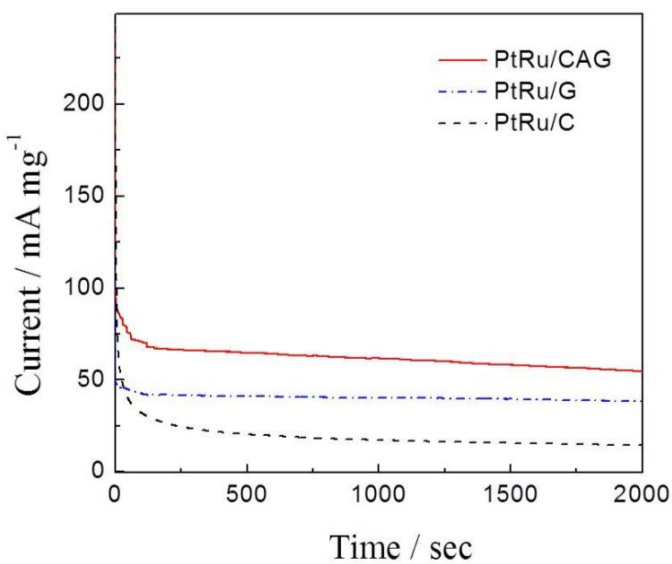

Figure 23. Chronoamperometric response of PtRu/chemically activated graphene (PtRu/CAG), PtRu/graphene (PtRu/graphene), and PtRu/Vulcan carbon (PtRu/C) in 1 M H_2SO_4 and 1 M CH_3OH at 0.6 V.

5. CONCLUSION AND PERSPECTIVE

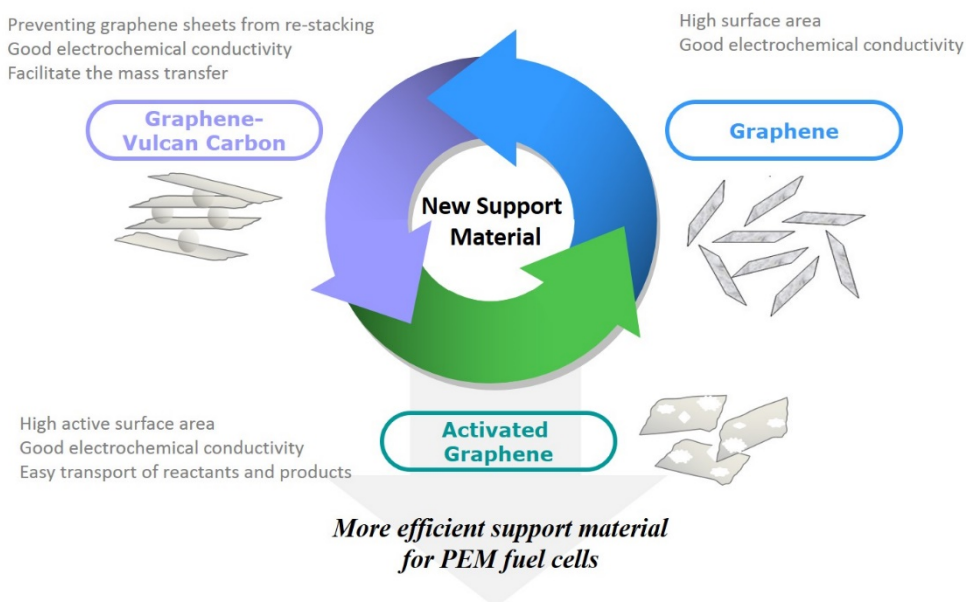

In this part, we studied a new support material for low temperature fuel cell electrocatalyst: graphene, graphene-Vulcan carbon composite and chemically activated graphene. We tried to provide a better approach of reactants into PtRu catalysts *via* the addition of a nano-sized spacer between graphene sheets. Vulcan carbon is added as a nano spacer to enhance the utilization and electrochemical activities of the graphene-based materials. The results show that a PtRu catalyst loaded onto the graphene-Vulcan carbon (3:1 w/w) composite exhibits high electrocatalytic activity and high stability toward methanol electrochemical oxidation owing to the special structure of the graphene-Vulcan carbon composite.

Also, the PtRu/graphene-Vulcan carbon catalyst exhibits better performance than the PtRu/graphene catalyst in a polymer electrolyte membrane fuel cell test. Also, we prepared a chemically activated graphene by using KOH activation, after which it was loaded with 40 wt.% PtRu using an improved impregnation method. The chemical activation of graphene to produce CAG results in a modification that leads to an increase in the number of triple-phase boundaries that are available for electrochemical reaction. The results show that the PtRu/CAG exhibited an enhanced electrocatalytic activity and stability toward methanol oxidation owing to the three-diemnsional and porous structure of the CAG. The outstanding catalytic activity of the PtRu/CAG catalyst suggests that the chemically activated graphene can be used as the catalyst support in fuel cells.

6. REFERENCES

[1] K.I. Han, J.S. Lee, S.O. Park, S.W. Lee, Y.W. Park, H. Kim, *Electrochim. Acta*, 50 (2000) 791.

[2] K. Park, Y. Sung, S. Han, Y. Yun, T. Hyeon, *J. Phys. Chem. B,* 108 (2004) 939.

[3] E. Antolini, *Appl. Catal. B,* 88 (2009) 1.

[4] A.S. Arico, L. Pino, P.L. Antonucci, N. Giordano, *Carbon*, 28 (1990) 599.

[5] P.A. Simonov, V.A. Likholobov, in: A. Wieckowski, E.R. Savinova, C.G. Vayenas (Eds.), Catalysis and Electrocatalysis at Nanoparticle Surfaces, Marcel Dekker, New York, 2003, p. 409.

[6] Y. Takasu, T. Kawaguchi, W. Sugimoto, Y. Murakami, *Electrochim. Acta,* 48 (2003) 3861.

[7] C.A. Bessel, K. Laubernds, N.M. Rodriguez, R.T.K. Baker, *J. Phys. Chem. B*, 105 (2001) 1115.

[8] K.W. Park, Y.E. Sung, S. Han, Y. Yun, T. Hyeon, *J. Phys. Chem. B,* 108 (2004) 939.

[9] I.-S. Park, K.-W. Park, J.-H. Choi, C.R. Park, Y.-E. Sung, *Carbon*, 45 (2007) 28.

[10] K.S. Novoselov, A.K. Geim, S.V. Morozov, D. Jiang, Y. Zhang, S.V. Dubonos, I.V. Grigorieva, A.A. Firsov, *Science*, 306 (2004) 666.

[11] A.K. Geim, K.S. Novoselov, *Nature Mater.*, 6 (2007) 183.

[12] B. Seger, P.V. Kamat, *J. Phys. Chem. C,* 113 (2009) 7990.

[13] R. Kou, Y. Shao, D. Wang, M.H. Engelhard, J.H. Kwak, J. Wang, V.V.

Viswana-than, C. Wang, Y. Lin, Y. Wang, I.A. Aksay, J. Liu, *Electrochem. Commun.,* 11 (2009) 954.

[14] Y. Xin, J. Liu, Y. Zhou, W. Liu, J. Gao, Y. Xie, Y. Yin, Z. Zou, *J. Power Sources,* 196 (2011) 1012.

[15] D.A.C. Brownson, D.K. Kampouris, C.E. Banks, *J. Power Sources,* 196 (2011) 110.

[16] S. Bong, Y. Kim, I. Kim, S. Woo, S. Uhm, J. Lee, H. Kim, *Electrochem. Commun.,* 12 (2010) 129.

[17] Q. Shi, S. Mu, *J. Power Sources,* 203 (2012) 48.

[18] H. Huang, H. Chen, D. Sun, X. Wang, *J. Power Sources,* 204 (2012) 46.

[19] M.S. Wietecha, J. Zhu, G. Gao, N. Wang, H. Feng, M.L. Gorring, M.L. Kasner, S. Hou, *J. Power Sources,* 198 (2012) 30.

[20] S. Park, R.S. Ruoff, *Nature Nanotech.,* 4 (2009) 217.

[21] W. Yang, K.R. Ratinac, S.P. Ringer, P. Thordarson, J.J. Gooding, F. Braet, *Angew. Chem. Int. Ed.,* 49 (2010) 2114.

[22] D. Li, M.B. Muller, S. Gilje, R.B. Kaner, G.G. Wallace, *Nat. Nanotechnol.,* 3 (2008) 101.

[23] H.C. Schniepp, J. Li, M. J. McAllister, H. Sai, M. Herrera-Alonso, D.H. Adamson, R.K. Prud'homme, R. Car, D.A. Saville, I.A. Akasy, *J. Phys. Chem. B,* 110 (2006) 8535.

[24] M. J. McAllister, J. Li, D.H. Adamson, H.C. Schniepp, A.A. Abdala, J. Liu, M. Herrera-Alonso, D.L. Milius, R. Car, R.K. Prud'homme, I.A. Aksay, *Chem. Mater.*, 19 (2007) 4396.

[25] S. Iijima, *Nature*, 354 (1991) 56.

[26] T.W. Ebbesen, P.M. Ajayan, *Nature*, 358 (1992) 220.

[27] V.A. Paganin, E.A. Ticianelli, E.R. Gonzalez, *J. Appl. Electrochem.*, 26 (1996) 297.

[28] J. Chen, M. Wang, B. Liu, Z. Fan, K. Cui, Y. Kuang, *J. Phys. Chem. B*, 110 (2006) 11775.

[29] T.W. Ebbesen, H. Hiura, M.E. Bisher, M.M.J. Treacy, J.L. ShreeveKeyer, R.C. Haushalter, *Adv. Mater. 8*, (1996) 155.

[30] V. Lordi, N. Yao, J. Wei, *Chem. Mater.*, 13 (2001) 733.

[31] J.M. Planeix, N. Coustel, B. Coq, V. Brotons, P.S. Kumbhar, R. Dutartre, P. Geneste, P. Bernier, P.M. Ajayan, *J. Am. Chem. Soc.*, 116 (1994) 7935.

[32] Z.L. Liu, X.H. Lin, J.Y. Lee, W. Zhang, M. Han, L.M. Gan, *Langmuir*, 18 (2002) 4054.

[33] H.F. Yang, Y. Yan, Y. Liu, F.Q. Zhang, R.Y. Zhang, Y. Meng, M. Li, S.H. Xie, B. Tu, D.Y. Zhao, *J. Phys. Chem. B*, 108 (2004) 17320.

[34] G.L. Che, B.B. Lakshmi, C.R. Martin, E.R. Fisher, *Langmuir*, 15 (1999) 750.

[35] C.-T. Hsieh, Y.-T. Lin, *Micropor. Mesopor. Mater.*, 93 (2006) 232.

[36] W.Z. Li, C.H. Liang, J.S. Qiu, W.J. Zhou, H.M. Han, Z.B. Wei, G.Q. Sun, Q. Xin, *Carbon*, 40 (2002) 791.

[37] N. Rajalakshmi, H. Ryu, M.M. Shaijumon, S. Ramaprabhu, *J. Power Sources*, 140 (2005) 250.

[38] B. Rajesh, K. Ravindranathan Thampi, J.M. Bonard, N. Xanthopoulos, H.J. Mathieu, B. Viswanathan, *J. Phys. Chem. B*, 107 (2003) 2701.

[39] P. Serp, M. Corrias, P. Kalck, *Appl. Catal. A*, 253 (2003) 337.

[40] T.W. Kim, I.S. Park, R. Ryoo, *Angew. Chem.*, 42 (2003) 4375.

[41] J.M. Gatica, J.M. Rodriguez-Izquierdo, D. Sanchez, C. Ania, J.B. Parra, H. Vidal, *Carbon*, 42 (2004) 3251.

[42] E.S. Steigerwalt, G.A. Deluga, C.M. Lukehart, *J. Phys. Chem. B*, 106 (2002) 760.

[43] X.K. Lu, M.F. Yu, H. Huang, T.S. Ruoff, *Nanotechnol.*, 10 (1999) 269.

[44] K.S. Novoselov, A.K. Geim, S.V. Morozov, D. Jiang, Y. Zhang, S.V. Dubonos, I.V. Grigorieva, A.A. Firsov, *Science*, 306 (2004), 666.

[45] G. Eda, G. Fanchini, M. *Nat. Nanotechnol.*, 3 (2008) 270

[46] M.J. McAllister, J.L. Li, D.H. Adamson, H.C. Schniepp, A.A. Abdala, J. Liu, M. Herrera-Alonso, D.L. Milius, R. Car, R.K. Prud′homme, I.A. Aksay, *Chem. Mater.*, 19 (2007) 4396

[47] G. Wang, J. Yang, J. Park, X. Gou, B. Wang, H. Liu, J. Yao, *J. Phys. Chem. C*, 112 (2008) 8192.

[48] A. Du, Z. Zhu, S.C. Smith, *J. Am. Chem. Soc.*, 132 (2010) 2876.

[49] X. Zhao, C.M. Hayner, M.C. Kung, H.H. Kung, *ACS Nano*, 5 (2011) 8739.

[50] M.D. Stoller, S. Murali, N. Quarles, Y. Zhu, J.R. Potts, X. Zhu, H.-W. Ha, R.S. Ruoff, *Phys. Chem. Chem. Phys.*, 14 (2012) 3388.

[51] S. Murali, J.R. Potts, S. Stoller, J. Rark, M.D. Stoller, L.L. Zhang, Y. Zhu, R.S. Ruoff, *Carbon*, 50 (2012) 3482.

[52] S. Blankenburg, M. Bieri, R. Fasel, K. Müllen, C.A. Pignedoli, D. Passerone, *Small*, 6 (2010) 2266.

[53] D. Jiang, V.R. Cooper, S. Dai, *Nano Lett.*, 9 (2009) 4019.

[54] S. Stankovich, D.A. Dikin, G.H.B. Dommett, K.M. Kohlhaas, E.J. Zimney, E.A. Stach, R.D. Piner, S.T. Nguyen, R.S. Ruoff, *Nature*, 442 (2006) 282.

[55] R.B. Rakhi, H.N. Alshareef, *J. Power Sources*, 196 (2011) 8858.

[56] R.B. Rakhi, W. Chen, D. Cha, H.N. Alshareef, *Adv. Energy Mater.*, 2 (2012) 381.

[57] S. Chen, J. Duan, Y. Tang, S. Z. Qiao, *Chem. Eur. J.*, 19 (2013) 7118.

[58] S. Chen, J. Duan, M. Jaroniec, S. Z. Qiao, *J. Mater. Chem. A*, 1 (2013) 9409.

[59] J. Yan, T. Wei, B. Shao, Z. Fan, W. Qian, M. Zhang, F. Wei, *Carbon*, 48 (2010) 487.

[60] X.-C. Chen, W. Wei, W. Lv, F.-Y. Su, Y.-B. He, B. Li, F. Kang, Q.-H. Yang, *Chem. Commun.*, 48 (2012) 5904.

[61] J. Yan, T. Wei, Z. Fan, W. Qian, M. Zhang, X. Shen, F. Wei, *J. Power Sources*, 195 (2010) 3041.

[62] D. Yu, L. Dai, *J. Phys. Chem. Lett.*, 1 (2009) 467.

[63] Z. Fan, J. Yan, L. Zhi, Q. Zhang, T. Wei, J. Feng, M. Zhang, W. Qian, F. Wei,

Adv. Mater., 22 (2010) 3723.

[64] M.-Q. Zhao, X.-F. Liu, Q. Zhang, G.-L. Tian, J.-Q. Huang, W. Zhu, F. Wei, *ACS Nano*, 6 (2012) 10759.

[65] J.J. Shao, W. Lv, Q. Guo, C. Zhang, Q. Xu, Q. H. Yang, F. Kang, *Chem. Commun.*, 48 (2012) 3706.

[66] M.-Q. Zhao, Q. Zhang, J.-Q. Huang, G.-L. Tian, T.-C. Chen, W.-Z. Qian, F. Wei, *Carbon*, 54 (2013) 403.

[67] N.I. Kovtyukhova, P.J. Ollivier, B.R. Martin, T.E. Mallouk, S.A. Chizhik, E.V. Buzaneva, A.D. Gorchinskiy, *Chem. Mater.*, 11 (1999) 771.

[68] A.J. Patil, J.L. Vickery, T.B. Scott, S. Mann, *Adv. Mater.*, 21 (2009) 3159.

[69] Y. Kim, S. Bong, Y. Kang, Y. Yang, R.K. Mahajan, J.S. Kim, H. Kim, *Biosens. Bioelectron*, 25 (2010) 2366.

[70] Y. Zhu, S. Murali, M. D. Stoller, K. J. Ganesh, W. Cai, P.J. Ferreira, A. Pirkle, R.M. Wallace, K.A. Cychosz, M. Thommes, D. Su, E.A. Stach, R.S. Ruoff, *Science*, 332 (2011) 1537.

[71] L.L. Zhang, X. Zhao, M.D. Stoller, Y. Zhu, H. Ji, S. Murali, Y. Wu, S. Perales, B. Clevenger, R.S. Ruoff, *Nano Lett.*, 12 (2012) 1806.

[72] I. Kim, S. Bong, S. Woo, R.K. Mahajan, H. Kim, *Int. J. Hydrogen Energy*, 36 (2011) 1803.

[73] Y. Takasu, T. Fujiwara, Y. Murakami, K. Sasaki, M. Oguri, T. Asaki, W. Sugimoto, *J. Electrochem. Soc.*, 147 (2000) 4421.

[74] X. Fan, W. Peng, Y. Li, X. Li, S. Wang, G. Zhang, F. Zhang, *Adv. Mater.*, 20

(2008) 4490.

[75] J. Yan, T. Wei, B. Shao, F. Ma, Z. Fan, M. Zhang, C. Zheng, Y. Shang, W. Qian, F. Wei, *Carbon*, 48 (2010) 1731.

[76] S. Park, S. Yu, N. Pinna, S. Woo, B. Jang, Y. Chung, Y. Cho, Y. Sung, Y. Piao, *J. Mater. Chem.*, 22 (2012) 2520.

[77] R. Bissessur, P.K.Y. Liu, W. White, S.F. Scully, *Langmuir*, 22 (2006) 1729.

[78] J. Guo, G. Sun, Q. Wang, G. Wang, Z. Zhou, S. Tang, L. Jiang, B. Zhou, Q. Xin, *Carbon*, 44 (2006) 152.

[79] S. Litster, G. McLean, *J. Power Sources*, 130 (2004) 61.

[80] J. Wang, S. Kaskel, *J. Mater. Chem.*, 22 (2012) 23710.

[81] K.S.W. Sing, D.H. Everett, R.A.W. Haul, L. Moscou, R.A. Pierotti, J. Rouquerol, T. Siemieniewska, *Pure & Appl. Chem.*, 57 (1985) 603.

[82] D. He, K. Cheng, T. Peng, M. Pan, S. Mu, *J. Mater. Chem. A*, 1 (2013) 2126.

[83] K. Kaneko, *J. Membrane Sci.*, 96 (1994) 59.

[84] X. Mei, J. Ouyang, *Carbon*, 49 (2011) 5389.

[85] Y. Hu, H. Zhang, P. Wu, H.Zhang, B.Zhou, and C. Cai, *Phys. Chem. Chem. Phys.*, 13 (2011) 4083.

[86] Y. Xu, X. Lin, *J. Power Sources*, 170 (2007) 13.

PART 3

ONE-STEP SYNTHESIS OF Pt-GRAPHENE CATALYST

1. INTRODUCTION

Graphene-metal nanoparticle catalysts have typically been prepared by chemical or thermal reduction of mixtures of GO (or graphene) and metallic precursors. These methods involve hazardous chemicals, or high temperatures and complicated procedures. More recently, the electrochemical reduction of GO by potentiostatic method such as chronoamperometry or cyclic voltammetry has been developed [1-12]. For instance, Liu and co-workers [13] developed electrodeposition method for the synthesis of graphene-Au (Au NPs with a diameter of about 30 nm) nanocomposite film through cyclic voltammetry. Ye and co-workers [14] investigated by pulsed potential deposition and chronoamperometry for the synthesis of graphene-Pt (Pt microspherical particles are built up by numerous small Pt nanorods with average diameter of ~ 30 nm and the length of ~ 90nm). The electrodeposition technique is attractive because it is fast, clean, and simple. In general, electrodeposition can be carried out using either a potentiostatic or galvanostatic method, which involve direct and pulse techniques. The galvanostatic method is more convenient for the preparation of high geometric surface area electrodes, because the electrical set-up requires only two electrodes and an arbitrary waveform generator, whereas the potentiostatic set-up requires a three electrode configuration. Electrodeposition via the galvanostatic pulse technique is better for controlling particle size and composition of the alloy by

varying experimental parameters such as duty cycle (on/off time), peak current density, and total charge [3, 4].

One step co-electrodeposition synthesis of the Pt/graphene catalyst is possible because both GO and H_2PtCl_6 reduction reactions can occur under cathodic conditions simultaneously. Herein, we demonstrate the one step co-electrodeposition synthesis of the Pt/graphene catalyst using a galvanostatic pulse technique. The novel Pt/graphene electrocatalyst exhibits significantly higher electrocatalytic activity than commercially available Pt/C catalysts toward methanol oxidation.

2. EXPERTIMENTAL

2. 1. Preparation of graphene and Pt/graphene electrocatalyst

Pulsed galvanostatic electrodeposition of the Pt/graphene catalyst was carried out in a two-electrode cell using an Autolab electrochemical workstation (Metrohm, USA). **Figure 1** shows a schematic of the pulsed electrodeposition method. The glassy carbon electrode (GCE, 3 mm diameter, Bioanalytical Systems, Inc.) served as a working electrode and a Pt wire as the counter electrode. The working electrodes were prepared as follows: the GCE, polished to a mirror finish with a 0.05 mm alumina suspension (Buehler, Lake Bluff, MN, USA) before electrodeposition, was used as a substrate for the catalysts. GO was synthesized using the modified Hummer's method [15-17]. For electrochemically reduced

Pt/graphene (Pt/ERG), a dispersion containing 1.0 mg mL^{-1} GO and 5 mM chloroplatinic acid hydrate ($H_2PtCl_6 \cdot xH_2O$) in 0.01 M phosphate buffered saline (PBS; 0.138 M NaCl, 0.0027 M KCl, pH 7.4) was prepared. Pt precursor was used to prepare mixed dispersions with GO for co-electrodeposition synthesis of Pt/ERG. The parameters for the pulsed galvanostatic electrodeposition were optimized at a peak current density of 300 mA cm^{-2}, an on/off time of 10/100 ms and a total charge density of 2 C cm^{-2}. After deposition, the working electrode was rinsed with distilled water and dried under an infrared lamp. For comparison of the electrochemically reduced graphene (ERG), a dispersion containing 1.0 mg mL^{-1} GO in 0.01 M PBS was also prepared using the same method.

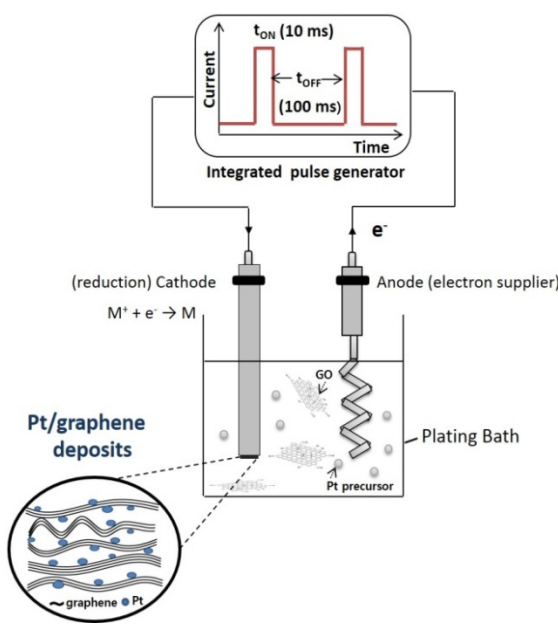

Figure 1. Schematic diagram of pulsed galvanostatic electrodeposition.

2. 2. Characterization

A field-emission scanning electron microscope (FE-SEM, JSM-6700F, JEOL) and high-resolution transmission electron microscope (HR-TEM, JEM-3010, JEOL) were used to assess the morphology of the catalysts. Energy dispersive spectroscopy (EDS) was used to confirm the existence of Pt particles. Fourier-transform infrared (FT-IR) spectra were recorded using a Nicolet 6700 (Thermo Scientific, USA) in the 500-4000 cm^{-1} infrared range using a KBr matrix. The Raman spectra of GO, ERG, and Pt/ERG were obtained using a micro-Raman system equipped with a homemade sample stage, a monochromator (SPEX 500 M), and a CCD camera (RogerScientific model 7346-001) with a 632.8 nm wavelength He/Ne laser line (power 2 mW). The chemical states of the component elements were determined using X-ray photoelectron spectroscopy (XPS; Sigma Probe, ThermoVG, U.K) with a monochromatic Al Kα X-ray source (1486.6 eV) with a 12 kV voltage and 10 mA current. The binding energies were corrected for charging by scaling them to the C 1s binding energy, 284.6 eV. The C 1s signals were collected and analyzed by deconvoluting the spectra using XPS peak software. The amount of deposited Pt was determined using inductively coupled plasma-atomic emission spectroscopy (ICP-AES). All electrochemical experiments were performed using an Autolab electrochemical workstation (Metrohm, USA) with a conventional three-electrode system. The electrochemical cell consisted of an electrochemically prepared sample on the GCE as the working electrode, Ag/AgCl (Bioanalytical Systems, Inc.) as the reference electrode, and a Pt wire as the

counter electrode. The scan rate used during the CV experiments was 50 mV s^{-1}. Electrochemical impedance spectroscopy (EIS) experiments were carried out using a GAMRY electrochemical analyzer system (Reference600, US) in a grounded Faraday cage at ambient temperature. EIS was conducted in the frequency range between 0.5 Hz and 1 MHz with a perturbation signal of 5 mV. The impedance data were fitted to an appropriate equivalent circuit using Echem Analyst™ Software. Electrochemical experiments were conducted in 5 mM $Fe(CN)_6^{3-/4-}$ /0.01 M PBS solution, 0.5 M H_2SO_4, 0.5 M CH_3OH/0.5 M H_2SO_4, respectively. For comparison, a commercial Pt/C catalyst (40 wt% Pt/C, E-TEK Inc.) was also tested under the same conditions.

3. RESULTS AND DISCUSSION

Co-electrodeposition synthesis of the Pt/graphene catalyst becomes possible because both GO and H_2PtCl_6 reduction reactions can occur under cathodic conditions simultaneously. **Figure 2** shows photo of electrochemically reduced graphene (ERG) and electrochemically reduced Pt/graphene (Pt/ERG) on indium tin oxide (ITO) glass in order to observe the color change of GO. The color was changed from brownish yellow (GO) to black (ERG and Pt/ERG) visible to the naked eye, which indicates the restoration of the π network within the carbon structure, and has been witnessed during the electrochemical reduction of GO [7].

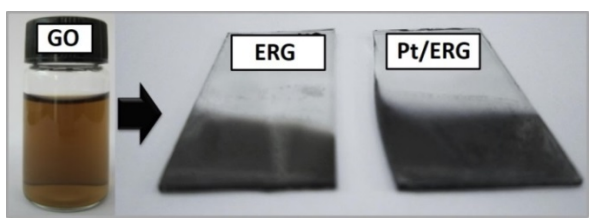

Figure 2. Photograph of electrochemically reduced graphene (ERG) and electrochemically reduced Pt/graphene (Pt/ERG) on ITO glass.

The electrodeposition process occurs by formation of fresh nuclei and by growth of deposits. These two processes are competitive, depending on the chemical and electrochemical parameters are related to the particle size. The Pt loading amount increases with the increase of total charge density and concentration of Pt precursor. When the concentration of Pt precursor at a fixed total charge density doubles, Pt metal ions are deposited approximately twice as much. (**Figure 3** and **Table 1**).

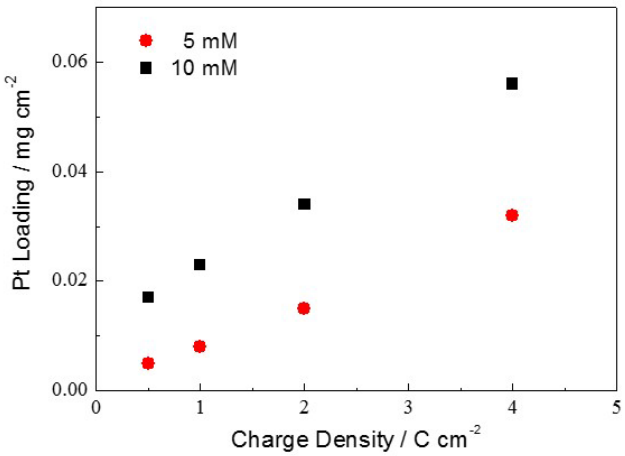

Figure 3. Amount of Pt loading according to the concentration of Pt precursor and charge densities (1.0 mg mL^{-1} GO, 300 mA cm^{-2}, 10/100 ms).

Table 1. Pt loading and electrochemically surface area by different concentration (1.0 mg mL^{-1} GO, 300 mA cm^{-2}, 2 C cm^{-2}, 10/100 ms).

Concentration	Pt Loading (mg/cm^2)	ECSA (m^2/g Pt)
5 mM $H_2PtCl_6 \cdot xH_2O$	0.015	45.2
10 mM $H_2PtCl_6 \cdot xH_2O$	0.034	37.8

Duration of the off-time plays an important role in the pulsed deposition since the recovery of concentration of the electroactive species at the surface of electrode (**Figure 4**). So the use of appropriate pulse variables creates predictable Pt/ERG morphology. The parameters for the pulsed galvanostatic electrodeposition were optimized at a peak current density of 300 mA cm^{-2}, an on/off time of 10/100 ms and a total charge density of 2 C cm^{-2}. Consequently, the repeated pulsed electrodeposition led to the formation of the Pt/ERG catalyst.

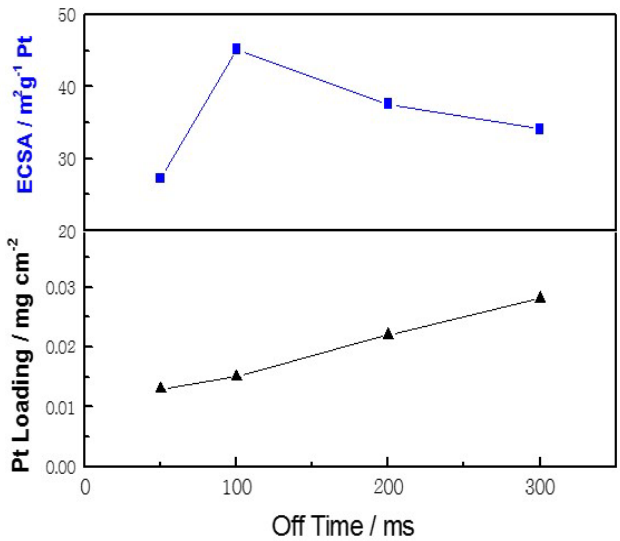

Figure 4. Pt loading and electrochemically surface area estimated for various off-times (5 mM $H_2PtCl_6 \cdot xH_2O$, 1.0 mg mL^{-1} GO, 300 mA cm^{-2}, 2 C cm^{-2}, 10 ms On time).

The surface morphology of ERG and Pt/ERG was examined using electron microscopy. SEM images revealed that the graphene appeared as an aggregation of thick flakes, each consisting of overlapping thin sheets, stacked in random orientations (**Figure 5** (a)). Pt/ERG catalyst can be successfully synthesized via electrochemical co-reduction (**Figure 5 (**b) and **Figure 5** (c)). Indeed, as shown in the **Figure 6**, the lattice spacing of Pt is ~ 0.22 nm, corresponding to Pt (111). It is clearly seen that Pt particles with a diameter of ~ 4.5 nm were dispersed uniformly on the graphene, which enables high electrochemical activity of Pt/ERG. It showed a much smaller Pt particle size than potentiostatic synthesis [14].

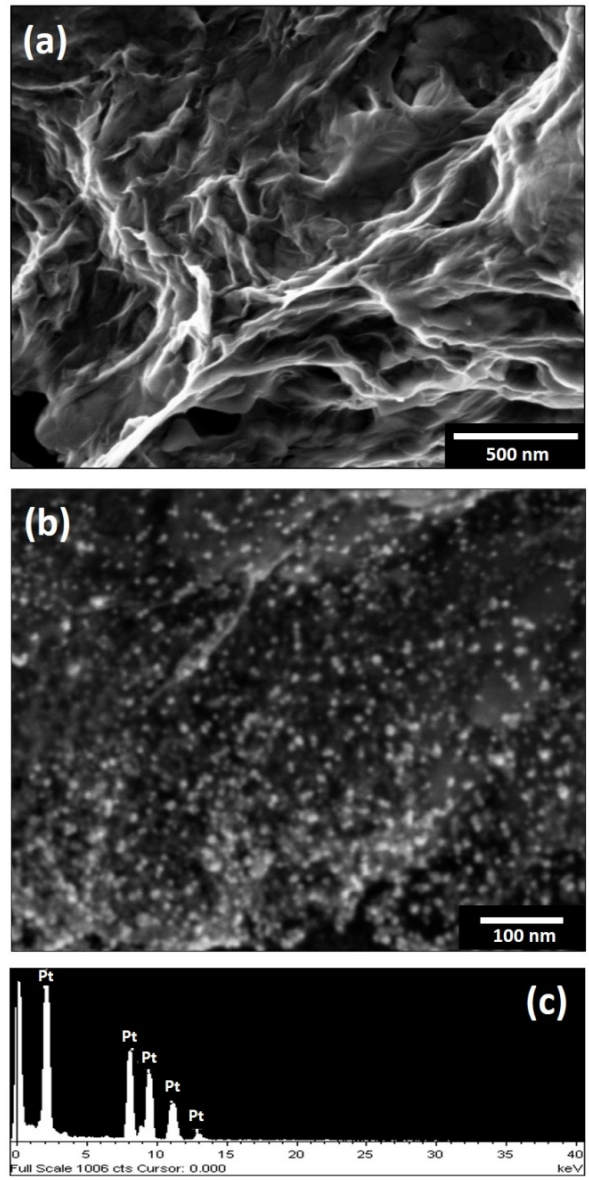

Figure 5. Typical SEM images of (a) electrochemically reduced graphene (ERG) and (b) electrochemically reduced Pt/graphene (Pt/ERG) catalyst by pulsed galvanostatic electrodeposition, respectively. (c) EDS spectrum of electrochemically reduced Pt/graphene (Pt/ERG) catalyst.

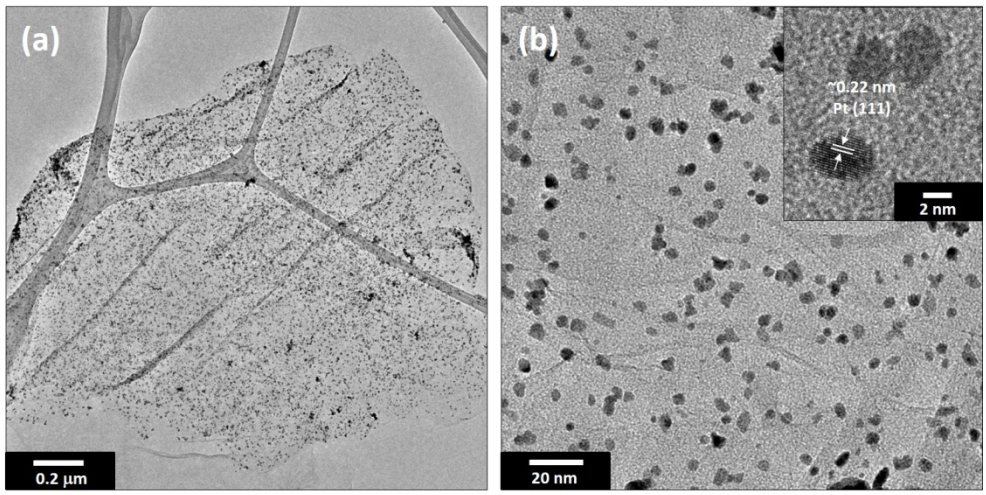

Figure 6. TEM images of electrochemically reduced graphene (Pt/ERG) at different magnifications.

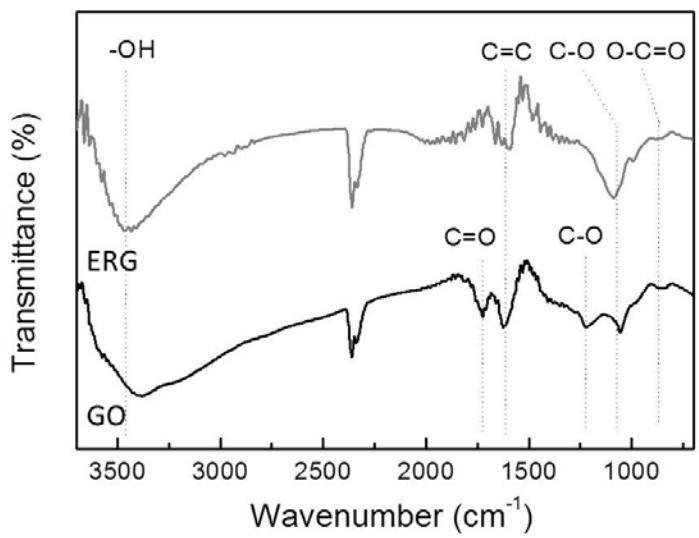

Figure 7. FT-IR spectra of graphene oxide (GO) and electrochemically reduced graphene (ERG).

To assess the reduction of GO, the nanostructures were characterized using FT-IR spectroscopy (**Figure 7**). The FT-IR spectrum of GO shows the presence of various oxygen-containing groups, including -OH (ν = 3400 cm^{-1}), carboxyl C=O (ν = 1730 cm^{-1}), aromatic C=C (ν = 1623 cm^{-1}), epoxy C-O (ν = 1268 cm^{-1}), alkoxy C-O (ν = 1082 cm^{-1}), and O-C=O (ν = 840 cm^{-1}), which were formed by the vigorous oxidation process [19-21]. As expected, most of the contributions in graphene from oxygen-containing groups decreased after electrochemical reduction.

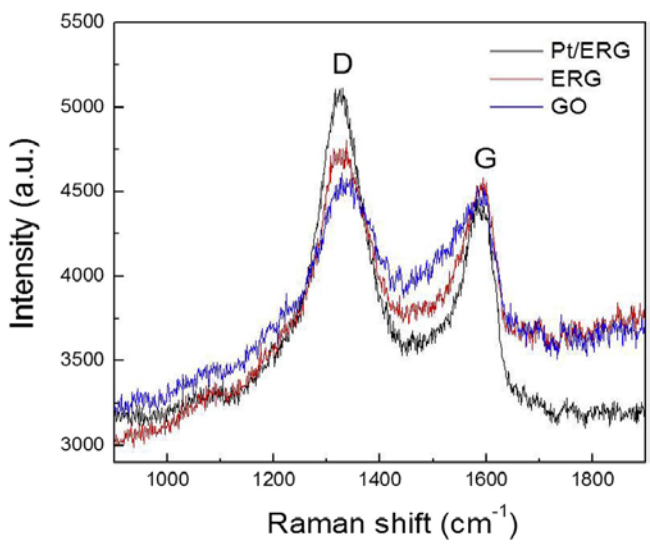

Figure 8. Raman spectra of graphene oxide (GO), electrochemically reduced graphene (ERG), and Pt/graphene catalyst (Pt/ERG).

Significant structural changes arising from electrochemical reduction from GO to graphene were reflected in the corresponding Raman spectra. GO, ERG, and Pt/ERG were characterized by Raman spectroscopy, and the results are shown in **Figure 8**. The two peaks were attributed to the G and D bands at 1593 cm^{-1} and

1338 cm^{-1}, respectively. The G band is related to the in-plane bond-stretching motion of pairs of sp^2-C atoms. The D band is the breathing mode of the sp^2-rings in the graphene layer related to a series of defects: bond-angle disorder, bond-length disorder and hybridization [22, 23]. The increased intensity ratio (I_D/I_G) of Pt/ERG was attributed to the increase in the graphene sheet defects caused by the incorporation Pt.

Surface chemical information was obtained using XPS. In brief, the C1s XPS spectrum of the GO (**Figure 9** (a)) clearly indicated a considerable degree of oxidation, with four components corresponding to carbon atoms in different functional groups: the non-oxygenated C ring (284.6 eV), the C in C-O (~286.8 eV), the carbonyl C (~287.8 eV), and the carboxylate carbon (O-C=O, ~289.5 eV) [24, 25]. The contribution of C-O was particularly high. After electrochemical reduction, the O/C ratio decreases notably in ERG, indicating that a majority of the oxygenated species were reduced. **Figure 9** (b) shows the XPS of Pt 4f of the electrochemically reduced Pt/graphene catalyst (Pt/ERG). The XPS signals were deconvoluted to their corresponding XPS signals for the Pt metal, Pt (II), and Pt (IV) species. Relative intensities of different species were calculated according to the area of the Pt $4f_{7/2}$ signal [26-29]. The results of the XPS analysis are presented in **Table 2**. As shown in **Table 2**, a large portion of the surface elements were in the form of metallic Pt species. According to the literature, greater metallic Pt content can result in higher catalytic activity [29].

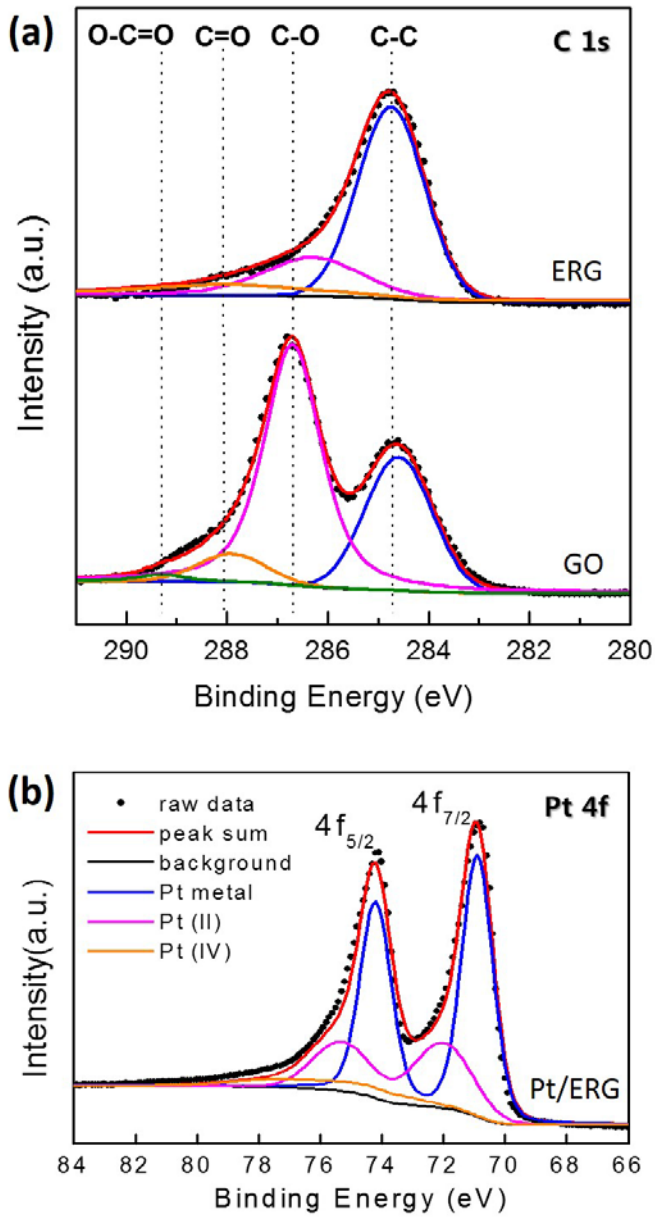

Figure 9. X-ray photoelectron spectra of (a) C 1s of graphene oxide (GO) and electrochemically reduced graphene (ERG), (b) Pt 4f of electrodeposited Pt/graphene catalyst (Pt/ERG).

Table 2. Binding energies and relative intensities of XPS spectra of Pt species in the electrochemically reduced Pt/graphene catalyst (Pt/ERG).

Species	Binding energy of $4f_{7/2}$ (eV)	Relative intensity (%)
Pt metal	71.0	69.5
Pt(II)	72.5	24.1
Pt (IV)	74.2	6.4

Figure 10 (a) shows cyclic voltammograms of 5 mM $Fe(CN)_6^{3-/4-}$ in 0.01 M PBS with bare GCE, ERG, and Pt/ERG catalysts. The peak current intensity of the Pt/ERG catalyst was 1.4 times higher than that measured with the bare GCE. It is assumed that these electrochemical properties are related to the larger electrochemical active surface area of the Pt/ERG structure. A pair of well-defined oxidation and reduction peaks was observed at 0.27 and 0.17 V with the Pt/ERG catalyst, indicating that conductive graphene facilitated electron transfer. The capacity of electron transfer of different catalyst was also investigated using electrochemical impedance spectroscopy (**Figure 10** (b)). In the Nyquist plot of impedance spectra, the semicircular portion at higher frequencies corresponds to the electron transfer limited process and the linear portion seen at lower frequencies ascribed to diffusion. The increased diameter of the semicircle reflects an increase in the charge transfer resistance (R_{ct}). Numerical values of R_{ct} were calculated from the experimental impedance spectra by fitting an equivalent circuit model to the data.

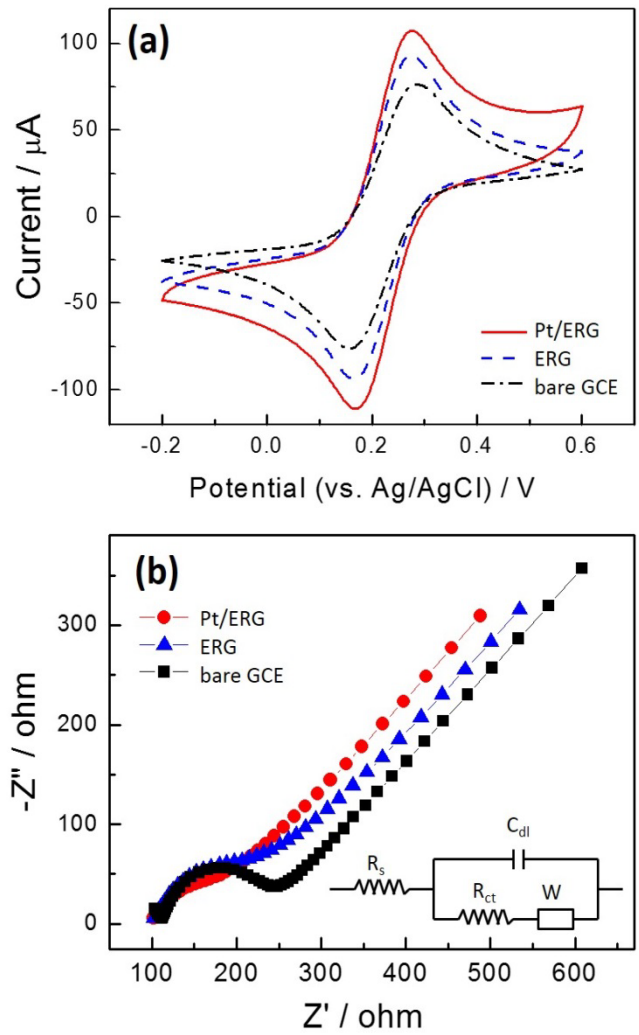

Figure 10. (a) Cyclic voltammograms of 5 mM $Fe(CN)_6^{3-/4-}$ in 0.01 M PBS on bare GCE (dash-dotted line), ERG (dashed line), and Pt/ERG (solid line) modified electrodes. Scan rate: 50 mV/s. (b) Nyquist plots of 5 mM $Fe(CN)_6^{3-/4-}$ in 0.01 M PBS on bare GCE (square), ERG (triangle), and Pt/ERG (circle) modified electrodes. The frequency range was from 0.5 Hz to 1 MHz. An ac amplitude of 5 mV was applied. Inset of (b) is the used equivalent circuit.

By fitting the data using an appropriate equivalent circuit, the R_{ct} values were determined to be 126.8 Ω on bare GCE, 77.7 Ω on the ERG, and 61.6 Ω on the Pt/ERG catalyst. The R_{ct} of the Pt/ERG catalyst was decreased compared to ERG catalyst. The Pt/ERG catalyst prevented graphene agglomeration and improved its conductivity [30, 31]. The higher electrocatalytic activity of the Pt/ERG catalyst was confirmed by the reduction of R_{ct} in electrochemical impedance spectra.

To characterize the deposited Pt, the prepared catalysts were cycled in a N_2 saturated 0.5 M H_2SO_4 electrolyte at 50 mV s^{-1}. A typical cyclic voltammogram of the Pt/ERG catalyst in acid is shown in **Figure 11** (a). Three potential regions are observed: (i) one pair of reversible hydrogen adsorption-desorption peaks (-0.2 ~ 0.1 V), (ii) double-layer formation (0.1 V ~ 0.3 V), and (iii) oxidation-reduction of Pt (0.3 V ~ 1.25 V). Pt nanoparticles have been effectively loaded between the graphene sheets. The amounts of deposited Pt and the commercial Pt/C were determined by ICP-AES to be 0.015 and 0.092 mg cm^{-2}. A commercial Pt/C electrocatalyst was selected with specification of 40 wt% Pt loading and particle size distribution in the range 2-5 nm. (**Figure 12**) The electrochemically active surface area (ECSA) values were calculated by measuring the coulomb charge for adsorption of the monolayer of hydrogen [32, 33]. The chemical surface area (CSA) of these Pt catalysts can also be calculated using the following equation:

$$S_{CSA} = \frac{6 \times 10^4}{\rho d}$$

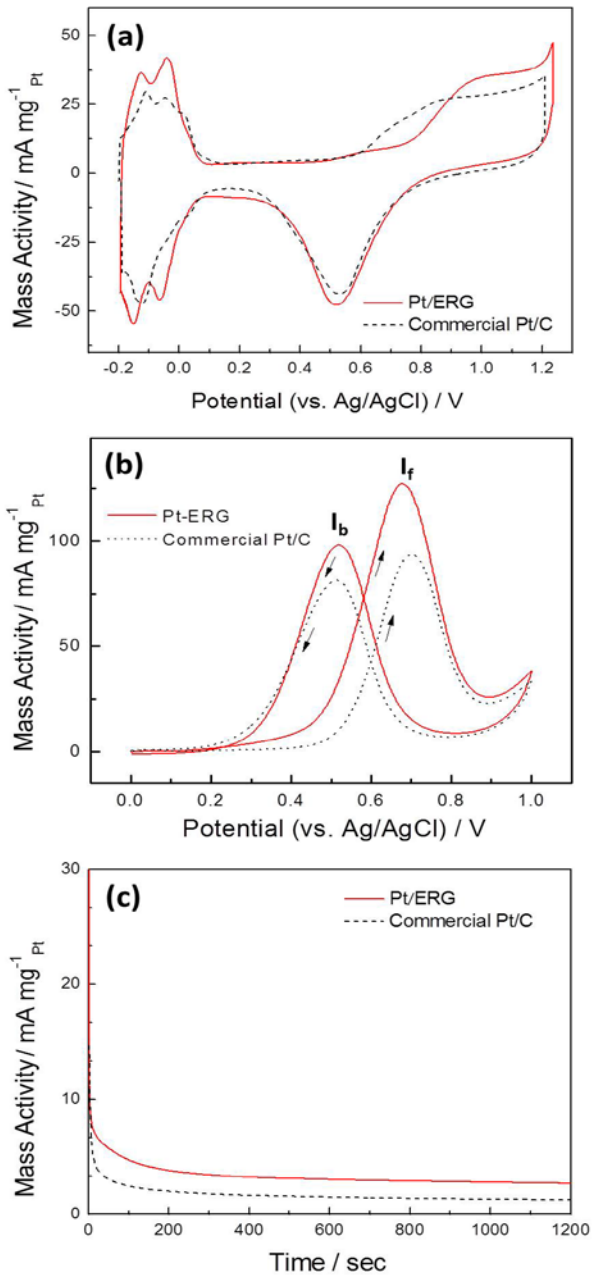

Figure 11. Cyclic voltammograms of the Pt/graphene catalyst (Pt/ERG, solid line) and commercial Pt/C (dashed line) in (a) 0.5 M H_2SO_4 and (b) 0.5 M CH_3OH + 0.5 M H_2SO_4 at 25 ^oC with a scan rate of 50 mV s^{-1}. (c) Chronoamperometric curves at 0.5 V in 0.5 M CH_3OH + 0.5 M H_2SO_4.

where *d* is the mean Pt particle in Å (from TEM results) and ρ is the density of Pt metal (21.4 g/cm^3).

Then the Pt utilization efficiency for methanol oxidation can be calculated [34-36]:

$$Pt\ utilization\ efficiency\ (\%) = \frac{S_{ECSA}}{S_{CSA}} \times 100$$

The ECSA values of the commercial Pt/C and the Pt/ERG were 36.5 and 45.2 m^2/g, respectively, based on the normalized Pt loading on the substrate. Pt utilization efficiencies for the commercial Pt/C and the Pt/ERG catalysts are about 50% and 73%, which is in good agreement with other's work [36]. This result indicates thatmore Pt was available electrochemically at the Pt/ERG catalyst than at the commercial Pt/C catalyst. The effective structure of Pt nanoparticles on the graphene sheets contributed to the ECSA value enhancement of the Pt/ERG catalyst.

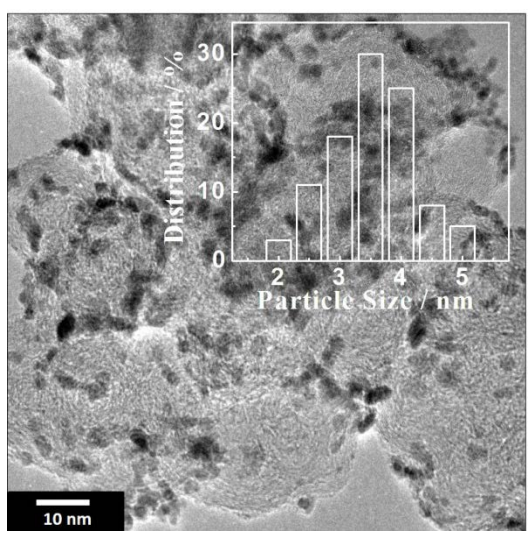

Figure 12. TEM image of commercial Pt/C.

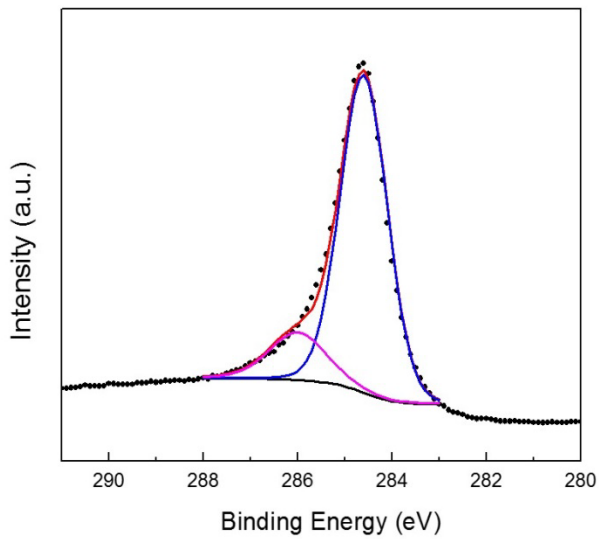

Figure 13. XPS spectrum of C 1s of commercial Pt/C.

To evaluate the activity of the Pt/ERG catalyst toward methanol electro-oxidation, cyclic voltammetry was performed in a N_2 saturated solution of 0.5 M CH_3OH in 0.5 M H_2SO_4 at a scanning rate of 50 mV s^{-1}. Before voltammograms were recorded, cycling was repeated until a reproducible CV curve was obtained. As shown in **Figure 11** (b), each of curves includes a methanol oxidation peak during the forward scan at around 0.6-0.8 V and another anodic peak during the reverse scan associated with the removal of incompletely oxidized carbonaceous species (such as CO) formed in the forward scan. The current of Pt/ERG catalyst at 0.5 V (vs. Ag/AgCl) was 25.6 mA/mg $_{Pt}$ and commercial Pt/C catalyst was 7.6 mA/mg$_{Pt}$. The current value of Pt/ERG catalyst was about 3 times higher than the commercial Pt/C catalyst. This shows that the Pt/ERG catalyst could be due to high

conductivity of graphene and highly Pt utilization efficiency. Generally, the ratio (I_f/I_b) of the forward peak current (I_f) to the reverse peak current (I_b), could be used to describe the catalyst tolerance to the carbonaceous species on the electrode surface. A higher ratio means the higher removal efficiency of the poisoning species [11, 37]. The I_f/I_b ratio of the Pt/ERG (1.24) is higher than that of the Pt/C (1.08), showing the better tolerance to the intermediate carbonaceous species. The improved CO tolerance of Pt/ERG is attributed to the increased amount of oxygen groups as well as to the strong interaction between the Pt nanoparticles and the graphene sheets [38, 39] (**Figure 13** and **Table 3**).

Table 3. XPS analysis: relative intensity contributions of Pt/ERG and commercial Pt/C.

Sample	**Relative intensity (%)**	
	Carbon	Oxygen
Pt/ERG	63.3	36.7
Pt/C	83.5	16.5

The long-term stability of methanol oxidation was conducted at 0.5 V and the variation of current with time was recorded (**Figure 11** (c)). The currents at Pt/ERG and Pt/C catalysts decrease rapidly at the initial stage, which is due to the formation of intermediate species during methanol oxidation reaction [40, 41]. However, the electrocatalytic stability of the Pt/ERG catalyst for the methanol oxidation reaction is higher than that of the Pt/C. From these results, the higher

activity and long-term stability of the Pt/ERG catalyst could be due to the synergetic effects of the Pt nanoparticles and the graphene sheets, such as an increase in the number of catalytic reaction sites and an enhancement of the charge transfer rate.

4. CONCLUSION AND PERSPECTIVE

We demonstrated a straightforward one step pulsed galvanostatic electrodeposition technique for the preparation of Pt/ERG catalyst for improved electro-oxidation of methanol. The Pt/ERG eletrocatalyst improved catalytic activity for methanol oxidation due to the synergistic effects of the Pt nanoparticles and the graphene sheets, such as an increase in the number of catalytic reaction sites caused by the well-dispersed graphene sheets, and an enhancement of the charge transfer rate. Due to the ease of synthesis of Pt/ERG catalyst, this pulsed electrodeposition technique may be applied to the fabrication of many devices such as sensors, fuel cells, supercapacitors, and batteries.

5. REFERENCES

[1] L. Chen, Y. Tang, K. Wang, C. Liu, S. Luo, *Electrochem. Commun*., 13 (2011) 133.

[2] M. Hilder, J. Winther-Jensen, D. Li, M. Forsyth, D.R. MacFarlane, Phys. *Chem. Chem. Phys*., 13 (2011) 9187.

[3] J. Ping, Y. Wang, K. Fan, J. Wu, Y. Ying, *Biosens. Bioelectron*., 28 (2011) 204.

[4] J. Feng, A. Li, A. Wang, Z. Lei, J. Chen, *Microchim Acta*, 173 (2011) 383.

[5] H.L. Guo, X.F. Wang, Q.Y. Qian, F.B. Wang, X.H. Xia, *ACS Nano*, 3 (2009) 2653.

[6] Y. Shao, J. Wang, M. Engelhard, C. Wang, Y. Lin, *J. Mater. Chem*., 20 (2010) 743.

[7] M. Zhou, Y.L. Wang, Y.M. Zhai, J.F. Zhai, W. Ren, F. Wang, S.J. Dong, *Chem. Eur. J*., 15 (2009) 6116.

[8] C.T.J. Low, F.C. Walsh, M.H. Chakrabarti, M.A. Hashim, M.A. Hussain, *Carbon*, 54 (2013) 1.

[9] M.S. Chandrasekar, M. Pushpavanam, *Electrochim. Acta*, 53 (2008) 3313.

[10] C. Hsieh, J. Wei, H. Hsiao, W. Chen, *Electrochim. Acta*, 64 (2012) 177.

[11] Y. Zhou, J. Chen, F. Wang, Z. Sheng, X. Xia, *Chem. Commun*., 46 (2010) 5951.

[12] Z. Yao, M. Zhu, F. Jiang, Y. Du, C. Wang, P. Yang, *J. Mater. Chem*., 22 (2012) 13707.

[13] C. Liu, K. Wang, S. Luo, Y. Tang, L. Chen, *Small*, 7 (2011) 1203.

[14] W. Ye, X. Zhang, Y. Chen, Y. Du, F. Zhou, C. Wang, *Int. J. Electrochem. Sci*., 8 (2013) 2122.

[15] Y. Kim, S. Bong, Y. Kang, Y. Yang, R.K. Mahajan, J.S. Kim, H. Kim, *Biosens. Bioelectron*., 25 (2010) 2366.

[16] A.J. Patil, J.L. Vickery, T.B. Scott, S. Mann, *Adv. Mater*., 21 (2009) 3159.

[17] S. Woo. Y. Kim, T.D. Chung, Y. Piao, H. Kim, *Electrochim. Acta*, 59 (2012) 509.

[18] D. Li, M.B. Müller, S. Gilje, R.B. Kaner, G.G. Wallace, *Nat. Nanotechnol*., 3 (2008) 101.

[19] Z. Liu, L. Jiang, F. Galli, I. Nederlof, R.C.L. Olsthoorn, G.E.M. Lamers, T.H. Oosterkamp, J.P. Abrahams, *Adv. Funct. Mater*., 20 (2010) 2857.

[20] T. Yang, L. Liu, J. Liu, M.L. Chen, J.H. Wang, *J. Mater. Chem*., 22 (2012) 21909.

[21] A. Kaniyoor, S. Ramaprabhu, *J. Mater. Chem*., 22 (2012) 8377.

[22] Y. Shao, S.H. Zhang, M.H. Engelhard, G. Li, G. Shao, Y. Wang, J. Liu, I.A. Aksay, Y. Lin, *J. Mater. Chem*., 20 (2010) 7491.

[23] H. Wang, Y.H. Hu, *Energy Environ. Sci*., 5 (2012) 8182.

[24] S. Stankovich, D.A. Dikin, R.D. Piner, K.A. Kohlhaas, A. Kleinhammes, Y. Jia, Y. Wu, S.B.T. Nguyen, R.S. Ruoff, *Carbon*, 45 (2007) 1558.

[25] O.C. Compton, B. Jain, D.A. Dikin, A. Abouimrane, K. Amine, S.T. Nguyen,

ACS Nano, 5 (2011) 4380.

[26] Y. Lu, R.G. Reddy, *Electrochim. Acta*, 52 (2007) 2562.

[27] K.C. Park, I.Y. Jang, W. Wongwiriyapan, S. Morimoto, Y.J. Kim, Y.C. Jung, T. Toya, M. Endo, *J. Mater. Chem*., 20 (2010) 5345.

[28] C. Nethravathi, E.A. Anumol, M. Rajamathi, N. Ravishankar, *Nanoscale*, 3 (2011) 569.

[29] I. Kim, S. Bong, S. Woo, R.K. Mahajan, H. Kim, *Int. J. Hydrogen Energy*, 36 (2011) 1803.

[30] L. Qiu, X. Yang, X. Gou, W. Yang, Z.-F. Ma, G.G. Wallace, D. Li, *Chem. Eur. J*., 16 (2010) 10653.

[31] S. Guo, D. Wen, Y. Zhai, S. Dong, E. Wang, *ACS Nano*, 4 (2010) 3959.

[32] R. Woods, A series of advances, in Electroanal. Chem., ed. A. J. Bard, Marcel Dekker, New York, 1974, vol.9 pp.1-162.

[33] M. Chen, Y. Xing, *Langmuir*, 21 (2005) 9334.

[34] G. Tamizhmani, J.P. Dodelet, D. Guay, *J. Electrochem. Soc*., 143 (1996) 18.

[35] W. Li, W. Zhou, H. Li, Z. Zhou, B. Zhou, G. Sun, Q. Xin, *Electrochim. Acta*, 49 (2004) 1045.

[36] S. Song, Y. Wang, P.K. Shen, *J. Power Sources*, 170 (2007) 46.

[37] T. Hyeon, S. Han, Y. Sung, K. Park, Y. Kim, *Angew. Chem., Int. Ed*., 42 (2003) 4352.

[38] S. Sharma, A. Ganguly, P. Papakonstantinou, X. Miao, M. Li, J.L. Hutchison,

M. Delichatsios, S. Ukleja, *J. Phys. Chem. C*, 114 (2010) 19459.

[39] N. Shang, P. Papakonstantinou, P. Wang, S.R.P. Silva, *J. Phys. Chem. C*, 114 (2010) 15837.

[40] Y. Liu, Y. Xia, H. Yang, Y. Zhang, M. Zhao, G. Pan, *Nanotechnology*, 24 (2013) 235401.

[41] Y. Xu, X. Lin, *J. Power Sources*, 170 (2007) 13.

ABSTRACT (in Korean)

연료전지는 가장 친환경적이고 효율이 높은 전기 생산 방식 중 하나이다. 그러나 대중적으로 사용되기 위해서는 몇 가지 해결해야 하는 과제가 있다. 본 논문에서는 이러한 과제들 중 (i) 백금 기반 촉매의 사용량을 절감하기 위한 촉매 및 전극의 제조 방법과 (ii) 새로운 촉매 담지체를 이용하여 백금 기반 촉매의 성능 향상 연구 그리고 (iii) 촉매와 담지체를 동시에 합성하는 방법에 관하여 연구하였다.

첫번째 파트에서는 촉매 및 전극 제조가 연료전지에 성능에 주는 영향을 중심으로 고찰하였다. 펄스 전류 전기환원법을 이용하여 연료전지 운전 중에 반응이 일어나는 삼상계면에 백금-코발트 입자를 담지 시켜, 촉매 이용 효율을 높이고 백금의 사용량을 절감하는 효과를 얻을 수 있었다. 용액 상에서 나피온이 포함된 탄소 전극의 표면에 직접 백금과 코발트의 이온을 담지하여 환원시키기 때문에 촉매층의 두께를 줄일 수 있고, 백금 담지량 또한 줄일 수 있었다. 막-전극 접착체의 단면을 보면 펄스 전류 전기환원법으로 제조한 전극이 기존의 방법으로 제조한 전극에 비해 두께가 얇으며, 전극 내부의 백금-코발트 분포는 나피온 막에 가까울수록 담지된 촉매의 양이 많고 멀어지면서 서서히 그 양이

감소하는 것으로 나타났다. 이것은 촉매의 사용 효율과 밀접한 연관성을 갖는다. 실제 연료전지 반응은 나피온 막에 가까울수록 많이 일어나며 전기환원법으로 제조한 촉매는 이와 잘 부합되어 촉매의 이용 효율이 높아지게 된다. 펄스 전류 전기환원법으로 제조한 전극의 경우 촉매 이용 효율이 높아졌음을 확인하였다.

두번째 파트에서는 새로운 탄소 담지체를 이용하여 백금 기반 촉매의 성능을 향상 시키고자 하였다. 삼차원 구조의 나노 스페이서를 삽입한 그래핀, 그리고 화학적으로 활성화 시킨 다공성 구조의 그래핀을 담지체로 이용하였다. 그래핀의 재결합 방지 및 삼상계면 증가와 반응물의 이동을 용이하게 하기 위해 그래핀에 나노 스페이서로 활성 탄소를 도입하였다. 그 결과 전기화학적 활성 면적이 증가되었고, 메탄올의 전기화학적 산화반응이 향상되었으며, 단위 전지 실험에서도 우수한 성능을 보였다. 더불어, 그래핀의 표면을 알칼리족 수산화물인 수산화칼륨으로 처리하여 다공성 구조의 활성화된 그래핀을 합성하여 촉매의 담지체로서 응용하였다. 그래핀 산화물 분산액에 수산화칼륨을 넣고 함침시키면 그래핀 시트 사이에 수산화칼륨이 끼어 들어가 탄소 원자 사이의 격자간격이 넓어진다. 이후 혼합액을 건조시킨 뒤 고온에서 열분해 시킨다. 그러면 그래핀 표면은 수산화칼륨과의 반응 및 반응 부산물로 인하여 에칭되고 그 자리에 기공이 생성된다. 이렇게 만들어진

다공성 구조의 활성화된 그래핀은 풍부한 기공을 통하여 비표면적을 넓히고 반응자리를 극대화 시킴으로써 더 빠르게 전기화학적 반응을 가능하게 하였다. 그 결과 전기화학적 활성 면적이 증가되었고, 메탄올의 전기화학적 산화반응이 향상되었다.

세 번째 파트에서는 펄스 전류 전기환원법을 이용해 촉매와 담지체를 동시에 합성하는 방법이다. 산화된 그래핀과 백금 전구체를 전기화학적으로 동시에 환원시켜서 그래핀-백금 촉매를 합성하였다. 기존 제조 방법보다 전기화학적으로 환원된 백금-그래핀 촉매가 반응 사이트 증가 및 전자 전달 속도의 향상으로 인해 메탄올의 전기화학적 산화반응이 우수해 졌음을 확인할 수 있었다.

주요어: 펄스 전류 전기환원법, 백금-코발트 합금 촉매, 백금-루테늄 합금 촉매, 그래핀, 나노 스페이서, 다공성 구조의 활성화된 그래핀, 촉매 이용 효율, 메탄올 산화반응, 고분자 전해질막 연료전지